UNIVERSITÀ DEGLI STUDI DELL'INSUBRIA

Facoltà di Scienze Matematiche, Fisiche e Naturali

Anno Accademico 2007-2008

Laurea Specialistica in Fisica

STUDY OF CHANNELING PHENOMENA IN BENT CRYSTALS: THE NEW FRONTIERS

Laureando: Davide Bolognini
Matricola 610319

Relatore: Dr.ssa Michela Prest
Università degli Studi dell'Insubria
Correlatore: Dr. Walter Scandale
CERN - Ginevra, Svizzera
Dr. Erik Vallazza
INFN - Sezione di Trieste

La scienza è fatta di dati come una casa di pietre.
Ma un ammasso di dati non è scienza
più di quanto un mucchio di pietre sia una casa.
Jules Henri Poincaré

Contents

Riassunto della tesi **v**

Introduction **1**

1 Bent crystals in different physics fields: where, how and why **5**
1.1 Beam collimation 6
1.1.1 The LHC collimation system 7
1.1.2 Bent crystals: a possible solution for the LHC phase II collimation 13
1.2 Microbeam 19
1.2.1 Biological application: from radiotherapy to space 19
1.2.2 Environmental studies 23
1.2.3 Physics & art: a microbeam factory 23
1.2.4 The microbeam and the crystal option 25
1.3 Synchrotron radiation sources and crystal undulators 28
1.3.1 Synchrotron radiation: dipoles, undulators and wigglers . 29
1.3.2 Crystal undulator (CU) 32

2 The physics of crystals **39**
2.1 Looking inside a straight crystal 39
2.1.1 The structure of crystals 40
2.1.2 The potential in a crystal 41
2.1.3 Particle motion in a crystal: channeling 44
2.1.4 Dechanneling 48
2.1.5 Axial channeling 49
2.2 A new era: the bent crystal 52
2.2.1 Particle motion in a bent crystal 53
2.2.2 Volume capture (VC) 57
2.2.3 Volume reflection (VR) 60
2.3 Energy loss by heavy and light particles 63
2.3.1 Energy loss by heavy particles 63

2.3.2 Channeling radiation in straight and bent crystals 65
2.3.2.1 Radiation in straight crystals 66
2.3.2.2 Radiation by channeled particles in bent crystals 67
2.3.3 Radiation emitted in volume reflection 72

3 The 2007 experimental setup 77
3.1 The CERN SPS H8 beamline 77
3.2 The 2007 beam tests 79
3.2.1 The silicon detectors 81
3.2.2 Calorimeter for the October 2007 beam test 84
3.2.3 The DAQ 87
3.3 The crystals 89
3.3.1 The quasimosaic crystal 90
3.3.2 The strip crystal 91
3.3.3 The multicrystal system 92
3.4 The goniometer 93
3.5 The new setup at work 95
3.5.1 Pre-alignment 98
3.5.2 Lateral scan 98
3.5.3 Angular scan 98

4 The experimental results 101
4.1 Studies with hadrons 102
4.1.1 VR as a function of the crystal curvature 103
4.1.1.1 Geometrical and divergence cuts and the critical angle evaluation 104
4.1.1.2 The VR behavior as a function of the crystal primary curvature 107
4.1.2 The multicrystal 112
4.1.3 Diamond crystal 117
4.1.4 The negative particles 119
4.2 Light particles: electrons and positrons 121
4.2.1 The crystal behavior with light particles: analysis cuts and angular scan 122
4.2.2 Energy loss by light particles 125
4.2.2.1 The amorphous contribution 127
4.2.2.2 VR radiation spectra 127
4.3 And there is much more... 129

5 Conclusions and outlooks 131

Conclusions & outlooks **131**

A Data processing **137**
A.1 Pedestal, noise and common mode 137
A.2 Processing data 139
A.3 ASCII file 141
A.4 The detector alignment 142

List of acronyms **145**

List of figures **151**

List of tables **153**

Bibliography **155**

Acknowledgments **162**

Riassunto della tesi

Questo lavoro di tesi descrive gli ultimi risultati ottenuti nello studio dei fenomeni di channeling e volume reflection in cristalli incurvati. Nel 1912 J. Stark, un fisico tedesco, ipotizzò che alcune direzioni in un cristallo potevano risultare più trasparenti al passaggio di particelle cariche: questa ipotesi venne verificata sperimentalmente con fasci di ioni solo negli anni '60 e da allora diversi studi vennero intrapresi soprattutto a bassa energia.

Il fenomeno venne definito *channeling* ed avviene quando una particella carica attraversa il cristallo allineata rispetto ad un suo piano (o asse): essa rimane intrappolata tra i piani cristallini a causa di una serie di urti correlati con i diversi atomi, diversamente da quanto avviene in un materiale amorfo. Il moto della particella nei piani può essere descritto come il movimento di una carica in un campo elettrico: la buca di potenziale che si forma permette il confinamento del moto.

Una svolta importante nello studio di questi fenomeni avvenne nel 1976 ad opera di un fisico russo, E. Tsyganov, il quale propose di incurvare dei cristalli di silicio per deviare fasci di particelle cariche: curvando un cristallo, infatti, vi è una corrispondente piegatura dei piani atomici che lo costituiscono; pertanto una particella che viene confinata tra due piani atomici non può far altro che seguirlo, deviando dalla sua traiettoria nominale. Tre anni dopo, questa idea venne confermata sperimentalmente presso il Fermilab di Chicago (USA).

Solo recentemente è stato scoperto e studiato un interessante fenomeno legato alla curvatura dei cristalli: all'interno del volume cristallino può avvenire la condizione di tangenza tra il canale costituito dalla buca di potenziale e la traiettoria della particella incidente. In questa condizione possono avvenire due fenomeni: la *volume capture* (in cui una particella viene confinata in un piano cristallino) e la *volume reflection* in cui la traiettoria di una particella subisce una riflessione totale nel volume. Questo secondo fenomeno venne scoperto nel 1987 in alcune simulazioni e venne osservato sperimentalmente per la prima volta nel 2006.

I fenomeni di channeling e volume reflection vennero accolti con grande interesse dall'ambiente scientifico: l'idea di sostituire oggetti pesanti e di grosse dimensioni come i magneti dipolo con oggetti di pochi millimetri suscitò l'interesse ed incentivò la ricerca.

La prima naturale applicazione di questi oggetti sembrò essere proprio la collimazione in acceleratori di particelle. I moderni acceleratori richiedono un sistema di collimazione a multi stadio per ridurre gli effetti dell'alone del fascio ed aumentare la luminosità della macchina: in generale le particelle dell'alone vengono deviate su tutto l'angolo solido sfruttando l'effetto di multiplo scattering all'interno di collimatori primari (materiali amorfi); lo sciame prodotto viene successivamente assorbito da collimatori secondari e terziari.

In acceleratori di alta energia, come ad esempio il Large Hadron Collider (LHC) presso il CERN, questi sistemi di collimazione devono sopportare una grande quantità di radiazione e devono essere efficienti: utilizzando il sistema appena descritto, si è stimato che nella prima fase di collimazione di LHC, la luminosità massima raggiungibile sarà solo il 40% di quella nominale. I cristalli curvati potrebbero rappresentare una valida soluzione a questo problema: essere utilizzati quali collimatori "intelligenti', deviando le particelle dell'alone in una particolare direzione con un'alta efficienza.

Tuttavia la collimazione è solo un esempio delle possibili applicazioni di questa tecnologia: da fasci di ridotte dimensioni (microbeam) alla radiazione, diverse linee di ricerca sono attualmente in fase di studio o test. I microbeam sono utilizzati in adroterapia per il trattamento tumorale, in biologia per lo studio del comportamento di una singola cellula all'interno di un tessuto, in applicazioni legate all'ambiente ed all'arte per la determinazione della composizione di campioni e manufatti. Tradizionalmente sono prodotti tramite lenti elettrostatiche e magneti. In questo ambito l'effetto di channeling potrebbe essere sfruttato per focalizzare i fasci, mentre strutture diverse (come i nanotubi) permetterebbero di creare fasci di dimensioni ridotte.

Per quanto riguarda la radiazione, cristalli noti con il nome di ondulatori potrebbero rappresentare la sorgente di radiazione del futuro. In un sincrotrone, elettroni ultrarelativistici possono irradiare in magneti dipolo (radiazione di sincrotrone) o in sezioni diritte per mezzo di magneti ondulatori o wiggler, generando diversi tipi di radiazione in termini di intensità e spettro. I cristalli ondulatori dovrebbero permettere di sostituire questi ultimi, fornendo un fascio di fotoni di alta intensità.

Questa tesi si apre con la descrizione dei possibili campi di applicazione dei cristalli, confrontandoli con le tecniche attualmente usate e presentando brevemente lo stato di sviluppo di ciascuna applicazione.

Alla fisica dei cristalli è dedicato il capitolo 2: partendo dai cristalli diritti per arrivare a quelli curvati e all'analisi di tutti i fenomeni che possono caratterizzare il passaggio di una particella carica in un cristallo. L'ultima parte del capitolo si addentra nel difficile ambito della radiazione emessa da particelle leggere (elettroni e positroni) in cristalli curvati.

Il nocciolo duro di questa tesi è rappresentato dal lavoro sperimentale e di

analisi dati svolto all'interno della collaborazione H8RD22, che ha come scopo principale lo sviluppo di un sistema di collimazione basato su cristalli di silicio curvati. I dati sono stati raccolti nel periodo Maggio-Novembre 2007, anche se durante la scrittura di questa tesi un lungo periodo di presa dati è in corso.

Il comportamento dei cristalli è stato studiato su una linea di fascio estratto (H8, presso il Super Proton Synchrotron del CERN) con un setup dedicato, descritto nel capitolo 3: la traiettoria delle particelle viene ricostruita a partire dalle informazioni di rivelatori a microstrip di silicio (con una risoluzione spaziale di 5 μm), mentre i cristalli (a strip o quasimosaico), piegati tramite holder meccanici, sono posizionati su un sistema goniometrico di alta precisione per l'allineamento sul fascio e per lo studio del comportamento tramite gli scan angolari. La procedura di stripping dei raw data è descritta in appendice A.

I test sono stati effettuati con diversi fasci di particelle: protoni con momento di 400 GeV/c, adroni positivi e negativi di momento 180 GeV/c ed elettroni/positroni di 180 GeV/c.

Il capitolo 4 descrive parte dei risultati raccolti dalla collaborazione H8RD22 in questi due anni: questo lavoro di tesi si basa principalmente sull'analisi del comportamento dei parametri della volume reflection in funzione del raggio di curvatura e sulla radiazione emessa da elettroni e positroni quando il cristallo è in condizione di volume reflection. Nel 2006 il fenomeno della volume reflection è stato misurato ad alta energia tramite l'utilizzo di rivelatori al silicio sviluppati per un esperimento spaziale; nel 2007 un setup dedicato ha permesso uno studio approfondito dei parametri della volume reflection (angolo di deflessione, RMS ed efficienza) al variare del raggio di curvatura del cristallo: dai dati raccolti è stato possibile identificare un particolare valore del raggio tale per cui il prodotto tra l'angolo di deflessione e l'efficienza è massimo.

Nel Novembre 2007 è stata (per la prima volta) valutata la radiazione emessa da elettroni e positroni da 180 GeV/c in condizione di volume reflection: lo spettro di energia dei fotoni si estende sino a 100 GeV ed è stato misurato sfruttando un metodo spettrometrico basato sull'utilizzo di rivelatori al silicio di grandi dimensioni e di un calorimetro elettromagnetico per l'identificazione dei leptoni. I risultati sperimentali sono stati confrontati con calcoli analitici e simulazioni con GEANT3 per quanto riguarda la condizione amorfa (o cristallo non orientato) ottenendo un buon accordo, mentre vi è una discrepanza tra i risultati teorici e sperimentali per quanto riguarda la radiazione emessa in volume reflection, che richiederà un supplemento di indagine sia teorica che sperimentale.

Nell'ottica di utilizzare un cristallo in volume reflection per la collimazione, con il vantaggio di una grande accettanza angolare (superiore a ~ 100 μrad rispetto a ~ 8 μrad per il channeling a 400 GeV/c) e di una grande efficienza, è necessario aumentare l'angolo di deflessione (~ 10 μrad rispetto a quello di channeling, superiore a ~ 100 μrad), mettendo tanti cristalli uno di seguito all'altro: le particelle

riflesse dal primo cristallo entrano nell'accettanza del secondo che le riflette a sua volta e così via.

Nel 2007 è stato valutato il comportamento di un multi cristallo costituito da 5 cristalli quasimosaico controllati remotamente tramite motori piezoelettrici. Il sistema di multi cristallo è stato studiato in termini di angolo di deflessione, efficienza e ripetibilità.

Il capitolo 4 riassume anche parte dei risultati ottenuti in questi due anni: dal comportamento di un cristallo incurvato con adroni negativi, allo studio preliminare di un cristallo di diamante, sino all'evidenza sperimentale del channeling assiale, intrappolando la particella nelle due direzioni.

L'insieme di risultati presentato in questa tesi dimostra come i cristalli (la cui storia inizia quasi un secolo fa) siano un argomento di estrema attualità, e come l'utilizzo nel campo della collimazione sia solo una delle possibili applicazioni. Se da un lato in questi ultimi due anni i diversi effetti sono stati misurati e capiti dal punto di vista teorico, rendendo la tecnologia pronta per test di collimazione, lo studio dell'emissione di radiazione è un campo aperto con diverse possibili applicazioni: dalla creazione di una sorgente di positroni per il linear collider alla collimazione di fasci di elettroni e positroni, alla produzione di fasci fotonici di alta intensità con ondulatori cristallini, per svariati usi tra cui quelli in fisica medica.

Entrambi questi aspetti vengono affrontati nelle conclusioni della tesi. Per quanto riguarda la radiazione, viene descritto un setup dedicato per una fase di misura a diverse energie. Nell'ambito della collimazione, viene illustrato il progetto CRYSTAL, approvato dal Research Board il 3 settembre 2008, che consiste di un test di collimazione nell'SPS con protoni da 120 GeV/c. Tale test è previsto nel 2009, con un possibile seguito nel 2010 a Fermilab con il fascio da 980 GeV del Tevatron.

Introduction

When a physicist hears the word “crystal” he thinks of calorimeters, silicon detectors, a particular state of matter. When he hears the word “magnet” he thinks of big, heavy objects. More or less 30 years ago, it was experimentally demonstrated how a crystal (a bent crystal to be more precise) can become a magnet. Much more than this: an object 1 mm thick, a couple of mm wide and a few cm high is capable of steering particles as a dipole of several tens of Tesla.

The goal of this thesis work is to give an insight of the physics of bent crystals from several points of view: their behavior with heavy and light particles, the possible applications in different fields and the experimental results obtained in recent beam tests. Crystals came on stage 100 years ago going through long periods of stand by. Their history can be summarized with a few dates:

1912: a German physicist, J. Stark, suggested that certain directions in a crystal could be more transparent to the motion of charged particles with respect to amorphous materials. This theory was confirmed only in the ’60s by experiments with ion beams which showed an anomalous penetrating capability in crystals. It was the dawn of the channeling experiments.

1976: a Russian physicist, E. H. Tsyganov, applied Stark’s suggestion to study the effects of a charged particle beam in a bent crystal. The idea is incredibly simple: exploiting the potential created between the atomic planes, particles can be deflected from the initial trajectory.

1979: Tsyganov’s idea was confirmed by experiments in Fermilab.

1987: a new phenomenon was discovered in computer simulations: when a particle with an incoming angle in a particular range impinges on a bent crystal, a trajectory reflection can occur: this phenomenon was called *volume reflection* and has been experimentally confirmed in 2006.

2006: for the first time the H8RD22 collaboration measures the channeling and volume reflection phenomena with very high precision silicon detectors at very high energy using 400 GeV/c protons.

From the middle of the ’70s the ideal application for crystals was identified with beam collimation in high energy hadron colliders. Modern accelerators require a multi-stage collimation system to reduce the effects of the beam halo and

increase the luminosity: in general the primary beam halo is spread on the whole solid angle by a primary collimator (an amorphous target); the produced shower is absorbed by the secondary bulk collimator while scattering needs a tertiary system to complete the cleaning.

In very high energy machines this system must be very efficient and must tolerate very high radiation. At the Large Hadron Collider (LHC) at CERN, for example, the first phase collimation system is expected not to allow to reach the nominal luminosity, limiting it to 40% of the desired value. A bent crystal could play a key role being a clever collimator: it is able to steer particles in a given direction with a high efficiency, thus increasing the cleaning efficiency, reducing the constraints on the alignment of the secondary collimator and finally increasing luminosity. “Could” instead of “can” means that in principle (and in simulations) this is the possible scenario but several tests in circular machines are needed to definitely check this hypothesis.

Collimation is not the only example of a possible application: from microbeams to radiation, several development lines are under study or under test. Microbeams are used in hadron therapy to treat cancer, in biology to study the behavior of single cells in tissues, in environmental and artistic studies to determine the composition of the involved materials. In general a microbeam is provided by electrostatic lens and electromagnetic quadrupoles. The channeling effect which occurs in bent crystals can be exploited to focus beams, while different structures (i.e. carbon nanotubes) can steer part of a primary beam forming a sharp edge microbeam.

The so-called “crystal undulators” can be exploited as radiation sources. In a synchrotron accelerator, ultra relativistic electrons can irradiate in bending magnets (synchrotron radiation) or in straight sections (insertion devices) using undulator or wiggler magnets, generating different radiation fields in terms of intensity and spectra. A crystal undulator is a particular crystal which can provide a high intensity gamma beam, replacing the classical magnets.

The first chapter of this thesis is dedicated to a review of examples of these applications and of the possible role of crystals, while a brief overview of the physics and the motion of a charged particle in a bent crystal is given in chapter 2. When a crystal is bent, according to Tsyganov’s suggestions, a charged particle (which impinges on it with a certain angle) follows the channel and is steered with a high deflection angle. Several phenomena can occur in a bent crystal depending on the angle between the crystallographic plane and the incoming particle trajectory. The most recent discovery, *volume reflection*, has aroused a lot of interest as far as collimation is concerned: in volume reflection a particle is reflected by the interatomic plane potential (thus the deflection is in the opposite direction with respect to channeling) with high efficiency and a large angular acceptance (that is the angular region where it can occur).

A review of the radiation features and the theoretical bases of radiation emitted by light particles in crystals is also presented in chapter 2: in particular this thesis work describes the experimental results of the first measurement of the radiation emitted by a bent crystal in volume reflection at high energy.

All the crystal effects have been studied on an extracted beam line with a dedicated setup described in chapter 3: a set of double side 5 μm resolution silicon detectors which are used to determine the trajectory of each particle, a high precision goniometer to align the crystal with the beam and perform an angular scan and different types of crystals (strip and quasimosaic). These crystal designs have been tested both in single mode and in the multicrystal configuration: in particular, a remote control system to align five quasimosaic crystals with respect to the beam has been tested in November 2007.

While the last part of chapter 3 focuses on the analysis to extract the relevant information from the angular scan, appendix A describes the analysis procedure for the silicon detectors, which are the real winning tool of these experiments.

Chapter 4 is a review of the results of the 2007 beam tests from ultra relativistic 400 GeV/c proton beams to 180 GeV/c light particles (electrons and positrons).

Using protons the volume reflection parameters (the angular mean value, its RMS and the inefficiency) as a function of the crystal curvature have been evaluated obtaining a good agreement among experimental, simulation and analytical data; the behavior of several multicrystal systems is described in terms of the total deflection angle, efficiency and repeatability; the preliminary study of a diamond crystal is briefly described.

For the first time, in October 2007, the VR was observed with 180 GeV/c electrons and positrons. High energy spectra (up to $\sim$100 GeV) have been measured exploiting a spectrometer method based on large silicon strip detectors and on a sampling calorimeter for the electron identification; the experimental results have been compared with analytical calculations, showing that a lot of work has to be done both from the experimental and simulation point of view.

The concluding remarks of this thesis work concern the future of crystals: from collimation of positive and negative beams to the possibility of using the radiation they produce for medical, biological and matter science, from the use of different materials to the still open questions in the crystal physics field. Some of the tests require different and dedicated experimental setups; in some cases the agreement between data and analytical simulations is still far from being satisfactory.

A collimation test will be performed on the Super Proton Synchrotron at CERN in 2009 and a similar one is foreseen at Tevatron (Fermilab) in 2010. An electron beam with the ideal features is being looked for to study radiation and new crystal types are being produced.

Only a step of a long way that started almost 100 years ago.

Chapter 1

Bent crystals in different physics fields: where, how and why

The study of channeling related phenomena in high energy physics has started many years ago but, even now, it is extremely up-to-date: the channeling phenomena (especially in bent crystals) are, in fact, a possible answer to unsolved problems in different physics fields.

The most important application of this technology seems to be beam collimation in high energy hadron colliders where luminosity can be dramatically reduced by the effects of the beam halo. Hadron accelerators are characterized by a large energy stored in the beam and by a high sensitivity of super-conducting magnets to particle losses, both of which are a cause of concern to the collimation system.

Modern accelerators require a multi-stage collimation system: the primary collimator (usually a solid target) intercepts the primary beam halo spreading it on the whole solid angle; the secondary halo is absorbed by the secondary bulk collimator while scattering needs a tertiary system to complete the job.

In very high energy machines, like the Large Hadron Collider (LHC) at CERN, this system must be very efficient (to prevent beam induced quenches of the magnets) and must tolerate very high radiation (given by the particle type and energy and the beam intensity). The LHC first phase collimation system is based on the multiple scattering effect inside the first absorber (the halo, in fact, is spread over the whole solid angle increasing its divergence) being thus characterized by a low efficiency and reducing luminosity: in the LHC case the effective luminosity should be about 40% of the nominal one.

An object able to deviate particles outside the beam in a given direction would increase the cleaning efficiency, reduce the constraints on the alignment of the secondary collimator and finally increase luminosity. A bent crystal could be such an object.

The working principle of a bent crystal allows its use in different fields, among

which microbeam applications. Microbeams are used in hadron therapy to treat cancer, in biology to study the behavior of single cells in tissues, in environmental and artistic studies to determine the composition of the involved materials. A microbeam is typically provided by electrostatic lens, while the beam focusing is guaranteed by electromagnetic quadrupoles. Bent crystals can be an alternative solution: they can be used as focusing magnets with excellent results at high energy, while channeling in different structures (carbon nanotubes) can steer part of a primary beam forming a sharp edge microbeam.

Another application of bent crystals in high energy physics is represented by the use of the so-called "crystal undulators" as radiation sources. High energy radiation is necessary in a lot of fields (from medicine to technology developments) thanks to its penetration capability; one of the most important sources is represented by the synchrotron accelerator where ultra relativistic electrons can irradiate in bending magnets (synchrotron radiation) or in straight sections (insertion devices) using undulator or wiggler magnets, generating different radiation fields in terms of intensity and spectrum. A classical electromagnetic undulator could be replaced by a so-called "crystal undulator" which exploits its peculiar characteristics (small dimension and high equivalent "magnetic field") to provide a high intensity gamma beam.

This chapter is dedicated to a brief review of the problematics that crystals could help to solve in different physics fields, underlining the pros and cons of the present technologies.

1.1 Beam collimation

Particle physics is strictly linked to the developments reached in the accelerator technology. The most important present accelerator, currently under commissioning at CERN, is the Large Hadron Collider (LHC) which will operate at a center-of-mass collision energy of 14 TeV [1]. LHC is a hadron storage ring of 27 km of circumference which can collide both protons-protons and ions-ions. While LHC is almost ready to produce physics, a new big project is under study to collide electrons and positrons of 500 GeV/c of momentum: the International Linear Collider (ILC) will have to face problems similar to the ones of a hadron collider.

In both these experiments, in fact, one of the critical issues is the luminosity[1], which in practice can be defined as the number of particles per $cm^{-2}\ s^{-1}$; colliders are characterized by a high luminosity (a typical number for LHC is $10^{34}\ cm^{-2}$

[1]For a given process, the luminosity (L) is defined as the rate between the number of events (N_{ev}) and the cross section (σ_{ev}) of the process itself: $N_{ev} = L\sigma_{ev}$. In a collider, the luminosity is given by: $L = f(n_1 n_2)/(4\pi\sigma_x\sigma_y)$, where f is the collision frequency, n_x the number of particles per bunch per beam, $\sigma_x\sigma_y$ the beam dimensions.

s^{-1}) to guarantee a large number of collisions, thus requiring very high intensity beams colliding at the interaction point (IP). In order to ensure the quality of the beam, the *beam halo* (formed by particles with a large momentum offset or too far from the nominal accelerator trajectory) should be critically reduced by a *collimation system*, whose tasks can be listed as follows [2]:

- reduction of the background in the experiments particle detectors;
- protection of machine components, minimizing their activation and damage. In high energy colliders, in particular, super-conducting magnets are a great concern, given their quenching limit;
- self-protection. The collimation system should be radiation hard in order to avoid being destroyed during the operation.

Collimation in circular colliders is based on the so-called *multi-stage system*, and LHC represents an ideal example to understand the performances and limits of the presently used technologies.

1.1.1 The LHC collimation system

LHC is designed to perform proton-proton (Pb ion-Pb ion) collisions with a center-of-mass collision energy of 14 TeV (180 GeV/nucleon) [1, 3] in four interaction points, corresponding to four experiments: ALICE, ATLAS, CMS and LHCb[2].

Figure 1.1(a) compares LHC with older and present accelerators: the transverse beam density is three orders of magnitude larger and the beam energy increases of a factor 7 with respect to the oldest accelerators [3]. These expected performances have been made possible by the use of advanced super-conducting magnets, that bend the charged particles in the ring, provide the required focusing fields for the stored beams and focus the beams in the collision points (figure 1.1(b) shows the quadrupoles before the ALICE interaction point).

The performances of the LHC magnets are guaranteed by the super-conducting technologies at temperatures as low as 1.8 K and 4.5 K, providing a nominal field of 8.33 T. These cryogenic temperatures make the magnets sensitive to any heat source, among which beam losses can be listed: if the magnet heating exceeds a threshold called *quench limit*, the magnet cables suffer a transition from super-conducting to resistive, reducing the bending capability. The LHC quench limits are about 10 mJ/cm^3, corresponding to a local transient loss of only $4 \cdot 10^7$ protons (being the total number of protons per beam $N_{tot} \sim 3 \times 10^{14}$ at 7 TeV).

[2] ATLAS and CMS are general purpose experiments, LHCb is optimized for B meson physics while ALICE will study the physics of strongly interacting matter at extreme energy densities using heavy Pb ions.

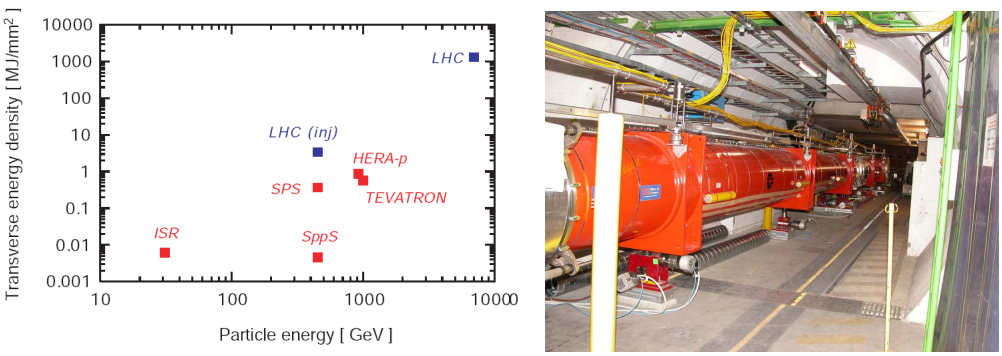

(a) (b)

Figure 1.1: a) Transverse energy density as a function of beam momentum for several accelerators [4]. b) The super-conducting magnets at the ALICE interaction point.

LHC beams are designed to have a maximum stability and to be stored for many hours (typically 30 h). During this period, the beam losses are able to induce enough heating in the magnets to cause quenches: the total stored energy, in fact, can reach 360 MJ per beam, ten orders of magnitude higher than the quench limit.

In order to fulfill the operational constraints, the collimation system must have the following features [5]:

- **Beam loss rates**: the LHC operation includes short periods of reduced beam lifetime. At 7 TeV, it means an acceptable loss of 4.1×10^{11} protons/s for 10 s or 0.8×10^{11} protons/s continuously; the collimation system has to withstand these numbers;

- **Cleaning inefficiency**: the cleaning inefficiency qualifies the efficiency of the collimation system. In order to understand its definition, the concept of aperture should be explained: the machine aperture identifies the available transverse plane in which a particle can circulate. There are two types of apertures (figure 1.2): geometric (given by the mechanical lattice) and dynamic (due to distorsions of the nominal orbit given by non-linear elements).

  The cleaning inefficiency η_c is defined as the ratio between the number of particles escaping the cleaning insertions that reach a normalized mechanical aperture (10σ for LHC) and the number of particles impacting on the primary collimator; from simulation computations, this number is of the order of 10^{-3}. The surviving particles can get lost in the machine and be the main cause of the magnet quench; thus a limit can be defined as the *local cleaning inefficiency* (η_l), which is the total number of protons lost over a

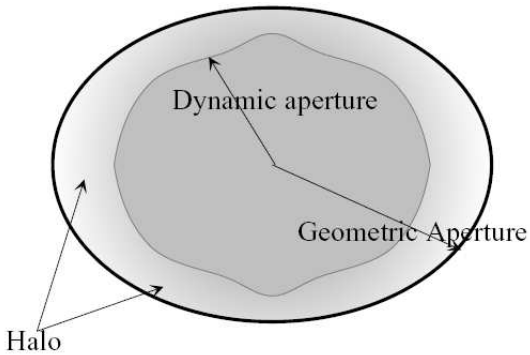

Figure 1.2: The geometric and dynamic apertures [6].

given length (L_{dil}), normalized to the total number of cleaned protons:

$$\eta_l = \frac{\eta_c}{L_{dil}} = 2 \times 10^{-5} \mathrm{m}^{-1}$$

The present length value is L_{dil}=50 m, but this number is still not accurate. In order to quantify the beam loss, the beam lifetime (τ_q) should be introduced: τ_q is defined as the time needed to reduce the number of initial particles by a factor e. In a circular accelerator, the particles inside the dynamic aperture are stable for many turns, while the halo particles get lost. However the beam halo is continuously re-generated due to the stable particles which can be kicked out: these effects are called *regular proton losses*. Moreover, particles can also produce *irregular proton losses*, which are due to unexpected beam conditions during a relatively short period of time, generally of the order of 1 second.

Taking into account all these processes, it is possible to calculate the corresponding beam lifetimes and thus the level of local losses that must not be exceeded in order to avoid magnet quenches.

Assuming a minimum required beam lifetime of 0.2 h (which corresponds to a 1% beam loss in 10 s) at 7 TeV (the operational energy) and 0.1 h at 450 GeV (the injection energy) [4], the maximum number of protons in the LHC beam can be estimated as:

$$N_{tot} = R_q \cdot \tau_q \cdot \frac{1}{\eta_l}$$

where R_q represents the magnet quench limit expressed in number of protons per meter per second. The maximum proton intensity as a function of the local collimation efficiency is shown in figure 1.3; since the total 7 TeV

protons which are requested to circulate in LHC for physics are of the order of $N_{tot} \sim 3 \times 10^{14}$ and the quench level (R_q) is set to 7×10^8 protons/(m s), the local cleaning inefficiency has to be 2×10^{-5} m^{-1}, as already stated.

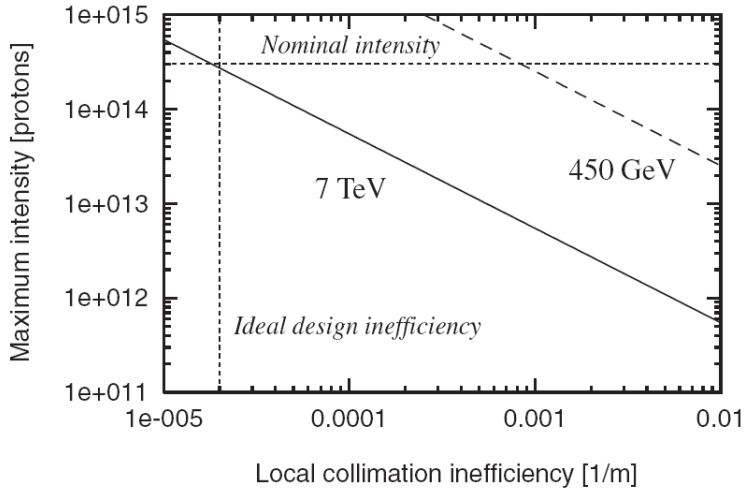

Figure 1.3: The beam intensity as a function of the local cleaning inefficiency for energies of 450 GeV and 7 TeV [4].

- **Number of collimators and phase advance requirements**: the collimation system is designed to provide momentum and betatron cleaning in different phase advance locations in the LHC ring [7]. The momentum collimators remove halo particles with a large energy offset ($\Delta p/p$), while the betatron ones remove halo particles with a large transverse amplitude. Depending on the collimation kind, different amounts and types of collimators have been considered in two special locations.

- **Beta functions in cleaning insertions**: the beta function (the transverse particle oscillation around the nominal trajectory) should be larger at the collimators in order to reduce the effect of the bunches if they impact on the jaw. However, the beta functions are limited in the 50-350 meter range due to the available space.

- **Collimator gaps and impedance**: the primary and secondary collimators must be close to 6 and 7σ respectively to provide the required cleaning efficiency. Since the impedance scales inversely proportional to the third power of the gap size, the collimators can produce a significant transverse resistive impedance: at the nominal beam intensity the total collimator impedance should be 110 MΩ, while the impedance generated by the rest of the ring is 100 MΩ;

- **Vacuum aspects and maintenance**: the geometry and the materials must be chosen to reduce the outgassing and to allow rapid interventions in case of malfunctioning.

The LHC collimation system, according to the requests formerly expressed, is designed to protect the LHC equipment (including electronics and the machine itself) from a peak beam loss rate of 1% in 10 s (4×10^{11} protons/s), from regular and irregular (due to equipment failure or wrong operation) beam losses with sufficient efficiency ($> 99.9\%$).

The collimation system will be implemented in different steps, following the natural upgrade of the machine performance. The initial system (*phase I*) has been developed to guarantee the maximum robustness against the normal and abnormal high power events. Robustness plays a key role in the collimation system because of the inaccessibility of the machine: a damage to a collimator or a machine component, in fact, requires an immediate access in a high radiation environment and problems due to vacuum. In order to overcome the limitations due to the impedance of the initial LHC collimators, in *phase II* several low-impedance advanced collimators will be used.

As already said, the choice of the material of the collimator jaws is a critical issue [8]. Since the collimator has to withstand a very high energy density deposit in a short time (of the order of nanoseconds), low Z materials are the best choice. An increase of the atomic number would correspond to a strong decrease of the radiation length with a consequently large contribution of the electron-gamma part in the cascade and its higher spatial concentration which would cause a greater heating of the collimator itself. The selection of the materials has been evaluated by simulations as shown in figure 1.4.

The most important candidates seem to be graphite and beryllium: the latter has not been considered because it would not resist the specific one-turn energy load and it is toxic [1]. The graphite disadvantage is its poor conducting power which increases the total impedance of the machine, that is, in fact, dominated by the collimator impedance [9]. A computation of the collimator induced impedance is estimated to limit the total machine intensity to about 40% of its nominal value [10].

Figure 1.5 shows the LHC collimation layout for phase I. In total there are 152 possible locations for collimators and absorbers for the two beams. In phase I, 88 ring collimators will be present. Further 34 ring locations are equipped and ready for an upgrade in 2010.

The LHC multi-stage collimation (as shown in figure 1.6(a)) consists of four blocks:

- **Primary collimators**: robust carbon-fibre-reinforced carbon composite (CFC) jaws [11, 12] for the interception of the primary beam halo at 6σ (RMS of

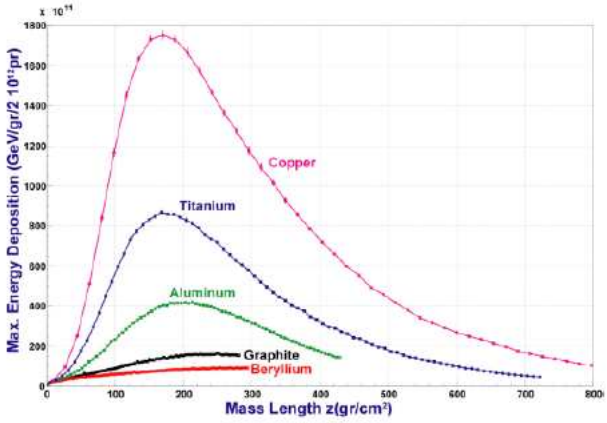

Figure 1.4: FLUKA simulations of the maximum energy deposit as a function of the mass length (and thus Z) for different materials [8].

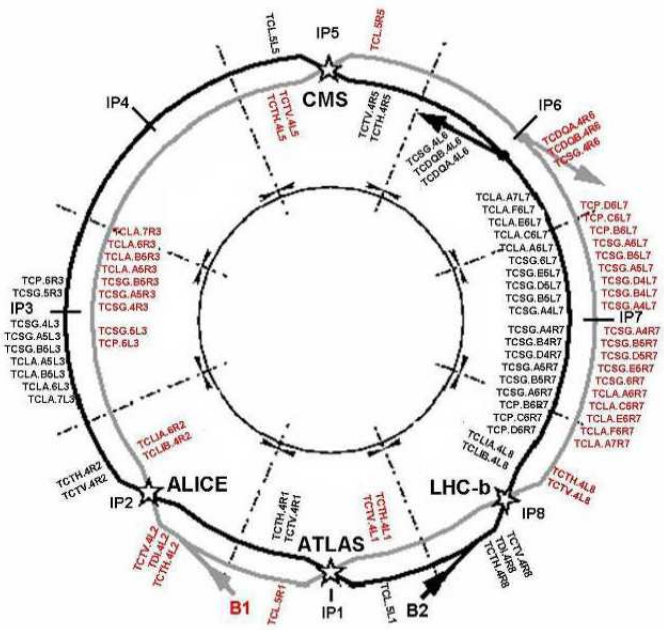

Figure 1.5: Layout of the LHC collimation during phase I. Red labels are beam 1 collimators, while black ones refer to beam 2 [10].

the beam profile) from the core with an impact parameter (the average distance between the collimator border and the proton impact position) smaller than 1 μm;

- **Secondary collimators**: longer robust CFC jaws [11, 12] to intercept the secondary beam halo at 7σ and reduce it (figure 1.6(b));
- **Tertiary collimators**: jaws for the interception of the tertiary beam halo and the protection of the triplets in case of unlikely events;
- **Absorbers**: high-Z collimators of Cu or W at the end of the cleaning insertions to protect the super-conducting magnets from the tertiary halo (mainly due to particle showering in the collimator jaws).

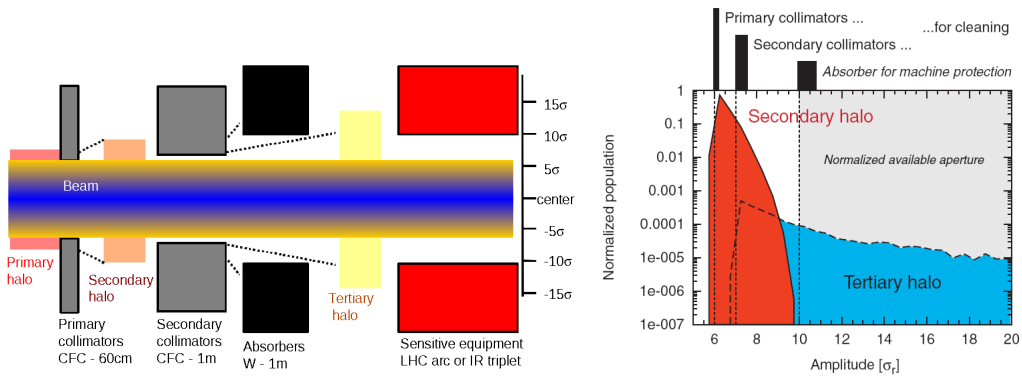

(a) (b)

Figure 1.6: a) Principle of collimation and beam cleaning during collisions in phase I. b) Normalized population of secondary and tertiary beam halo for protons impinging on the first collimators.

1.1.2 Bent crystals: a possible solution for the LHC phase II collimation

The robustness required in the first phase of the LHC collimation limits the machine luminosity to 40% of the nominal one. A R&D is necessary to develop and characterize a collimation system which can increase the machine luminosity, reducing the impedance and beam halo.

Different solutions have been presented [2]:

- **Consumable collimators**: proposed for the ILC experiment, this system is based on jaws that can be moved to a new position a finite number of times after having been damaged by the beam in case of direct impact [13]. The mechanical schemes are based on wheels, bars and tapes which can be transversely moved (figure 1.7): a wheel collimator requires vacuum

bearings but its design is very simple; a tape collimator requires a complex vacuum mechanical system but it has a large usable area; a bar collimator doesn't require vacuum moving parts but its structure is too large with respect to the usable area. Among these, a prototype based on rotating wheels

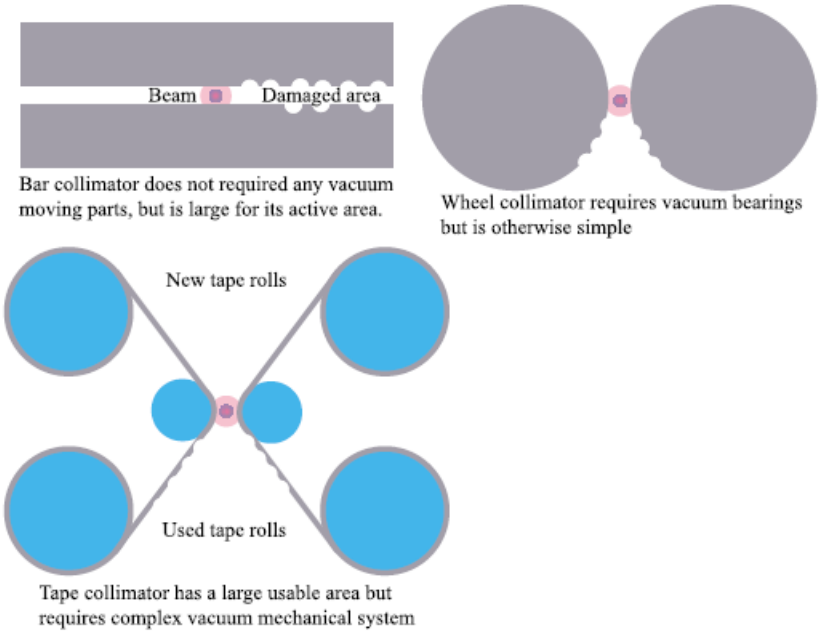

Figure 1.7: Consumable collimators based on bars, wheels and tapes [2].

has been chosen;

- **Repairable collimators**: they are based on jaws which can be continuously repaired during operation [13]. The idea is that the surface of the rotating jaws is exposed to a bath of liquid metal: this is frozen on the surface of slowly turning metal drums and then the solid surface is rolled flat with smoothing rollers. The problem is given by the choice of the metal, which should have the following features: low vapor pressure at melting point, elemental in order to avoid fractional crystallization during the solidification, no or low toxicity and adherence to the jaw surface. At present molybdenum seems to be a good candidate [13];

- **Laser collimation**: laser collimation consists in the Compton scattering of electrons or positrons in the transverse halo tails off a high power laser beam, avoiding the regime where pair production occurs [14]. The scattered halo particles, which are off-energy, should be intercepted in downstream absorbers placed in the dispersion region. The advantage of this system is

that it cannot be destroyed by the beam impact, but laser technology means high costs and very precise alignment with respect to the beam. Moreover, a failure in the laser could damage other accelerator components;

- **Electron lens collimation**: the system is based on very strong non-linear field components present in a hollow electron beam in an electron lens. Electron lens collimation offers a possible solution to the ion fragmentation problem in ion beam collimation.

Another possible solution is represented by bent crystals: their physics will be briefly presented in chapter 2; in this section the bent crystal key features will be introduced to explain the possible role of these innovative collimators in the LHC machine.

In a traditional multi-stage collimation system (figure 1.8(a)), an amorphous target spreads the primary halo on the whole solid angle and part of it is intercepted by the secondary collimators and absorbers. Bent crystals, instead, can be used as "intelligent" collimators (figure 1.8(b)): the beam that impinges on the crystal can be completely steered on a secondary collimator with a high efficiency, reducing the impedance and the alignment constraints of the secondary collimators themselves.

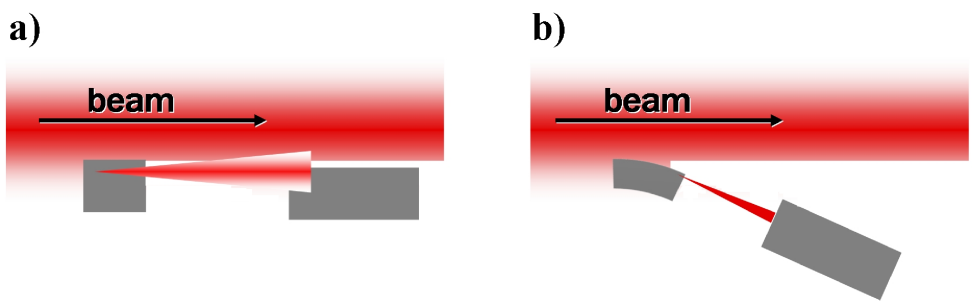

Figure 1.8: a) Traditional multi-stage collimation system: particles are spread on the whole angular range and then absorbed by secondary collimators and absorbers. b) A bent crystal in a channeling position steers the whole beam halo onto an absorber, increasing the efficiency and reducing the impedance.

Bent crystals could (since several tests are still needed) represent a valid alternative for the LHC phase II collimation. Their features can be summarized as follows:

Collimation efficiency. A bent crystal can be used as a primary collimator in two different configurations, depending on the angle between the interplanar potential in the crystal and the particle trajectory: channeling and volume

reflection (section 2.2). Channeling is characterized by a large deflection angle and an efficiency of the order of 70%, while the volume reflection efficiency is close to 100% with a small deflection angle, a factor 10 less than channeling (all these parameters depend on the energy and geometrical configuration of the crystal itself). Considering the goal of high efficiency, three different collimation possibilities can be identified: “singlepass” channeling that occurs when particles are deflected at the first impact with the crystal; “multipass“ channeling, in which particles hit more than once the crystal before being deviated enough to be absorbed by the secondary collimator (these possibilities have been already simulated for LHC by a Monte Carlo code as shown in figure 1.9); volume reflection.

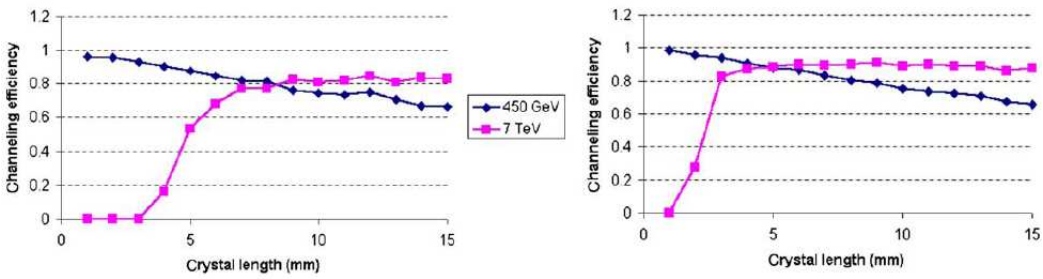

Figure 1.9: Simulated channeling efficiency as a function of the crystal length for the injection and operational energies. Crystal bending: 0.2 mrad (left), 0.1 mrad (right) [15].

Volume reflection could be used in principle both in singlepass and multipass. Moreover, to increase the deflection angle, a multi volume reflection system has to be developed (figure 1.10(b)): several crystals are aligned with respect to the beam in the volume reflection position to obtain a larger deflection angle, maintaining the acceptance (see below) and the efficiency large.

Angular acceptance. Particle deflection occurs when a particle impinges on the crystal with a certain angle with respect to the interplanar planes. The angular range where the deflection can occur is called angular acceptance. The channeling angular acceptance is the so-called Lindhard critical angle (chapter 2) and it is a function of the energy: at LHC, the channeling acceptance is 9.4 μrad at 450 GeV and 2.4 μrad at 7 TeV.

The volume reflection acceptance is a function of the crystal curvature and, for a typical curvature of 10 m, is around 100 μrad. Such a large value ensures a higher stability with respect to the beam variations and less stringent alignment requirements.

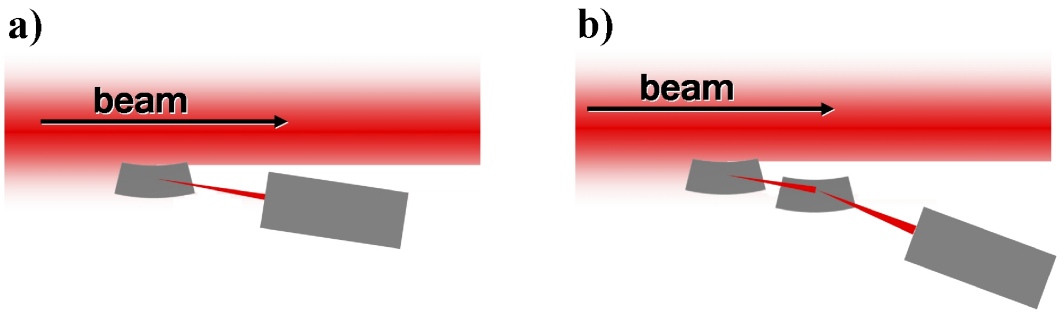

Figure 1.10: a) A bent crystal in a volume reflection position steers the beam halo onto an absorber. b) The volume reflection deflection angle is increased by a multi crystal system, maintaining a high efficiency and a large acceptance.

Deflected beam. A collimation system requires a large impact parameter which is given by the product of the deflection angle (or angular kick) and the distance between the primary and secondary collimators. The angular kick produced by bent crystals depends on the angle between the incoming particle and the crystallographic planes, that in turn identifies a channeling or a volume reflection effect. The channeling deflection angle is a function of the crystal length and of its bending radius; a great deflection angle corresponds to a low efficiency. On the other side, in the volume reflection case, a smaller deflection angle with respect to the channeling one is compensated by a higher efficiency and acceptance.

In order to use bent crystals as primary collimators, a complete characterization of the deflected beam in the LHC machine must be provided by Monte Carlo simulations in which all the crystal physics details are included together with the shape of the beam which impinges on the crystals themselves and the secondary collimators.

Crystal alignment. The crystal alignment with respect to the beam is fundamental to reach the best performance of the crystal itself. The alignment precision is a function of the acceptance: the smaller the acceptance, the higher the precision required on the alignment.

Surface specification. The roughness of the crystal surface is usually modelled as a thin amorphous layer where the crystal lattice presents imperfections and crystal effects have a very small probability to happen. The amorphous layer must be limited because the average impact parameter on the primary collimator is usually very small, 100-200 nm in the present LHC system [16].

The presence of a superficial amorphous layer on the crystal surface has been considered in several Monte Carlo simulations [15], to evaluate its impact on the efficiency. Figure 1.11(a) shows the simulated efficiency as a function of the amorphous layer thickness; a smaller thickness corresponds to a greater efficiency. It must be underlined that the multipass effect reduces the importance of this layer. Anyway, recent studies on a crystal surface treatment which involves mechanical polishing and chemical etching [17] have demonstrated that a crystal surface with imperfections below 100 nm (figure 1.11(b)) can be produced.

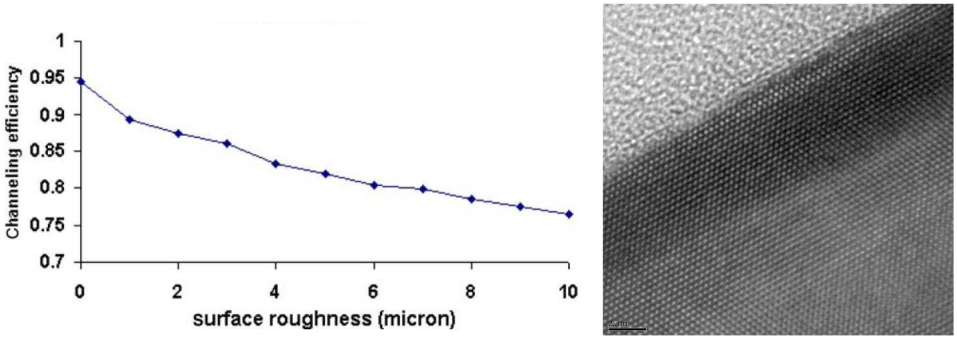

(a) (b)

Figure 1.11: a) Simulated channeling efficiency as a function of the crystal surface roughness. b) X-ray image of a crystal surface which doesn't present an amorphous layer (thanks to INFN Ferrara for the picture).

Radiation hardness. A critical task for a collimation system is represented by the robustness of the system itself against the energy deposited by the particles which could cause thermal shock, radiation damage and eventually the reduction of the crystal life. The capability to withstand a high energy beam intensity was tested at IHEP [18] where a 5 mm long crystal was exposed for several minutes to a 10^{13} 70 GeV proton circular beam in spills of 50 ms every 9.6 s. After this exposure (which corresponds to 1000 LHC bunches), the crystal was tested in an external beam line. The deflected beam observed with photoemulsions was exactly the same as the one pre-exposure. Other experiments at CERN (NA48 [19]) and IHEP [20] have shown that at the achieved irradiation of $5 \cdot 10^{20}$ protons/cm^2 the crystal loses only 30% of its deflection efficiency which means it can survive about 100 years in an intense beam like the NA48 one.

1.2 Microbeam

The last frontier in medicine and biology and related fields is the study of the behavior of a single cell in different conditions. In cell and structural biology the typical dimensions are spanning the length scales from a few nanometers up to centimeters, thus a *microbeam* of the order of a few nanometers is requested. Microbeams can be used in different fields; in this thesis work four applications will be briefly presented:

1. **Medicine**: beams in air for hadron therapy with an energy of the order of 100 MeV;
2. **Biology**: beams in air and vacuum for study of biological structures at low energies with the goal to understand the behavior of each single structure when a single particle hits it;
3. **Environmental study**: beams in air and vacuum for elemental analysis to identify sources of pollution in different environments;
4. **Physics applications to arts**: beams in air or vacuum for studies on artwork materials.

An example of these topics will be briefly described in this section, underlining the most important characteristics for a microbeam factory and the possibility to use crystals in these systems.

1.2.1 Biological application: from radiotherapy to space

Microbeams in biology are mainly used for their high collimation and low current ($\sim$ 1 nA) features: the behavior of each single cell when a particle hits it is under study since the discovery of particles. There are a lot of possible microbeam applications in biology: from radiotherapy, studying the effect of ionizing particles in cancer or healthy tissues, to space, such as the NASA studies on the possible problems due to cosmic radiation in advanced space missions.

As far as radiotherapy is concerned, a possible application is the study of the so-called *bystander effect* in cells and tissues [21]. The effects of exposures to ionizing radiation are under study since soon after its discovery, more than 100 years ago. Radiobiology has been and is a must to assess radiotherapy as a cancer treatment, to develop treatment plans which have to consider both the dose to the tumor and the nearby tissues, to find the best way of fractionating the dose delivery in order to allow the healthy cells to repair the radiation damages. Among the non-targeted effects (which are those where cells appear to respond to ionizing radiation through ways other than direct damage to the DNA), there is the so-called

bystander-effect which describes the behavior of an unirradiated cell exhibiting damage in response to signals transmitted by irradiated neighbors.

The bystander-effect dominates the dose-response at low dose (<200 mGy), but saturates as the dose increases (as shown in figure 1.12(a)).

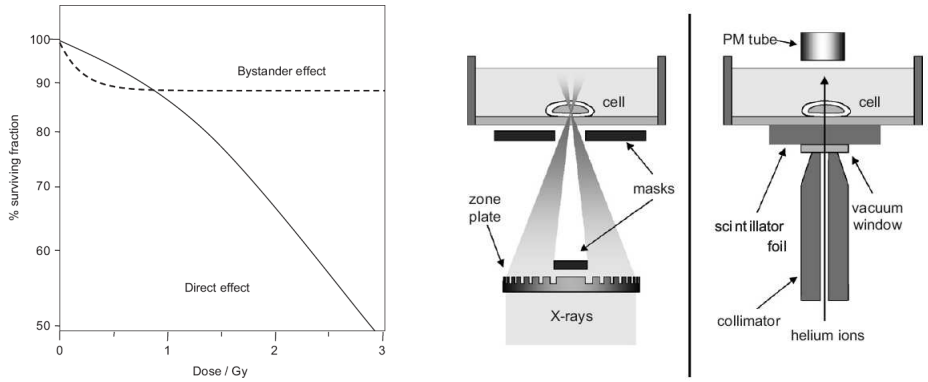

(a) (b)

Figure 1.12: a) Typical cell survival curves: the bystander-effect seems to be more important than direct irradiation at low doses. b) Two methods used to generate a microbeam. Left: low energy X-rays are focused using a zone-plate diffractive optics. Right: ions collimated using a glass capillary.

Different methods are used in bystander-effect studies but, in general, the irradiation of the whole tissue is performed, while interesting cells are protected by masks and grids. Microbeams represent a possible alternative thanks to their versatility in terms of design and execution: a microbeam can be used to irradiate just a single cell within a cell population.

The typical radiobiological microbeams are produced with charged-particles, low-energy X-rays and low-energy electrons; in particular, most particle microbeams use light ions, such as protons or helium because of their high linear energy transfer (LET[3]) and high relative biological effectiveness (RBE[4]).

Figure 1.12(b) shows two methods to irradiate cells [21]. Protons and light ions (right figure) are accelerated with a 4 MV Van der Graaff accelerator and then steered vertically towards the cell irradiation apparatus. The microbeam is provided by a 1 μm diameter bore silica capillary collimator; the particles scattering inside cells are detected by a photomultiplier tube (PMT). As far as a X-ray

[3]LET quantifies the energy transferred to a material by an ionizing particle which travels through it.

[4]RBE identifies the different degrees of effectiveness in producing effects in biological systems.

microbeam is concerned (left figure), a X-ray microfocused source generates low-energy X-rays that are subsequently focused to a micro-sized spot using a small diffraction lens (zone-plate). X-rays are able to penetrate the first cell layer and therefore much better suited to studies involving tissues and multi-cellular samples.

Another fundamental application for microbeams is hadron therapy. Hadron therapy was born in 1946 when Robert R. Wilson made the first proposal to treat cancer using proton beams. This treatment is in rapid evolution and the total number of patients has increased from 10000 in 1993 to 50000 in 2006, with a progression which seems to be exponential [22].

With respect to typical radiotherapy treatments, which use photons (for deep tumors) or electrons (for superficial tumors) accelerated by linear accelerators (LINAC), hadron therapy is based on protons or light ions, which have three considerable advantages [23]:

1. they penetrate the patient practically without diffusion;
2. they deposit the maximum energy density abruptly at the end of their range (Bragg peak, as shown in figure 1.13(a)), producing severe damage to the target cells;
3. the beam shape and dimensions can be changed in a rather simple way and the energy can be chosen according to the depth of the tumor in the body.

In 1996 a collaboration formed by CERN, GSI, Med-AUSTRON, Oncology 2000 and TERA started a new project for a hadron machine called PIMMS (Proton and Ion Medical Machine Study) [24, 25]. This machine can be considered as an example of an up-to-date hadron factory. It consists of:

- two LINACs for protons (20 MeV) and carbon ions (7 MeV/nucleon);
- two dispersion-free zones for injection and RF acceleration in a lattice made of short and cheap bending magnets;
- single-turn injection;
- slow extraction;
- an ”empty“ bucket that increases the velocity of the particles entering the extraction resonance, thus reducing the intensity fluctuations of the extracted beam;
- separated functions for the high-energy beam lines to scan the tumor in both the dimensions independently;

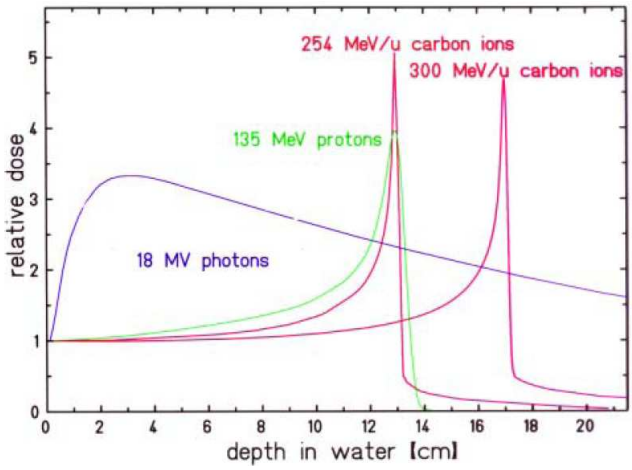

(a)

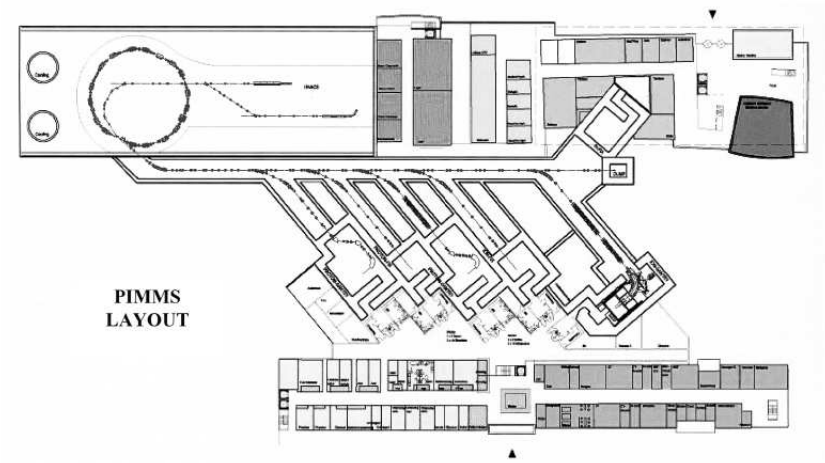

(b)

Figure 1.13: a) The Bragg peak: dose deposit of photons, protons and carbon ions in water. b) General layout of the PIMMS design study.

- a mobile cabin gantry for carbon ions;
- rotators to make the beam optics of each gantry completely independent of the gantry rotation angle.

The studies of proton beams (typically used at 230 MeV) and carbon ions (with an energy up to 430 MeV/nucleon) have been performed in order to evaluate the behavior of each single cell within a treated tissue. For these studies a low size beam is necessary (of the order of a few hundred microns), while for the patient treatments a FWHM (Full Width Half Maximum) beam size at the patient in the

range 4 to 10 mm is requested [26].

In addition to radiotherapy related topics, a possible application of biological studies with microbeams is represented by the pioneeristics characterization of single cell behaviors in a cosmic environment performed by the National Aeronautics and Space Administration (NASA) at the NASA Space Radiation Laboratory (NSRL) at the Brookhaven National Laboratory (BNL) [27]. Many questions, in fact, are common to radiotherapy and space studies:

- carcinogenesis which is a concern both for astronauts involved in long-term missions and young patients;
- radioprotection;
- individual sensitivity.

For both the applications, studies using microbeams are necessary.

1.2.2 Environmental studies

Different microbeam applications can be found in the environmental field with excellent results: an important example is represented by elemental analysis, which is one of the analytical processes that can be used to identify sources of pollution in several environments by stormwater analysis [28] or cosmic materials in a meteorite [29].

The extracted samples are prepared before the analysis with standard procedures: for the pollution analysis, for example, each sample is passed through a coarse 2 mm screen to remove organic debris and then through a 250 μm nylon screen into a pre-cleaned container. Samples are then filtered by papers to separate particles depending on their size in two groups: 0.4-60 μm and 60-250 μm.

The elemental analysis is provided by a PIXE (Particle Induced X-ray Emission) system in the following way: a 2.5 MeV proton beam (with a current of 5 nA) is focused on targets with a minimum spot size of 10 mm in diameter. The filter targets are mounted on an automatic sample changer used for air particulate studies. The characteristic X-rays generated by the sample are detected by a Si detector with a 25 μm Be absorber. In order to improve the sensitivity for the higher Z elements, a second X-ray detector with a 25 μm Al absorber is used. Figure 1.14 shows the spectrum of a stormwater particulate sample as obtained with a PIXE analysis.

1.2.3 Physics & art: a microbeam factory

PIXE systems are also used for applications regarding art: these non-invasive methods are used to analyze the materials which form the artwork, as described

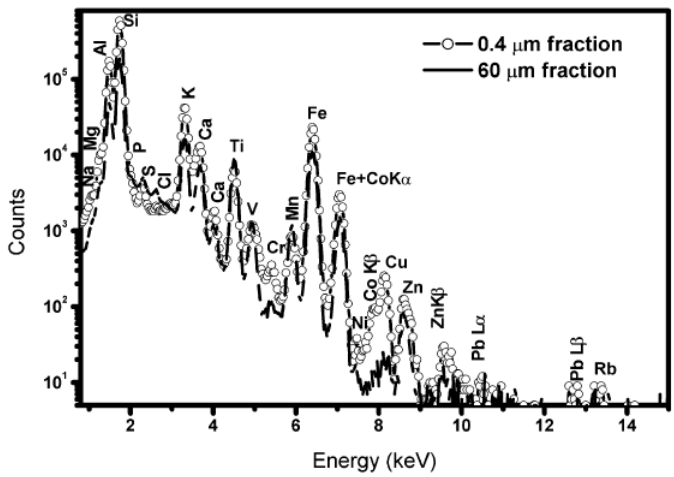

Figure 1.14: PIXE spectrum of a stormwater particulate [28].

in [30, 31]. In particular, in this section a brief description of a typical setup used in ”artwork physics“ is given [32]: this allows to better understand a microbeam facility and the possible applications of crystals in this framework.

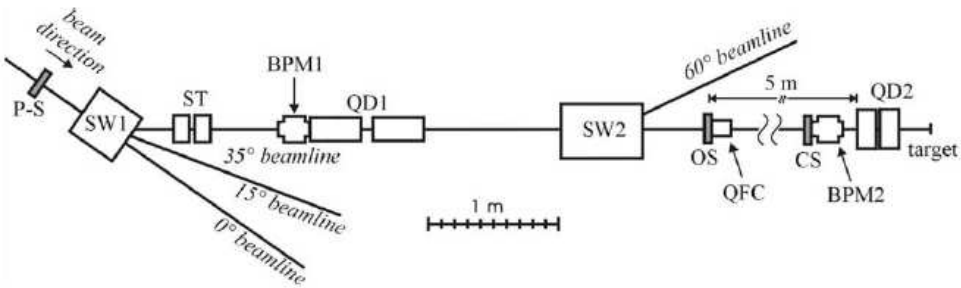

Figure 1.15: An example of a microbeam facility for art studies [32].

Figure 1.15 shows an example of a microbeam facility: the proton beam coming from a 3 MV Van der Graaff accelerator is selected by a deflector magnet and then passes through a series of pre-slits (PS) to regulate the current before being deflected by a switching magnet. A beam profile monitor (BPM1) is positioned in front of the quadrupole lenses (QD1) and a beam diagnostic stage, consisting of a Faraday cup and a quartz beam viewer. A set of collimating slits is positioned before a strong focusing (QD2) quadrupole to reduce aberrations, while a second BPM is located after the collimating slits.

The performances of this facility are very good: the dimensions of the beam spot are 12 ± 2 μm in X and 11 ± 2 μm in Y full width at 1/100 maximum

(FW1/100M) for a current of about 1 nA.

PIXE with an external beam produced by such a microbeam factory has been used in several ”artwork physics“ applications. Among these, the results of an elemental study on inks of ancient manuscripts can be cited [33]. Before the invention of printing, the inks were mixtures of several elements, from vegetable essences to mineral salt; the writing properties of inks are largely dependent on the ratios of the ingredients. In order to evaluate the elements which form an ink, a PIXE setup has been used: the beam runs lasted typically 150 s per spot with a proton current of 250-500 pA and a beam diameter of 200 μm FWHM (provided by the microbeam factory described above). The elements detected by the PIXE setup have been Na, Mg, Al, Si, P, S, Cl, K, Ca, Fe, Cu, Zn and Pb; the typical elemental spectra are shown in figure 1.16.

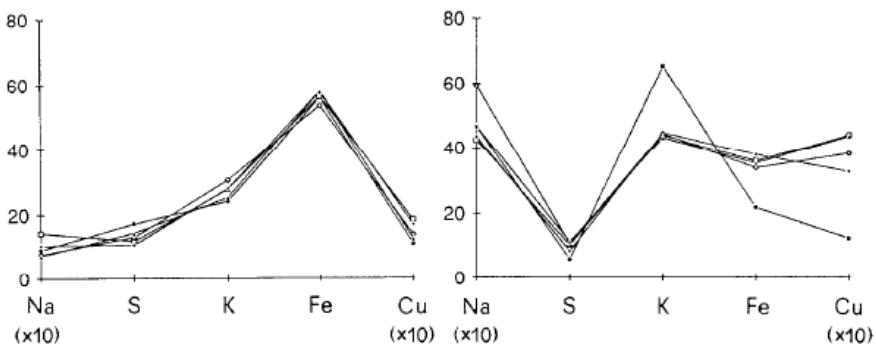

Figure 1.16: Number of counts for several elements in two pages of the analyzed manuscript. Different results in each spectrum refer to five different regions in each page where the analysis has been performed [33].

1.2.4 The microbeam and the crystal option

Even if bent crystals have been developed for beam extraction or collimation, they can be used in microbeam applications in two ways: beam focusing and nanotube channeling [34].

There are several methods to focus a beam using a bent crystal [35], many of which have disadvantages due to the background from the unchanneled beam fraction; a particular technique where a parallel beam is focused into a strip reducing background events will be briefly described.

Figure 1.17(a) shows this beam focusing method: the main feature is the specific shape of the bent crystal back end face, so that the tangential to the crystallographic planes (more details in chapter 2) on this surface cross the same line.

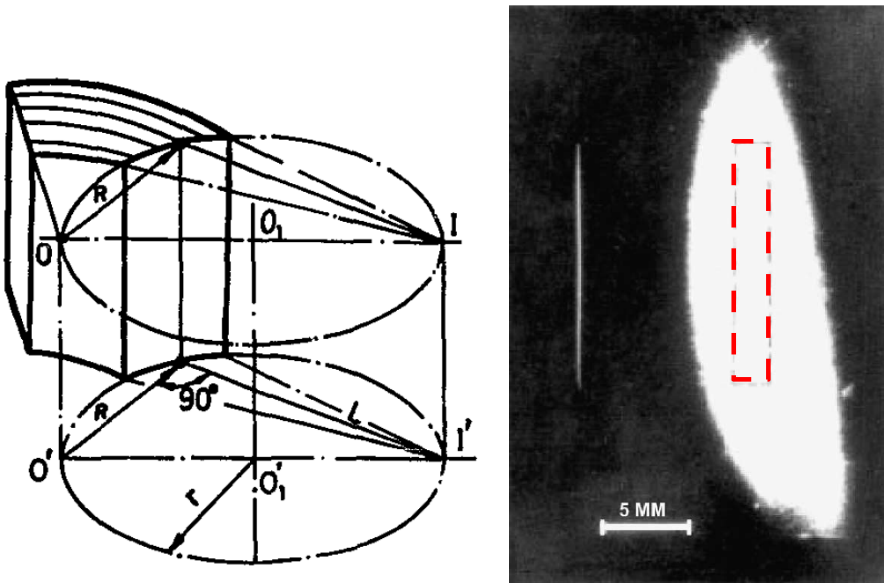

(a) (b)

Figure 1.17: a) The principle of beam focusing with a bent crystal. b) The profile of the deflected and focused beam is on the left, while the red dashed rectangle on the right is the crystal cross-section [34].

Considering the crystallographic planes which are curved following a cylinder of radius R, it is necessary that the line with the centres of curvatures O and O$'$ is placed on the surface of the cylinder which gives the shape to the crystal end face. In the case of a perfectly cut and bent crystal, the beam size at the focused point is provided by the product of the focal distance $L = (4r^2 - R^2)^{1/2}$ and the critical channeling angle ϕ, which depends on the crystal shape. The focal length is defined as:

$$F = \frac{2L\phi}{H}$$

where H is the crystal width.

A lot of tests have been performed with 70 GeV proton beams (IHEP) with different focal lengths (figure 1.17(b)) obtaining a measured beam size RMS in the focal plane of 21 μm. This technology has been developed and optimized for high energy (the beam size at the focal plane is of the order of a few tens of microns for a GeV beam and should be a few microns for a TeV one), but recent developments in the crystal technology will allow to test focusing also at a medium energy ($\sim$MeV).

As far as the nanotube channeling is concerned, there has been a large interest about the use of the channeling phenomena in carbon nanotubes to provide a microbeam. Carbon nanotubes are cylindrical molecules (figure 1.18) with a typical

diameter of the order of 1 nm for a single-wall nanotube, or tens of nanometer for multi-wall nanotubes.

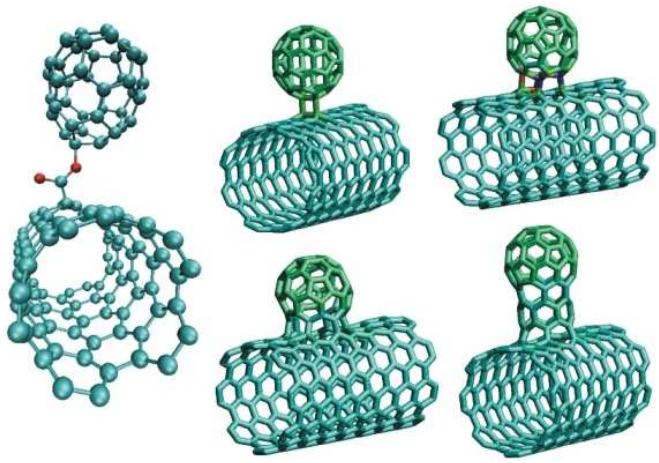

Figure 1.18: Simulation of several nanotube structures. Picture extracted from the web site: http://www.wikipedia.org

The channeling phenomena in nanotube structures occur when a particle is confined in a 2D potential which is localized very close to the wall as shown in figure 1.19(a).

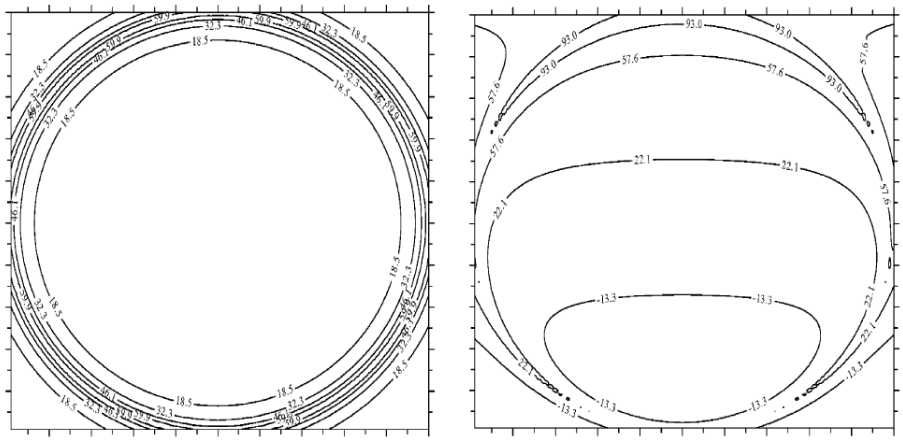

(a) (b)

Figure 1.19: a) The continuous potential within a carbon nanotube of 1.1 nm. b) The same nanotube bent with: $pv/R = 1$ GeV/cm [34].

In order to steer particles, a nanotube can be bent and the potential wall is thus modified by the centrifugal force (chapter 2): figure 1.19(b) shows the potential

wall in a nanotube which is bent of $pv/R = 1$ GeV/cm, where R is the curvature, p the particle momentum and v the velocity. To understand the bent nanotube efficiency, Monte Carlo simulations of positive particle channeling have been performed: figure 1.20 shows the number of channeled particles as a function of the nanotube curvature for different nanotube structures (single-wall and multi-wall) and for a Si (110) crystal.

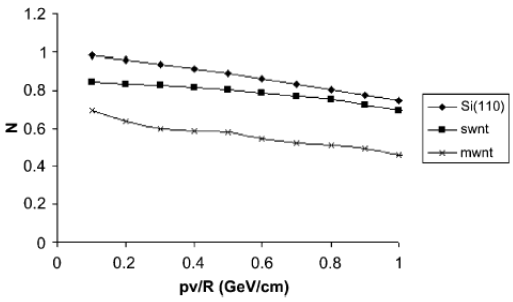

Figure 1.20: Number of channeled particles as a function of the nanotube curvature for single-wall (SWNT) and multi-wall (MWNT) nanotubes and for a silicon (110) crystal [34].

Two approaches can be considered to create a microbeam with nanotubes: the trapping of a small fraction of the incident beam which is then steered away to reduce the emittance with well-defined sharp edges; the arrangement of a focusing array of bent channeling nanotubes that focus the channeled particles into a small spot. The first solution seems to guarantee better results: some experiments in IHEP have evaluated the nanotube performances in terms of efficiency and radiation hardness with good results [34].

1.3 Synchrotron radiation sources and crystal undulators

High energy photons are used in several fields thanks to their penetration capability. In high energy physics, different radiation sources are provided in a synchrotron, a circular accelerator ring where charged particles are bent by magnets and are accelerated by radiofrequency cavities.

In this section a brief description of the radiation emitted by bending magnets, undulators and wigglers in a synchrotron accelerator in terms of spectrum, shape and intensity is given. In this field, specific bent crystals (called ”crystal undulators“) can play an important role: thanks to their intrinsic features, they can

provide high intensity spectra and can substitute the electromagnetic undulator as a radiation source.

1.3.1 Synchrotron radiation: dipoles, undulators and wigglers

Synchrotron radiation is one of the most important sources of high energy photon beams. It became available in the early '80s and, from there on, it has been used in several fields, from chemistry to material science, from medicine to biology [36].

Synchrotron radiation is emitted in a so-called synchrotron accelerator, where relativistic electrons are accelerated and injected into a storage ring within a nominal orbit by applying a constant magnetic field (provided by bending magnets). In the bending magnets, synchrotron radiation (or *dipole radiation*) is emitted tangentially to the beam in a very small angle; the lost energy is replenished by radiofrequency cavities. Radiation can also be produced in the straight sections (*insertion devices*) between the bending magnets, where photon beams are generated in magnetic devices called *undulators* and *wigglers*. The radiation emitted by these sources is different in terms of intensity and spectrum.

The radiation from a classical charged particle travelling in a circular orbit (of radius R) due to a magnetic field B is emitted isotropically at the Larmor frequency. However for a relativistic particle[5], the radiation is relativistically collimated in the forward direction and is Doppler shifted, in a stationary frame (figure 1.21).

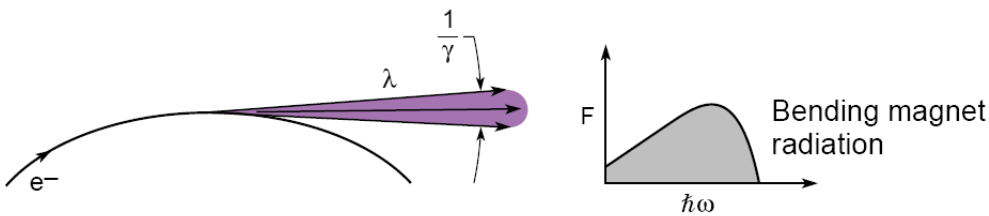

Figure 1.21: Left: synchrotron radiation is emitted in a cone with an aperture $1/\gamma$. Right: synchrotron radiation energy continuous spectrum [37].

The spectra properties of the radiation emitted by ultra relativistic charged particles in a dipole can be expressed as [38]:

$$\frac{\mathrm{d}I(\omega)}{\mathrm{d}\Omega} = \frac{3e^2\gamma^2}{4\pi^2 c}\left(\frac{\hbar\omega}{\hbar\omega_c}\right)(1+\gamma^2\psi^2)\left[K_{2/3}^2(\xi) + \frac{\gamma^2\psi^2}{1+\gamma^2\psi^2}K_{1/3}^2(\xi)\right] \tag{1.1}$$

[5] In synchrotron accelerators, electrons and positrons can typically have an energy between 0.5 and 5 GeV.

where

$$\xi = \left(\frac{\hbar\omega}{2\hbar\omega_c}\right)(1+\gamma^2\psi^2)^{3/2} \tag{1.2}$$

and

$$\hbar\omega_c = \frac{2\hbar c\gamma^2}{2R} \tag{1.3}$$

is defined as the *characteristic energy*, because half of the power is irradiated above it. γ is the electron energy in units of its rest energy, ψ is the angle perpendicular to the orbital plane and $K_x(\xi)$ is the modified Bessel function of order x.

From equation 1.1 it is possible to note that most of the synchrotron radiation is confined in the orbital plane within an instantaneous emission cone of half width $1/\gamma$ (right plot in figure 1.21) with photon energies smaller than $4\hbar\omega_c$.

In the insertion devices, the radiation is produced in the undulator and wiggler magnets which in practice are periodic structures of dipole magnets (as shown in figure 1.22) [38] where a static magnetic field is alternating along the length of the undulator with a wavelength λ_u.

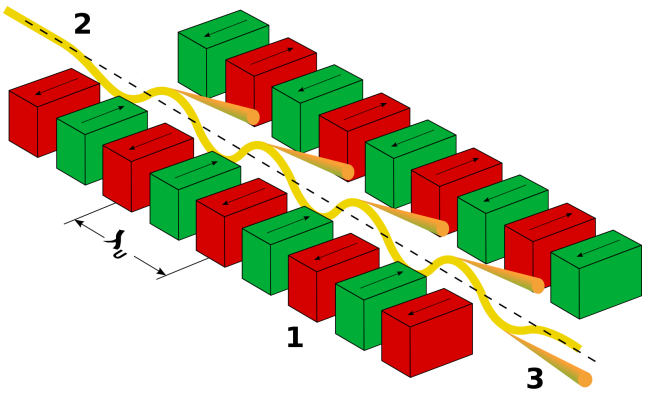

Figure 1.22: Undulator: alternated magnets (1), electron beam (2) and undulator radiation (3).

Electrons crossing the periodic magnet structure are forced to undergo oscillations and radiate. The curvature of the electron in a wiggler magnet is severe and the total intensity is the sum of the intensity of each structure. On the other side, undulator magnets deflect the electron of a quantity smaller than the photon opening angle, generating interference between the electron and the photon it has emitted and breaking the continuous spectrum into a harmonic series. Figure 1.23 shows the energy spectrum coming out from the undulator: it is very intense and concentrated in narrow energy bands (corresponding to the lower harmonics of the

fundamental wavelength) and it is also collimated on the orbit plane of the electrons; the photon beam is almost monochromatic and with an intensity of $\sim N^2$, where N is the number of sections.

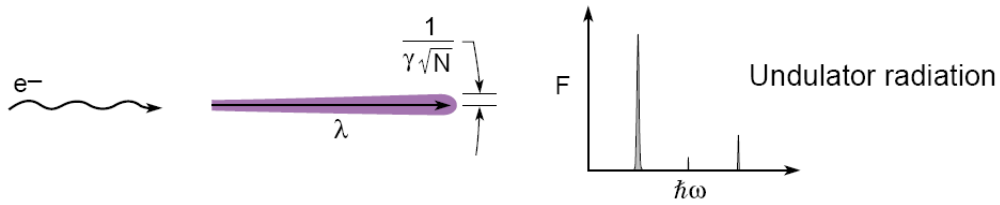

Figure 1.23: Left: undulator radiation cone. Right: radiation energy spectrum from an undulator magnet [37].

To be more quantitative, the relative spectra bandwidth of an electron which undergoes N oscillations is:

$$\frac{\Delta\lambda}{\lambda} = \frac{1}{N} \tag{1.4}$$

The undulator equation (where K is a dimensionless parameter, see later on) [37]:

$$\lambda = \frac{\lambda_u}{2\gamma}\left(1 + \frac{K^2}{2} + \gamma^2\theta^2\right) \tag{1.5}$$

can be written twice, once for on-axis radiation (θ=0) and once for off-axis wavelength-shifted radiation at an angle θ:

$$\frac{\lambda_u}{2\gamma^2} + \Delta\lambda = \frac{\lambda_u}{2\gamma^2}(1 + \gamma^2\theta^2) \tag{1.6}$$

The two equations can then be divided:

$$\frac{\Delta\lambda}{\lambda} \simeq \gamma^2\theta^2 \tag{1.7}$$

Considering equations 1.4 and 1.7, the *central radiation cone* is defined as:

$$\theta \simeq \frac{1}{\gamma\sqrt{N}} \tag{1.8}$$

as shown in figure 1.23.

For an undulator with N periods, the brightness can be up to N^2 more than a bending magnet: the first factor N is due to the constructive interference of the fields emitted during the N radiation periods at the harmonic wavelengths; the second N factor derives from the reduction of the emission angle associated

with these harmonics, which goes as $1/N$. When the electrons come with half the period, they interfere destructively, and the undulator stays dark.

In order to define the difference between wiggler and undulator magnets, a dimensionless parameter must be considered:

$$K = \frac{eB\lambda_u}{2\pi m_e c} \tag{1.9}$$

where e is the electron charge, B the magnetic field, m_e the electron rest mass and c the speed of light; K characterizes the nature of the electron motion. Using the K parameter, a general definition of the deflection angle can be given:

$$\theta \simeq \frac{v_x}{v_z} \simeq \frac{v_x}{c} \simeq \frac{K}{\gamma} \tag{1.10}$$

where v_z is the particle velocity along the beam and $v_x \simeq \frac{Kc}{\gamma}$ the transverse velocity.

For $K \ll 1$ the oscillation amplitude is small and the radiation displays interference patterns which lead to narrow energy bands (*undulator* case); on the other side, if $K \gg 1$ the oscillation amplitude is bigger and the radiation contributions from each field period sum up independently, leading to a broad energy spectrum: in practice the contribution of higher harmonics rapidly increases [38]. In this regime of fields the device is called *wiggler*. Figure 1.24(a) shows the wiggler energy spectrum: when the contribution of each single harmonic is added, a continuous spectrum appears.

The wiggler radiation is emitted in a cone of $\theta \simeq \frac{K}{\gamma} \gg \frac{1}{\gamma}$, according to equation 1.10, as shown in figure 1.24(b).

The intensity and the brilliance of the radiation emitted by undulator and wiggler magnets are larger than the synchrotron one as shown in figure 1.25: for the undulators this is due to the interference effects that occur between the emitting particle and the emitted photons; for wigglers it is simply due to the fact that the electrons (or positrons) are bent in the device more than once.

1.3.2 Crystal undulator (CU)

The crystal undulator idea has been developed to increase the energy of a photon emitted in an undulator [40]. This energy is defined as:

$$\hbar\omega = \frac{2\pi\hbar\gamma^2 c}{L} \tag{1.11}$$

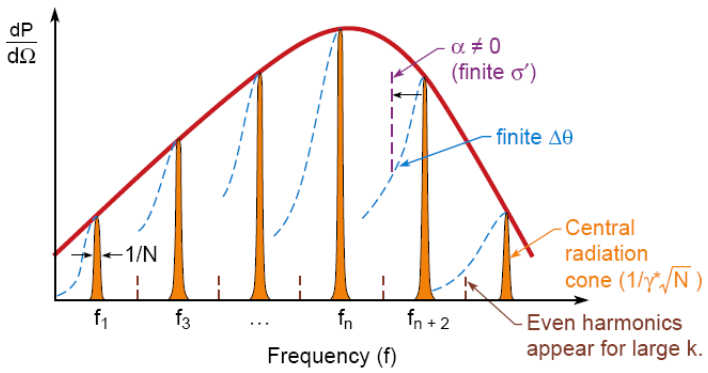

(a)

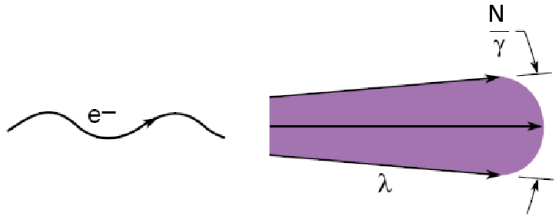

(b)

Figure 1.24: a) The wiggler continuous spectrum. b) The wiggler emitted radiation cone [37].

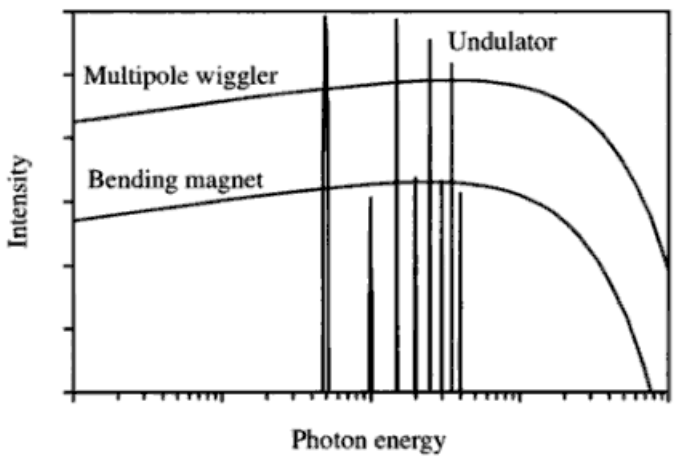

Figure 1.25: Synchrotron radiation from bending magnets, multiple wigglers and undulators (on a log-log scale) [39].

where γ is the Lorentz factor and L is the undulator period. The typical electromagnetic undulators minimal period L is limited to several millimiters, which

corresponds to low energy photons (up to a few keV). The big improvement provided by the crystal undulator (CU) is given by the submillimeter range of the period L. The crystallographic planes (chapter 2) can be periodically deformed and generate equivalent electromagnetic fields of the order of 1000 T: in these conditions the radiation intensity increases with respect to the electromagnetic case.

To obtain crystal undulators, different ideas have been proposed. The most recent one is based on the use of microgrooves on the crystal surface. X-ray experiments have observed that such a microgroove generates a stress strong enough to create a crystalline undulator. The first observation was made at IHEP with a 70 GeV proton beam [41]: it was found that micro-scratches on a crystal surface cause a significant deflection of the crystallographic plane (figure 1.26(a)). Exploiting the channeling effect for a particle in a deflected channel, it is possible to create a CU by making a periodic series of microgrooves on the crystal surface (figure 1.26(b)).

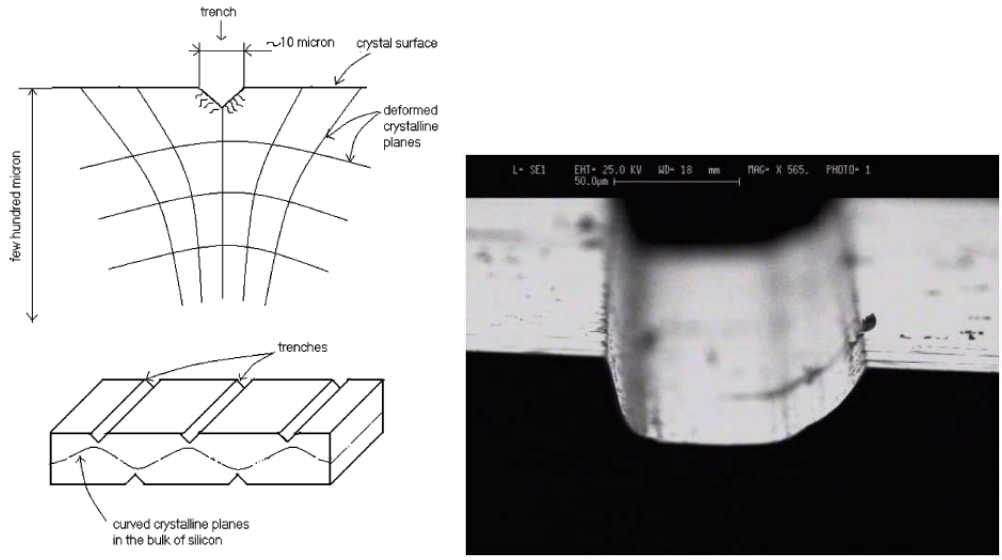

(a) (b)

Figure 1.26: a) Top figure: crystallographic plane distorsion near a surface scratch; bottom figure: crystal undulator scheme [42]. b) Example of a microgroove on the crystal surface [43].

Microgrooves are created with a special diamond blade (or scriber) which scratches the crystal plate with a set of parallel grooves [40]. Several ways of grooving were tried and the optimization is going on [44]: the size of the grooves and the pressure of the scriber are found empirically, aiming at producing the maximum effects without breaking the crystal.

Crystal undulators are characterized via X-ray measurements [44]: a X-ray beam is collimated to 2 mm in height and 40 μm in width and it is made to impinge on the sample surface. The sample can be translated with high accuracy (1 μm and 1 arcsec) by use of a standard theodolite; X-rays are detected by a NaI counter. Figure 1.27(a) shows the measured angles as a function of the beam incidence position at the crystal surface using a X-ray facility; the position of each single microgroove is clearly visible.

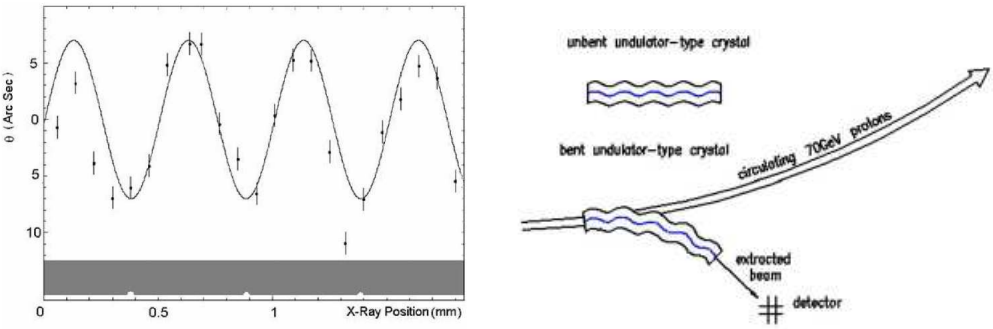

(a) (b)

Figure 1.27: a) X-ray test of a crystal undulator. b) A crystal undulator test on a circulating high-energy proton beam [42].

Experimental tests have been done on a crystal undulator (0.3-0.5 mm thickness, 10 periods, an oscillation amplitude $A \approx 100$ Å, 5 mm length along the beam), evaluating both the deflection of charged particles and the photon spectra emitted by the crystal itself.

The tests have been performed at IHEP with a 70 GeV proton beam as shown in figure 1.27(b): a crystal has been bent by a mechanical holder (see chapter 2) of an angle of 1 mrad which is enough to separate the primary and the deflected beam. The crystal behavior has been evaluated with a secondary emission detector in a vacuum tank as a function of the alignment between the beam and the crystallographic planes. The results are schematically shown in figure 1.28: the left figure corresponds to the disalignment position where only the beam scattering tail is seen; the right figure shows the channeling alignment position: in this case the efficiency is equal to 31%, while for a bent crystal without microgrooves it should be 45%. Thus the measurements show that a bent crystal undulator deflects protons with a good efficiency but just 70% of the crystal cross-section is available for channeling.

However, the most important aim of a crystal undulator is to produce a high-energy photon beam using electrons and positrons. At present two setups have been developed: at LNF (Frascati, Italy) with a 500-800 MeV positron beam [44]

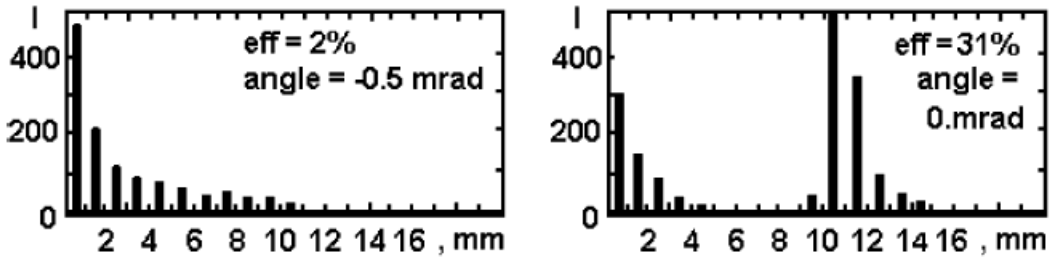

Figure 1.28: Deflection beam profile and efficiency for two values of the crystal orientation angle: amorphous on the left, perfect channeling alignment on the right [42].

and at IHEP with a 3 GeV positron beam. The typical setup is shown in figure 1.29: a crystal undulator on a remotely controlled goniometer system has been put in a vacuum tank to reduce the background events. The incoming positrons impinge on the crystal undulator which has been first aligned with respect to the beam with a laser system (further information in section 3.5.1). After the crystal, a bending magnet cleans the photon beam from charged particles. A NaI(Tl) crystal has been used as a detector for the photons; a 59 keV ^{241}Am and a 1.15 MeV ^{60}Co sources have been employed to calibrate the photon detector.

Waiting for the first experimental results, the expected photon spectrum has been calculated for a silicon undulator crystal. A theoretical explanation is given in section 2.3.3: the energy loss by the light leptons in the volume reflection orientation can be described as the contribution of an undulator and a synchrotron component.

The radiation is typically determined by means of the dimensionless parameter:

$$\rho = 2\gamma^2 \langle v_t^2 - v_m^2 \rangle / c^2$$

where $\langle v_t^2 - v_m^2 \rangle$ is the squared mean deviation of the transverse velocity from its mean value v_m, γ is the Lorentz factor and c the speed of light. If $\rho \leq 1$ the total radiation spectrum is just the sum of the undulator and channeling spectra, while if $\rho \gg 1$, the spectrum is similar to the synchrotron radiation one. According to the hypothesis $\rho \leq 1$, the expected energy spectrum can be computed for different energies (figure 1.30).

Figure 1.30(a) shows the photon spectrum for 800 MeV positrons ($\rho < 1$), while figure 1.30(b) shows the 3 GeV case, where ρ is approximately 1: from theory, in fact, it is possible to estimate $\rho = \gamma\theta_b$ (where $\theta_b = U/mc^2$, m is the particle mass and U is the planar potential barrier, see section 2.3.3).

For the 800 MeV (3 GeV) case a clear peak is visible at 55 keV (500 keV), while the energy reaches 2.5 MeV (16 MeV). The photon absorption process in

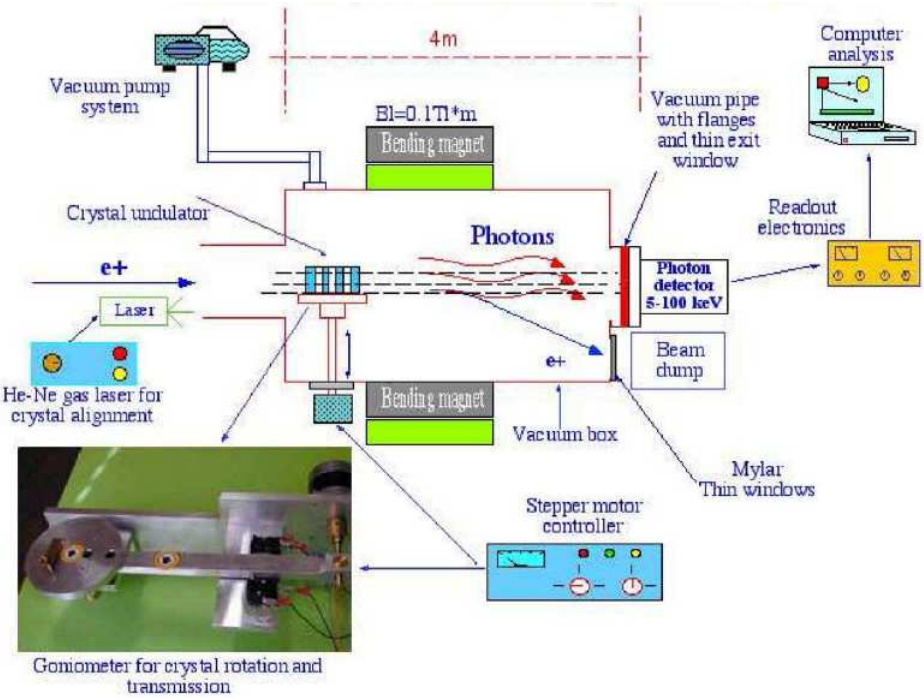

Figure 1.29: Schematics of the setup to measure the photon emission in a crystalline undulator [44].

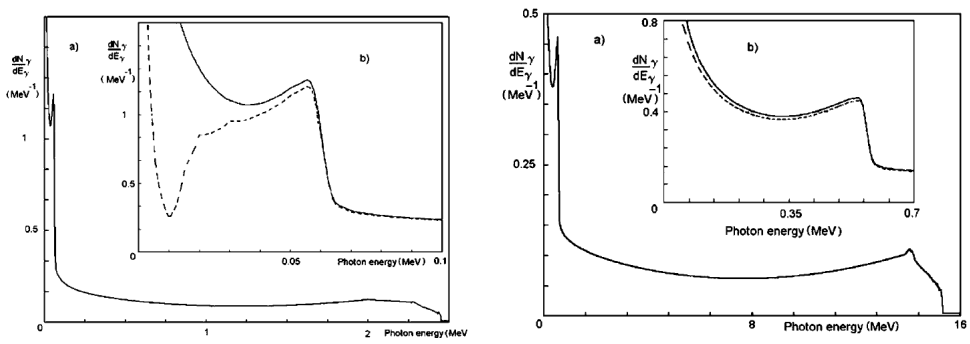

(a) (b)

Figure 1.30: a) The expected photon spectrum for 800 MeV and b) for 3 GeV positrons. The dashed curve is the photon spectrum taking into account the absorption process of photons in the body of the undulator [44].

the body of the undulator is an important factor and has been taken into account, as shown by the dashed lines in figure 1.30. In simulation some contributions (like the influence of the length of a single crystal and of the quasi-channeled process)

are not completely considered.

Chapter 2

The physics of crystals

In this chapter a brief overview of the physics and the motion of a charged particle in a bent crystal is given. J. Stark was the first in 1912 [45] to discover that certain directions in a crystal are more transparent to charged particles with respect to the amorphous material: this phenomenon was called *channeling*.

Starting from this, an interesting idea was proposed by E. H. Tsyganov in 1976 [46, 47]: when a crystal is bent, a charged particle (which impinges on it with a certain angle) follows the channel and is steered with a large deflection angle. In a bent crystal not only the channeling phenomenon occurs: depending on the angle between the crystallographic plane and the incoming particles trajectory, an effect called *volume reflection* can take place, that is charged particles can be reflected by the interatomic planes with high efficiency. The acceptance of this phenomenon (the angular region where it can occur) is larger than the channeling one, corresponding in practice to the channeling deflection angle.

The characterization of the channeling related phenomena in bent crystals has been performed at different energies with positive and negative particles. In particular, the last section of this chapter gives an overview of the theoretical bases of the radiation emitted by electrons and positrons in a channeling and a volume reflection orientation. The experimental results of the phenomena described here will be shown in detail in chapter 4.

2.1 Looking inside a straight crystal

The aim of this section is to describe the structure of a crystal and the effects which take place in a straight crystal depending on the angle of the particle with respect to the crystallographic planes.

2.1.1 The structure of crystals

Crystals are characterized by an ordered and symmetrical arrangement of the atoms. The crystal spatial structure, that is called *lattice*, consists of a grid of straight lines (which represent the interatomic bonds) and vertices (or nodes, corresponding to the single atoms in the simplest case) and has an infinite number of different translation periods. The primitive cell of the lattice is a parallelepiped which is characterized by the distance between the vertices in three dimensions and the angles (α, β and γ) among bonds.

Different combinations of several symmetries (translation, rotation and reflection) lead to fourteen so-called Bravais lattices, grouped in seven systems: cubic, tarragon, orthorhombic, monoclinic, rhomboidal and triclinic. In particular the cubic system has three crystal *sub*-lattices: the simple cubic lattice, the body centered cubic (bcc) and the faced centered cubic (fcc).

The crystal planes and axes are described by the so-called Miller indices that can be derived from the equation of the plane:

$$\frac{x}{x_0} + \frac{y}{y_0} + \frac{z}{z_0} = 1 \tag{2.1}$$

where x, y, z are the coordinates of an arbitrary point in the plane and x_0, y_0, z_0 are the coordinates of the intersections between the plane and the axes. Considering the coordinates n_j of any lattice node and a common divider m, the equation of the plane can be re-written in the following way:

$$hn_1 + kn_2 + ln_3 = m \tag{2.2}$$

where

$$h = \frac{m}{x_0}, \quad k = \frac{m}{y_0}, \quad l = \frac{m}{z_0}$$

From now on, each plane will be described using the Miller indices (h,k,l). In particular, the planes parallel to the coordinate axes are indicated as (100), (010) and (001). The main planes of the simple cubic lattice (described by round brackets) are shown in figure 2.1, while the axes are described by Miller indices within square brackets (i.e. [hkl]).

The typical crystals used for the study of channeling phenomena in accelerators are carbon (or diamond), silicon, germanium and tungsten: the internal structure of these materials is described by the diamond lattice, that is a face centered cube structure (figure 2.2) formed by the covalent bonds due to the four electrons in the outer shell.

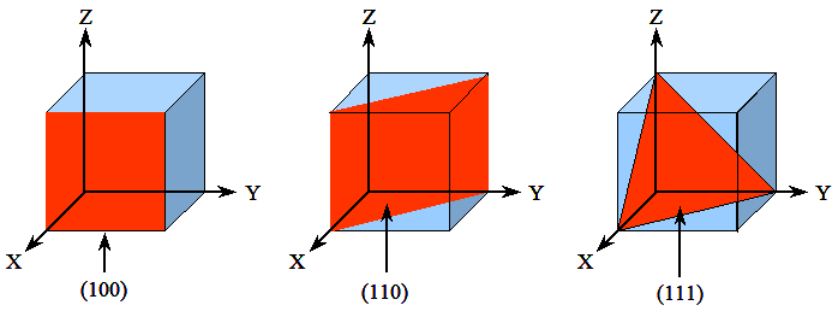

Figure 2.1: The main planes of the simple cubic lattice.

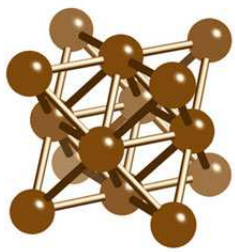

Figure 2.2: The diamond crystal structure is a face centered cubic.

2.1.2 The potential in a crystal

A particle motion in an amorphous material or in a misaligned crystal (see section 2.1.3) could be described like a number of *uncorrelated* collisions with the single atoms. In these cases, several processes can occur (mainly multiple scattering with atomic nuclei and energy loss in collisions with atomic electrons), depending on the impact parameter value.

However, the intrinsic crystal structure allows to reduce these effects. The interest in crystals started in 1912 when a German physicist, J. Stark [45], underlined the transparency of certain crystal orientations with respect to the direction of the incident particles. His theory was confirmed by several simulations and experiments in the early '60s, when the channeling effect was discovered using ions.

In 1964, the theoretical explanation of the channeling effect was formulated by J. Lindhard [48] who demonstrated that when a charged particle impinges on the crystal with a small impact parameter with respect to the crystallographic axis (or plane) a number of correlated collisions with the crystal lattice atoms occurs. The potential of each atom could be replaced with an average *continuous potential* in the approximation of a small incoming angle with respect to the atomic planes as shown in figure 2.3.

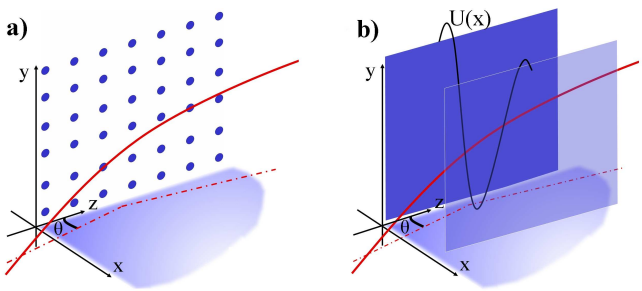

Figure 2.3: a) Motion of a particle (red line) misaligned with respect to the crystal axis but with a small impact angle with respect to the plane ones. In this case the continuous potential approximation is valid and the particle feels the average potential (black line) due to the plane (as shown in b).

The continuous potential is defined as:

$$U_{pl}(x) = Nd_p \int_{-\infty}^{+\infty} \int_{-\infty}^{+\infty} V(x,y,z)\mathrm{d}y\mathrm{d}z \tag{2.3}$$

where N is the volume density of the atoms, d_p is the interplanar spacing and $V(x,y,z)$ is the potential. The potential can be computed considering the Thomas-Fermi theory of the atom, which describes a particle-atom interaction as:

$$V(r) = \frac{Z_i Z e^2}{r} \Phi\left(\frac{r}{a_{TF}}\right) \tag{2.4}$$

where $Z_i e$ is the particle charge, Z the atomic number and r the distance between the particle and the atom. The expression can be divided in two parts: a point-like charge potential and a screening function $\Phi(r/a_{TF})$, where a_{TF} is the Thomas Fermi screening distance ($a_{TF} = 0.8853 a_B Z^{-1/3}$, with a_B = 0.529). Two analytical approximations of the screen function can be given: equation 2.5 presents the Molière expression, and equation 2.6 the Lindhard one[1]:

$$\Phi\left(\frac{r}{a_{TF}}\right) = \sum_{i=1}^{3} \alpha_i \exp\left(-\frac{\beta_i r}{a_{TF}}\right) \tag{2.5}$$

$$\Phi\left(\frac{r}{a_{TF}}\right) = 1 - \left(1 + \frac{3a_{TF}^2}{r^2}\right)^{-1/2} \tag{2.6}$$

The Molière expression is given by the weighted sum (with the weight α_i) of three exponential contributes (β_i). Considering Lindhard's approximation, the

[1] In this thesis work the Lindhard approximation is considered.

continuous potential becomes:

$$U_{pl}(x) = 2\pi N d_p Z_i Z e^2 \left(\sqrt{x^2 + 3a_{TF}^2} - x\right) \tag{2.7}$$

To complete the scenario, another aspect should be considered: the atomic thermal vibrations that cause distorsions in the lattice structure. This effect is independent and small with respect to the other one and can be described with a Gaussian law: at 300 K the RMS displacement of the silicon atoms is $\rho = 0.075$Å, while the lattice constant is $L_c = 5.431$Å. The thermal vibration effect becomes important at a small distance from the atomic planes where the infinite static potential has to be modified to have a finite maximum: the typical potential in the Molière approximation is shown in figure 2.4.

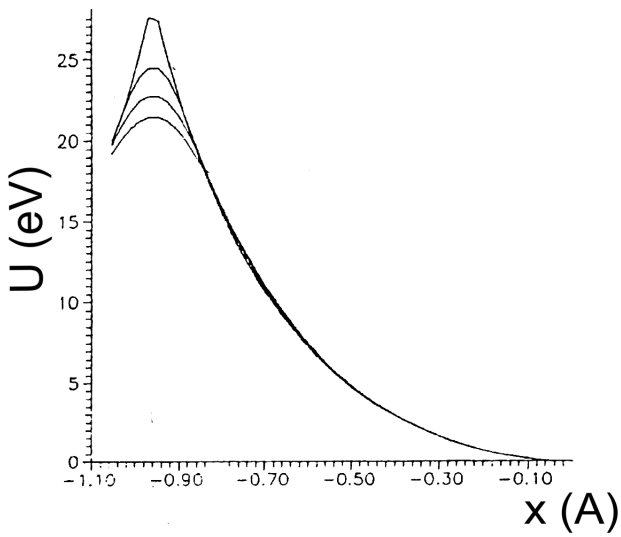

Figure 2.4: The (100) silicon potential in the Molière approximation at different temperatures; from the top: 0 K, 77 K, 300 K and 500 K.

The charged particles feel an effective potential which is defined as:

$$U(x) \approx U_p l\left(\frac{d_p}{2} - x\right) + U_p l\left(\frac{d_p}{2} + x\right) - 2U_p l\left(\frac{d_p}{2}\right) \tag{2.8}$$

where the first two terms describe the contribution of the two nearest planes, while the third term considers the potential at the origin ($U(0) = 0$), where the origin of the coordinate x is chosen in the middle of the two atomic planes.

Table 2.1 shows the planar channel parameter values for the typical materials used in high energy physics: silicon, germanium and tungsten; these crystals are characterized by the diamond crystal structure as described in section 2.1.1.

Figure 2.5 shows the interplanar Molière potential for the (110) and (111) silicon crystals. The dashed line is the harmonic potential approximation.

	Channel	$L_c[\dot{A}]$	$d_p[\dot{A}]$	$a_{TF}[\dot{A}]$	$\rho[\dot{A}]$	Z	$U(x_c)$[eV]
Si		5.43		0.194	0.075	14	
	110		1.92				16
	111L		2.35				19
	111S		0.78				4.2
Ge		5.65		0.148	0.085	32	
	110		2.00				27
	111L		2.45				30
	111S		0.81				7.2
W		3.16		0.112	0.050	74	
	100		1.58				63
	110		2.24				105

Table 2.1: Main parameters of the silicon, germanium and tungsten planar channels. The potentials are given by the Molière approximation and $x_c = d_p/2 - 2/\rho$.

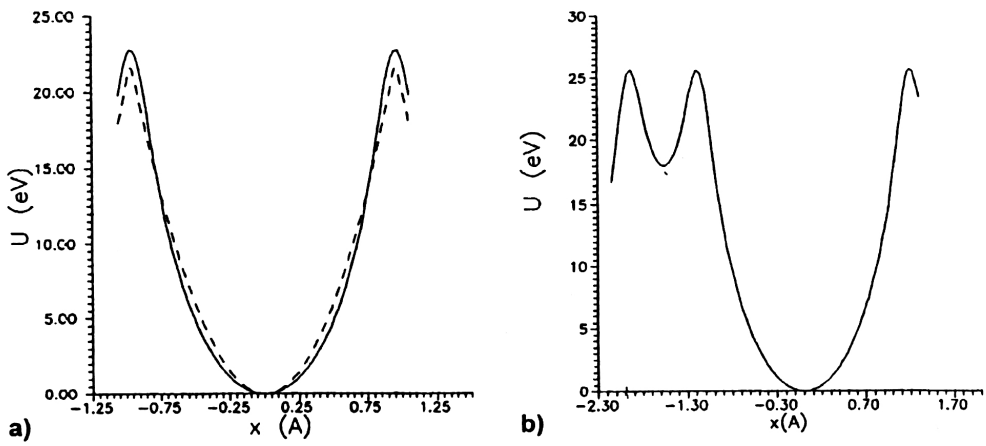

Figure 2.5: The interplanar potential for the a) (110) and b) (111) silicon channels. The dashed curve represents the harmonic potential approximation.

2.1.3 Particle motion in a crystal: channeling

From the considerations of the previous section, it is possible to describe the behavior of a charged particle moving in a channel: this motion is called *channeling*.

There are two different types of channeling: *axial channeling*, when particles are trapped in an atomic string (that is particles are trapped in a channel in the vertical and horizontal directions), and *planar channeling* (or, simply, *channeling*), when particles oscillate between two atomic planes (that is just a direction is considered).

A channeled proton (as described in this thesis work, see chapters 3 and 4) moves within the interatomic planes without colliding with the nuclei but in a medium of electrons with a low density which can reduce its momentum: for light particles this coherent effect increases the probability to irradiate a photon.

Lindhard [48] described his theory in the framework of classical mechanics and this approach is verified if the particle energy increases. The use of the classical approach can be justified by the harmonic potential approximation:

$$U(x) = U_0\left(\frac{2x}{d_p}\right)^2$$

where U_0 is the potential depth. In this approximation the energy spacing between potential levels is $\hbar\left(\frac{8U_0}{d_p^2 M_\gamma}\right)^{1/2}$, where M_γ is the oscillating mass, that for a particle trapped in the channel is the relativistic mass. Consequently the number of energy levels in the well of depth U_0 is:

$$N_i = \frac{d_p}{\hbar\sqrt{8}}\sqrt{U_0 M_\gamma}$$

The classical framework is true if $N_i \gg 1$. For heavy particles this condition is always fulfilled, while for light particles the classical approximation is valid from 10-100 MeV.

The particle motion in the channel is determined by the transverse momentum component which, if it is not large enough to overcome the potential well, keeps the particle in the channel itself; the transverse momentum component p_x is much smaller than the longitudinal one p_z if the small angle hypothesis is valid ($\theta = \frac{p_x}{p_z} \ll 1$): in other words for channeling to take place, a particle must impinge on the crystal parallel to the atomic planes. The situation is represented in a schematic way in figure 2.6.

Under these conditions the continuous potential approximation is valid and the total conserved energy of the system can be approximated as:

$$E = \sqrt{p_x^2c^2 + p_z^2c^2 + m^2c^4} + U(x) \approx \frac{p_x^2c^2}{2E_z} + U(x) + E_z \tag{2.9}$$

with $E_z = \sqrt{p_z^2c^2 + m^2c^4}$. For a motion in the potential $U(x)$, the longitudinal component is conserved, thus the transverse energy (E_T) is conserved too:

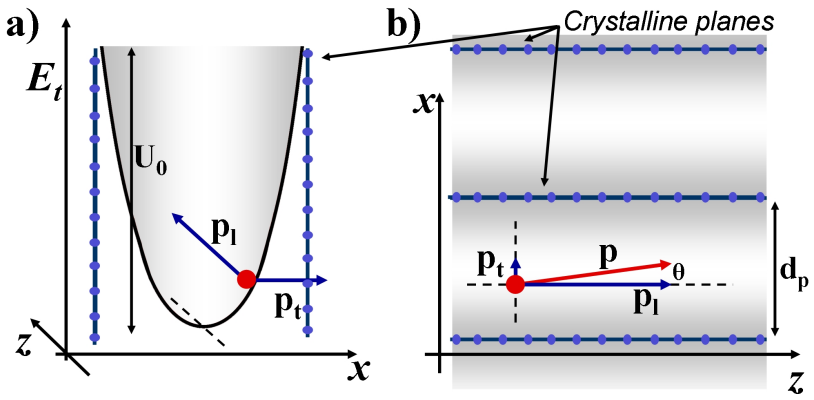

Figure 2.6: The particle motion in the channel is guaranteed by the small transverse momentum. a) A particle in the interplanar potential; b) the top view of the channel. In the schemes $p_t = p_x$ and $p_l = p_z$.

$$E_T = \frac{p_x^2 c^2}{2E_z} + U(x) = \frac{p_z^2 c^2}{2E_z}\theta^2 + U(x) = const \tag{2.10}$$

This equation defines the particle trajectory in the (x,θ) plane; the trajectories represent a set of ellipses depending on the value of E_T (figure 2.7).

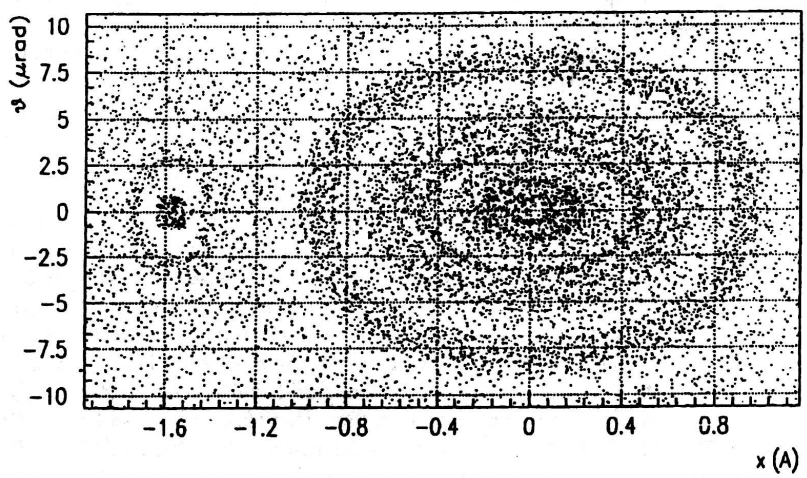

Figure 2.7: The trajectories of 450 GeV/c simulated protons in a (111) silicon plane for a straight crystal [41].

Assuming $E_z \approx E$, $p_z \approx p$ (since $\frac{p_x}{p_z} \ll 1$) and $pc^2 = vE$, the transverse energy

becomes:

$$E_T = \frac{pv}{2}\theta^2 + U(x) = \ const \tag{2.11}$$

The condition for the capture of the particle into the channeling mode is:

$$\frac{pv}{2}\theta^2 + U(x) \leq U_0$$

Assuming $x = 0$, the limiting angle of capture, or *Lindhard angle*, is:

$$\theta_L = \sqrt{\frac{2U_0}{pv}} \tag{2.12}$$

For (110) silicon, the Lindhard angle is 20 μrad at 100 GeV and becomes 7 μrad at 1 TeV. It has to be noted that the critical angle decreases as the square root of the energy while the multiple scattering as the energy of the incoming particles so the effects due to multiple scattering which (as will be shown) reduce the channeling efficiency become less important at high energy.

The scattering with the nuclei can in fact remove particles from the channeling mode; in this case the critical transverse coordinate for the channeled particle is $x_c \approx \frac{d_p}{2} - a_{TF}$. Using this assumption, the *critical channeling angle* is defined as:

$$\theta_c = \sqrt{\frac{2U_{max}}{pv}} \tag{2.13}$$

where U_{max} is the maximum value of the potential barrier. U_{max} is reached at the plane itself ($x = \frac{d_p}{2}$). However, in this position the particle could be immediately removed from the channel by the scattering with the nuclei, which means that below a minimum distance with respect to the plane, the particle is still not in channeling. This distance is a_{TF}, so the maximum transverse position reachable in channeling is x_c and the corresponding potential value $U(x_c) = U_0$.

Differentiating equation 2.10 with respect to z, the particle oscillation in the channel is described as:

$$pv\frac{d^2x}{dz^2} + U'(x) = 0 \tag{2.14}$$

Using the harmonic potential:

$$U_h(x) = U_0\left(\frac{2x}{d_p}\right)$$

the solutions of equation 2.14 are sinusoidal oscillations:

$$x = \frac{d_p}{2}\sqrt{\frac{E_T}{U_0}}\sin\left(\frac{2\pi z}{\lambda} + \phi\right) \tag{2.15}$$

$$\theta = \sqrt{\frac{2E_T}{pv}} \cos\left(\frac{2\pi z}{\lambda} + \phi\right) \tag{2.16}$$

with λ, the oscillation period, equal to:

$$\lambda = \pi d_p \sqrt{\frac{pv}{2U_0}} \tag{2.17}$$

A typical value of λ for a 450 GeV/c proton in silicon is $\sim 27\ \mu$m.

2.1.4 Dechanneling

Dechanneling occurs when a particle leaves its channeling state; this is due to the scattering with the electrons and the nuclei that form the crystal lattice: because of the scattering, θ_T (the transverse component of the angle with respect to the crystallographic planes) can increase and exceed θ_c. The consequent non-conservation of the transverse energy can be explained using the random-walk process; the variation of the transverse energy E_T can be written as:

$$\Delta E_T = pv\theta\theta_s + \frac{pv}{2}\theta_s^2 \tag{2.18}$$

with θ_s the scattering angle. The opposite process, called *volume capture*, is also possible and it will be presented in section 2.2.2. An analytical description of the process can be based on the diffusion theory ($\theta_s \ll \theta_c$, or, in other terms, the dechanneling process acts on a long distance scale with respect to the single collision); a possible alternative is represented by the introduction of the crystal imperfections using a Monte Carlo simulation.

In a given crystal, the number of channeled particles decreases exponentially:

$$N_{ch} = N_0 e^{-\frac{L}{L_D}} \tag{2.19}$$

where L is the crystal length, while L_D is the *dechanneling length* (which in practice represents the particle tendency to stay in channeling) defined as:

$$L_D = \frac{256}{9\pi^2} \frac{pv}{\ln(2m_e c^2\gamma/I) - 1} \frac{a_{TF} d_p}{Z_i r_e m_e c^2} \tag{2.20}$$

where m_e is the electron rest mass, r_e the classical electron radius, I the ionization potential (≈ 172 eV for silicon) and Z_i the charge number of the particle.

The dechanneling length has been computed considering only the dominant electron contribution, while the potential fluctuation due to the discreteness of the crystal lattice has a small influence: the particle oscillation length (λ) is 10^5 times larger than the interatomic scale (d_p). Considering the dechanneling length

(equation 2.20), two important terms have to be noted: the dependence on the energy and the dependence on the material and its orientation.

The second term, in fact, contains the linear dependence of L_D with respect to the energy, in agreement with the multiple scattering theory, and the reduction of its effects when energy increases; moreover, a very small logarithmic term is also present.

At the MeV energy range, the diffusion formalism approximation is valid since the maximum possible angular kick for a single collision $\theta_s^{max} \approx 1.4 m_e/M$ - with M the particle mass - is smaller than the channeling critical angle θ_c: at 10 MeV the single collision angle in silicon is $\theta_s^{max} \approx 0.77$ mrad to be compared to the channeling critical one, $\theta_c > 1$ mrad.

At high energy, $\theta_c \approx 10$ μrad, so the hypothesis $\theta_s \ll \theta_c$ is not valid anymore: the particle is thrown outside the channel and this event cannot be described by the diffusion formalism. In this case a characteristic length due to a single hard scattering can be computed:

$$L_{single} = \frac{4 a_{TF} d_p p v}{Z_i e^2} \tag{2.21}$$

Both the definitions are used to describe dechanneling, although the single collision dechanneling length is negligible with respect to the diffusion one ($L_D \approx 0.55$ m $\cdot$ p [TeV/c], $L_{single} \approx 10$ m $\cdot$ p [TeV/c]); thus the experimental data are usually described on the basis of the diffusion formalism. Figure 2.8 shows the analytical (figure a) and experimental (figure b) trend of L_D as a function of the energy.

The description of dechanneling is valid for positive charged particles which are channeled in the central region of the crystalline plane. Negative particles are rather channeled around the atomic planes as their potential well minimum corresponds to the nuclei positions. Thus the high electron and nuclei densities increase the scattering probability causing the dechanneling length to decrease.

2.1.5 Axial channeling

The previous sections describe the motion of a high energy particle hitting a crystal with an angle $\theta < \theta_c$ with respect to the crystallographic plane. The continuous potential hypothesis allows to describe the particle oscillation inside the channel and several other processes, such as dechanneling. This description becomes quite different if one considers the alignment with respect to the axis, and not with the planes. Figure 2.9 shows the motion of a particle, which is trapped in the so called *axial channeling*.

In the axial channeling the particle is aligned with respect to the planes which means it moves with a small angle with respect to the crystal atomic string and

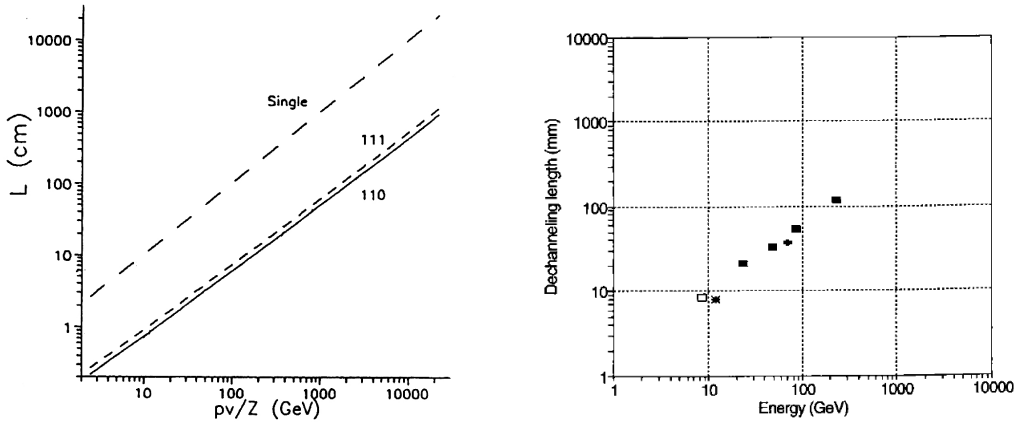

(a) (b)

Figure 2.8: a) Computed L_D trend as a function of pv for (110) Si (solid line) and (111) Si (short dashed). The single scattering is represented by the long dashed line. b) Experimental results on the measurement of the dechanneling length in silicon [41].

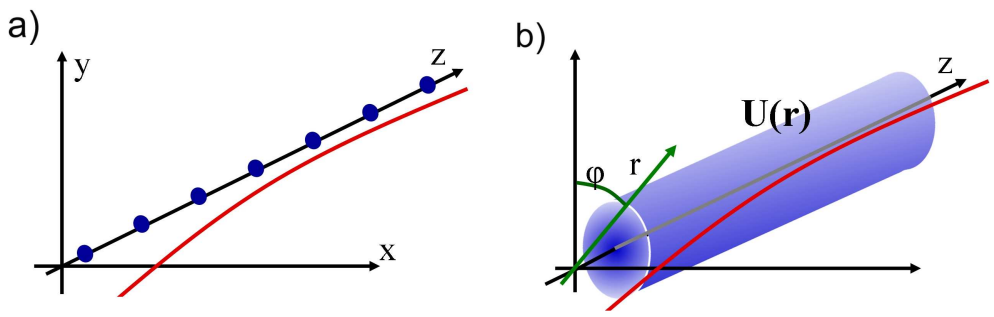

Figure 2.9: The axial channeling: a) the particle motion near the string and b) the potential with a cylindrical symmetry distribution.

feels an electric field with a cylindrical symmetry distribution (figure 2.9 b). The potential of an isolated atomic string in the Lindhard approximation (equation 2.6) is:

$$U_A(r) = \frac{Z_i Z e^2}{a_i} \ln\left(1 + \frac{3a_{TF}^2}{r^2}\right) \tag{2.22}$$

where a_i is the interatomic spacing in the string, r is the distance between the particle and the axis and a_{TF} is the Thomas-Fermi constant. The resulting transverse electric fields are shown in figure 2.10.

The particle motion in the potential is characterized by two conserved quantities: the angular momentum J and the energy in the transverse plane E_T. In

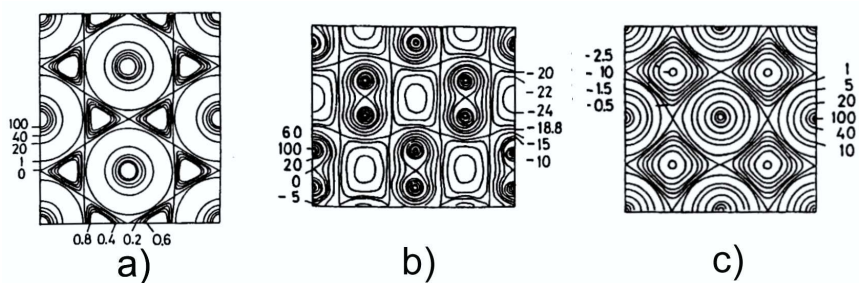

Figure 2.10: The transverse electric fields in the Molière approximation in a) (111) Si; b) (110) Si; c) (100) Si [41].

particular, the transverse energy can be divided in two components: a radial and a circular one; the angle between the particle trajectory and the crystal axis ($\theta = \sqrt{\mathrm{d}x^2 + \mathrm{d}y^2/\mathrm{d}z^2}$) can be expressed in the cylindrical coordinate system:

$$\theta = \sqrt{\left(\frac{\mathrm{d}r}{\mathrm{d}z}\right)^2 + \left(\frac{r\,\mathrm{d}\phi}{\mathrm{d}z}\right)^2} = \sqrt{\theta_r^2 + \theta_\phi^2} \tag{2.23}$$

Considering $J = p \times r = pr\theta_\phi$, the transverse energy becomes:

$$E_T = \frac{pv}{2}\theta^2 + U(r) = \frac{pv}{2}\theta_r^2 + \frac{J^2}{2M\gamma r^2} + U(r) \tag{2.24}$$

The second term represents a centrifugal term whose effect is to move the effective potential minimum aside from the channel center (r=0); so if J increases, the effective minimum moves farther from the atomic string for negative particles and nearer for positive ones.

The particle trajectory is described in the (z,r,ϕ) reference system by the relations:

$$z = \int \frac{\mathrm{d}r}{\frac{2}{pv}[E_T - U(r)] - \frac{J^2}{p^2r^2}} + const \tag{2.25}$$

$$\phi = \int \frac{\frac{J^2}{r}\mathrm{d}r}{2M\gamma[E_T - U(r)] - \frac{J^2}{r^2}} + const \tag{2.26}$$

A classical description of this motion called “rosette” has been given by Kumm et al [49], while a quantum mechanical treatment is presented in [50].

The condition for the axial channeling is that the transverse energy E_T does not overcome the maximum value of the potential well U_0. This condition can be transformed in an angular condition using the critical angle (equation 2.12). The U_0 values for the most important crystals are presented in table 2.2.

crystal	Si			Ge			W		
axes	100	110	111	100	110	111	100	110	111
U_0 (eV)	89	114	105	157	203	185	842	979	979

Table 2.2: The potential well depth of some axial channels for silicon, germanium and tungsten crystals at room temperature.

Comparing them with the potential depth of the planar case (table 2.1), the critical angle is 2-3 times greater in the axial channeling case. This favors the axial channeling with respect to the planar one, but also increases the probability for dechanneling for negative particles which is due to the nuclear scattering that can rapidly change the transverse energy, while for positive particles the interatomic axial channels are small, asymmetric and rather dependent on the axial direction.

2.2 A new era: the bent crystal

Starting from the motion of a particle confined in a channel of a straight crystal, in 1976 Tsyganov [46, 47] suggested the idea to steer a high energy particle beam using a bent crystal; the first confirmation was obtained by pioneering experiments in Fermilab and Dubna [51].

A scheme of a bent crystal is presented in figure 2.11(a): the bent channel is obtained from a straight one bending a crystal with a mechanical holder (figure 2.11(b)). For mechanical reasons, the curvature R^{-1} should be very small with respect to the crystal width w; note also that the crystal length l is independent on the radial coordinate r. As shown in figure 2.11(a), a particle (red line) is deviated from the original trajectory of an angle $\theta_b = \frac{l}{R}$.

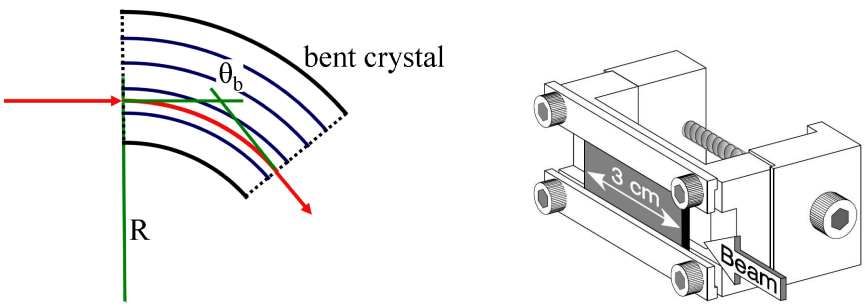

(a) (b)

Figure 2.11: a) The bent crystal scheme and b) the mechanical holder.

The curvature is described by the presence of an effective interplanar potential which takes into account the centrifugal force that reduces the interplanar potential barrier and the critical channeling angle. In the bent crystal case it is possible to define a critical curvature radius R_c (the maximum curvature wherein channeling is possible) and the quantities defined in the straight crystal case can be expressed as a function of $\frac{R_c}{R}$.

The description of a particle motion in a bent crystal requires the introduction of two phenomena: volume capture and volume reflection. Volume capture (which has already been cited in the straight crystal case) happens when misaligned particles lose transverse energy and are captured in a channel. Volume reflection (which plays a key role in crystal collimation, see chapter 1) describes the motion of a misaligned particle that is reflected by the effective centrifugal potential. These phenomena are described in sections 2.2.2 and 2.2.3, respectively.

2.2.1 Particle motion in a bent crystal

The particle motion in a bent crystal can be described with the equations illustrated for the straight crystal (section 2.1) considering the effects of a centrifugal force in the interplanar potential. In fact, the macroscopic curvature (of the order of meters) has a negligible effect on the microscopic channels: this implies that the continuous interplanar potential scenario is still valid. However a particle trapped in the channel feels a centrifugal force as well as the planar potential. This description could be schematically represented as in figure 2.12: figure a) shows the particle interaction in the channel in the laboratory frame, while figure b) shows the non inertial frame where the longitudinal direction (z) follows the channel orientation.

In the laboratory frame, a particle which impinges on the crystal with no transverse momentum ($p_t = 0$) acquires it following the curvature: the interplanar potential applies a force which modifies the particle momentum, which in turn corresponds to a particle equilibrium point different from the interplanar potential minimum. The contribution of the centrifugal force should be added in equation 2.14:

$$pv\frac{\mathrm{d}^2x}{\mathrm{d}z^2} + U'(x) + \frac{pv}{R(z)} = 0 \tag{2.27}$$

where $R(z)$ is the curvature radius as a function of the position in the channel; assuming it is independent on the position ($R(z) = R$), the crystal curvature can be approximated as an arc of circumference and the effective potential is:

$$U_{eff}(x) = U(x) + \frac{pv}{R}x \tag{2.28}$$

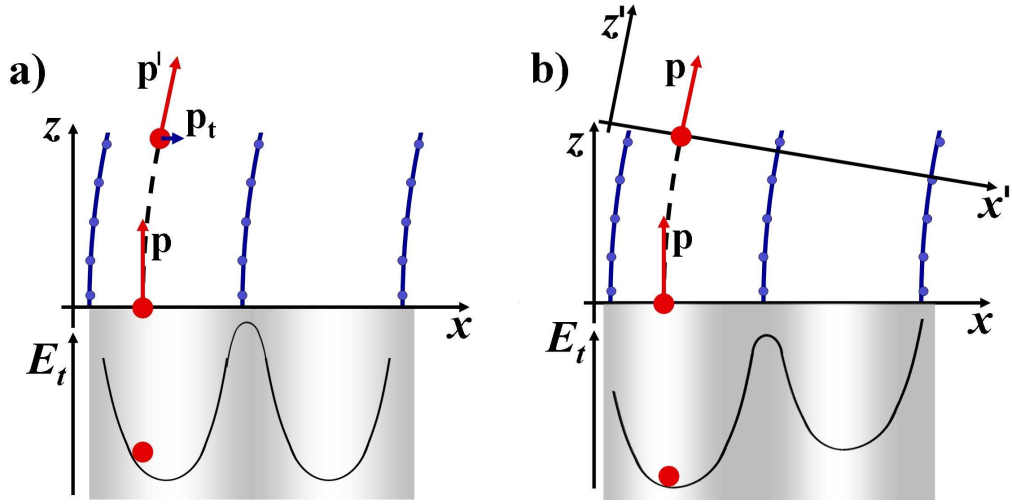

Figure 2.12: The channeling motion of a particle in a bent crystal: a) in the laboratory inertial frame in which the particle assumes an angle with respect to the planes which are curved; this implies that the equilibrium point is not in the channel center; b) in the non inertial frame which rotates with the particle: the centrifugal force appears and modifies the interplanar potential.

The particle motion expression given in section 2.1 remains valid even if the new effective potential is considered. If the curvature (R^{-1}) increases, the potential minimum is shifted towards the outer planes and the potential well depth is reduced on the outer planes, as shown in figure 2.13.

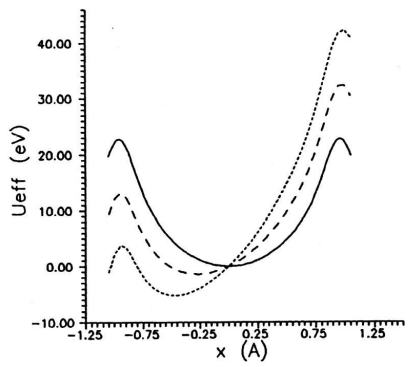

Figure 2.13: The effective interplanar potential for a (110) Si crystal in the Molière approximation for a straight channel (solid line), one with pv/R of 1 GeV/cm (dashed line) and one with 2 GeV/cm (dotted line).

The centrifugal force pushes the particles towards the atomic plane as the curvature increases, so there is a critical curvature value beyond which channeling is

not possible because the scattering probability with nuclei grows too much. This condition occurs when the centrifugal force equals the electric field produced by the atomic plane at the critical distance $x_c = d_p/2 - a_{TF}$:

$$\frac{pv}{R_c} = U'(x_c) \tag{2.29}$$

According to the Lindhard potential expression (equation 2.6), the *Tsyganov critical radius* R_c is defined as:

$$R_c = \frac{pv}{U'(x_c)} = \frac{pv}{\pi N d_p Z_i Z e^2} \tag{2.30}$$

The contribution of the single plane has been taken into account in the expression and, following the fact that x_c is close to an atomic plane, the contribution of the other plane to the potential is negligible. Since in silicon $U'(x_c) \approx 5$ GeV/cm, the critical curvature for relativistic particles of energy E is $R_c^b = \frac{E[\text{GeV}]}{5}$ cm.

Another fact can be noted in figure 2.13: the effective potential well shows a decrease of the potential barrier in the external direction with respect to the crystal bending as pv/R increases. The maximum transverse energy value for a fixed momentum particle decreases as a function of the curvature, and if U_0 is the potential well maximum in a straight crystal, the maximum transverse energy in a bent crystal assumes a new value $U_0^b < U_0$. Concerning the critical channeling angle, it is possible to define a new critical one:

$$\theta_c^b = \sqrt{\frac{2U_0^b}{pv}} < \theta_c \tag{2.31}$$

An approximated value of U_0^b as a function of the curvature can be provided considering the harmonical approximation; the effective potential becomes:

$$U_{eff}(x) = U_0\left(\frac{x}{x_c}\right)^2 + \frac{pv}{R}x \tag{2.32}$$

In a straight crystal the maximum potential U_0 positions are at $\pm x_c$; the centrifugal force just shifts the minimum position from x_c to x_{min}:

$$x_{min} = -\frac{pvx_c^2}{2RU_0} \tag{2.33}$$

so the height of the potential barrier U_0^b becomes:

$$U_0^b = U_{eff}(x_c) - U_{eff}(x_{min}) = U_0 - \frac{pv}{R}x_c + \frac{1}{2U_0}\left(\frac{pv}{R}x_c\right)^2 \tag{2.34}$$

Introducing the critical radius in the harmonic approximation $R_c^h = \frac{pvx_c}{2U_0}$, the potential barrier depth can be expressed as:

$$U_0^b = U_0\left(1 - 2\frac{R_c^h}{R} + \left(\frac{R_c^h}{R}\right)^2\right) = U_0\left(1 - \frac{R_c^h}{R}\right)^2 \tag{2.35}$$

The dependence of the critical channeling angle in a bent crystal (θ_c^b) on the critical channeling angle in a straight crystal (θ_c) and on the curvature ($1/R$) is:

$$\theta_c^b = \theta_c\left(1 - \frac{R_c^b}{R}\right) \tag{2.36}$$

According to the fact that the effective potential in a bent crystal is still harmonic, the particle trajectory has the same shape as in the straight crystal case:

$$x = -x_c\frac{R_c}{R} + x_c\sqrt{\frac{E_T}{U_0^b}}\sin\left(\frac{2\pi z}{\lambda} + \phi\right) \tag{2.37}$$

So, in a bent crystal, an oscillation of period λ occurs around a new equilibrium point $x_{min} = -x_c R_c/R$.

Because of the shift of the equilibrium point, the dechanneling probability should increase; but, as the valence electrons in Si and Ge have a roughly uniform distribution in the channel, the electron scattering probability of a channeled particle is almost insensitive to the crystal curvature for curvature radii $R \gg R_c$. This effect is anyway hidden by the greater influence on the dechanneling yield of the reduction of the maximum transverse energy. Consequently the dechanneling length, that is proportional to the maximum transverse energy, becomes:

$$L_D^b = L_D\left(1 - \frac{R_c^h}{R}\right) \tag{2.38}$$

Moreover, it is possible to recompute the dechanneling length as a function of a critical energy pv_c:

$$L_D^b = L_D\left(1 - \frac{pv}{pv_c}\right)^2 \propto pv\left(1 - \frac{pv}{pv_c}\right)^2 \tag{2.39}$$

The dechanneling length in a bent crystal is not a monotonic function of the energy but has a maximum at $pv = 1/3\ pv_c$: this value is an optimal choice to minimize the dechanneling losses in a bent crystal.

2.2.2 Volume capture (VC)

In the previous sections the description of a particle motion inside a channel was given: if the particle impinges on a channel with a small transverse momentum and the scattering effects with the planar nuclei are negligible, the particle remains trapped in the channel. However, it could happen that the multiple scattering in the channel increases the transverse momentum and the particle can overcome the potential barrier and exit the channel (the so-called dechanneling effect).

Following Lindhard's suggestions [48], a reverse mechanism could be foreseen: a particle which enters the crystal, misaligned with respect to the crystallographic plane (or, in other terms, with a high transverse momentum), can lose energy because of the multiple scattering and can be captured in a channel; this phenomenon is called *feed-in* or *volume capture*.

The dynamics of the channeled and the random (amorphous condition) particle is determined by the dechanneling and the feed-in mechanisms as shown in figure 2.14. In a straight crystal (figure 2.14(a)) a particle (red line) feels the inter-

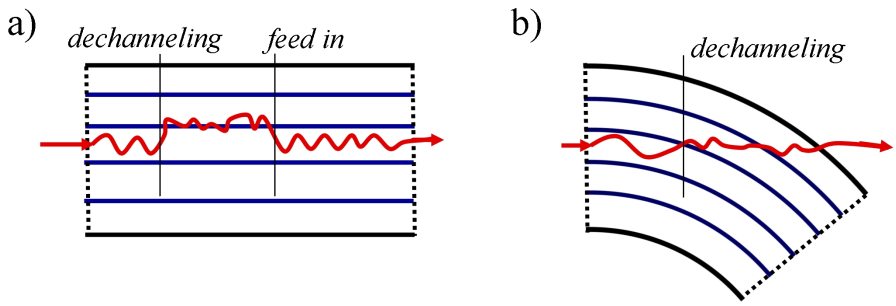

Figure 2.14: Possible particle trajectories in a straight and bent crystal. a) A particle is first dechanneled and subsequently re-channeled (or feed-in phenomenon). b) In a bent crystal, after a dechanneling event, the feed-in probability rapidly decreases as the particle is no more aligned with the channel.

planar potential in a channel until the multiple scattering increases its transverse momentum making the particle overcome the potential barrier (first horizontal line or dechanneling line). From there on, the free particle moves randomly changing its angle with respect to the channel: at a certain point (feed-in line) the particle is re-captured.

In a bent crystal (figure 2.14(b)) the situation is quite different: when a particle leaves a channel, it moves freely in the crystal, but differently from the straight case, the channel rotates its direction as the particle moves forward in the crystal itself. Defining δz the particle longitudinal displacement in a crystal, the angle

between the trajectory and the channel is

$$\theta = \frac{\delta z}{R} \tag{2.40}$$

When the particle path is greater than $R\theta_c$, the angle between the trajectory and the channel is greater than the critical channeling angle, so the particle is misaligned and cannot be channeled. Consequently, in a bent crystal, volume capture after a dechanneling process has a low probability.

Figure 2.15 is a pictorial representation of volume capture: in a bent crystal this phenomenon can occur when the particle trajectory is nearly tangent to the channel, or, in other words, when the angle between the particle and the channel is $\theta < \theta_c$.

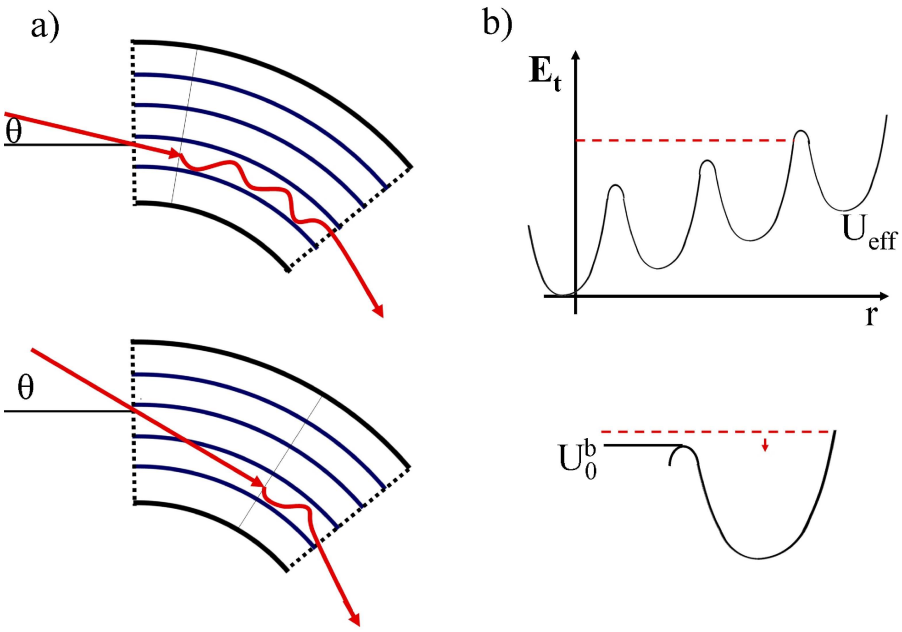

Figure 2.15: Volume capture effect. a) Two examples of volume captured particles in a bent crystal. b) Trajectory of a volume captured particle represented in the phase space (transverse energy versus radial position). In the zoom, note that the particle reaches a quasi-channeling condition.

VC occurs for impact angles larger than the critical one as long as the impact angle stays smaller than the bending one ($\theta < \theta_b$); when θ increases, the tangency condition moves along the crystal volume, as shown in the two examples in figure 2.15.

Figure 2.15(b) shows the (E_T,r) phase space: the particle transverse energy (red line) is plotted as a function of the radial coordinate, while the curve represents the effective potential (due to the interplanar potential and the centrifugal force). The transverse energy is the sum of a kinetic term and a potential one:

$$E_T = pv\theta^2 + U_{eff}(r) \tag{2.41}$$

The U_{eff} term increases as a function of the radial coordinate, so the kinetic term should decrease: since pv is constant, θ decreases. In the non inertial frame, this represents the progressive particle alignment with the channel.

At a radial coordinate r_t, the potential $U_{eff}(r_t)$ equals the transverse energy E_T, so the particle is aligned with the channel ($\theta = 0$). Note that (bottom figure) at this position the potential energy is greater than the potential barrier: the particle is not contained in the channel and it will be reflected with the same incoming angle. This phenomenon is called *volume reflection* and will be explained in section 2.2.3.

Volume capture is related to the dechanneling effect since both depend on the scattering probability. The number (N_c) of channeled particles is provided by the differential equation obtained from the exponential trend in equation 2.19:

$$\frac{\mathrm{d}N_c}{\mathrm{d}z} = -\frac{N_c}{L_D} \tag{2.42}$$

where dz is the infinitesimal longitudinal increment, while L_D is the dechanneling length. Considering the feed-in process (with N_{qc} the number of quasi-channeled particles and L_F the feed-in length, where $L_F = L_D$, due to the reversibility rule), equation 2.42 becomes:

$$\frac{\mathrm{d}N_c}{\mathrm{d}z} = -\frac{N_c}{L_D} + \frac{N_{qc}}{L_F} \tag{2.43}$$

Considering just the case when particles impinge on the crystal with an angle greater than the critical one, that is no particles are channeled, $N_c = 0$ and:

$$\frac{\mathrm{d}N_c}{\mathrm{d}z} = \frac{N_{qc}}{L_D} \tag{2.44}$$

According to the considerations made at the beginning of this section (at $\theta < \theta_c$, $\delta_z = \theta_c R$) the longitudinal increment is $\delta z \ll L_D$ and the number of captured particles is approximately:

$$\delta N_c \approx N_{qc}\frac{L_D}{\delta z} = N_{qc}\frac{L_D}{R\theta_c} \tag{2.45}$$

So the volume capture probability is:

$$P_{vc} = \frac{\delta N_c}{N_{qc}} \approx \frac{R\theta_c}{L_D} \tag{2.46}$$

Considering the trajectories reversibility in the crystal [41], a more rigorous definition contains a numerical correction factor:

$$P_{vc} = \frac{\pi}{2}\frac{R\theta_c}{L_D} \tag{2.47}$$

Finally the volume capture probability as a function of the curvature and beam energy is:

$$P_{vc} \propto \frac{R}{(pv)^{3/2}} \tag{2.48}$$

2.2.3 Volume reflection (VR)

Volume reflection could be the candidate for the last frontier of beam collimation thanks to its large efficiency and angular acceptance. VR describes the particle deviation in a single tangency point inside the crystal due to an elastic scattering with the atomic potential barrier. Discovered in a computer simulation [52], the first experimental observation is very recent [53].

Figure 2.16 shows the particle motion and effective potential in a bent crystal in a volume reflection alignment position.

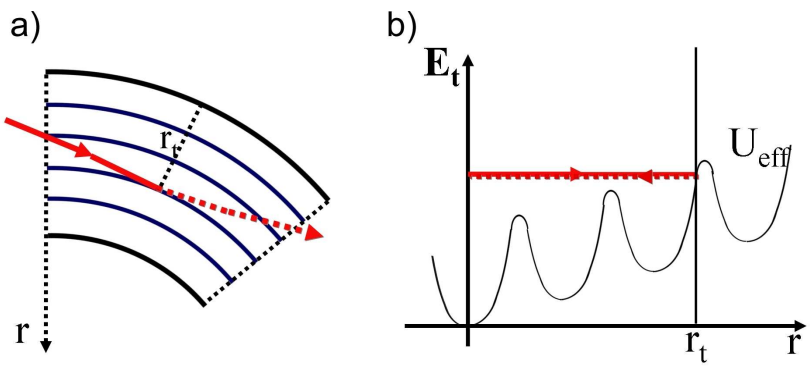

Figure 2.16: Volume reflection phenomenon. a) A charged particle in the crystal volume is reflected at the turning radial coordinate r_t. b) Phase space of the particle transverse energy as a function of the radial coordinate.

A particle which impinges on the crystal with an angle larger than the critical one (θ_c), cannot be channeled because of the high transverse momentum. In this

case the motion of the free particle can be described like the one in amorphous matter: multiple scattering causes a decrease of the angle between the particle and the crystal plane, according to the curvature (figure 2.16(a)). Considering the non inertial reference system which follows the channel direction (figure 2.16(b)), volume reflection can be described as an increase of the effective potential felt by the particle. In fact, the particle transverse energy E_T (given by the sum of a kinetic part ($pv\theta^2$), a potential one (U_{eff}) and an offset which depends on the particle entrance point) is a conserved quantity in which an increase of the effective potential should correspond to a decrease of the angle θ. At a certain point the potential U_{eff} equals the particle transverse kinetic energy, so that $\theta = 0$ meaning that the particle is tangent to the crystal planes. At this point the particle feels the potential wall increasing its transverse energy in the opposite direction: the particle has been reflected.

In order to better understand the phenomenon, it is useful to analyze the situation in the inertial frame. Let's consider as an example the case of a particle which starts and ends its motion in the center of a channel: a particle which enters the crystal overcomes the potential barrier of different channels because of its transverse energy; however along the crystal bending the barriers become more and more parallel to the particle momentum and at a certain point the barrier stops the particle motion towards the center of the crystal. At this point the barrier causes a particle motion deviation: according to the energy conservation, this means that the potential energy of the barrier $U(r_t)$ should be subtracted from the particle kinetic energy in the transverse direction. Therefore the deflection angle is:

$$\delta\theta = \sqrt{\frac{2U(r_t)}{pv}} \tag{2.49}$$

After being stopped, the particle is on the top of the barrier from where it is pushed towards the channel center: the potential energy $U(r_t)$ is converted in kinetic energy which means the particle assumes another angular kick $\delta\theta$.

The reflection is thus described in two steps: the particle is first stopped by the potential barrier and then it is accelerated in the opposite direction. The total angular kick is the sum of the partial kicks $\delta\theta$:

$$\theta_r = 2\sqrt{\frac{2U(r_t)}{pv}} \tag{2.50}$$

From figure 2.16(b) it is clear that a reflected particle has a too large transverse energy to be trapped in channeling, so the particle exits from the crystal in the direction assumed after the reflection.

According to figure 2.17(a), a better comprehension of the potential $U(r_t)$ is necessary. $U(r)$ is the crystal interplanar periodic potential whose period is the

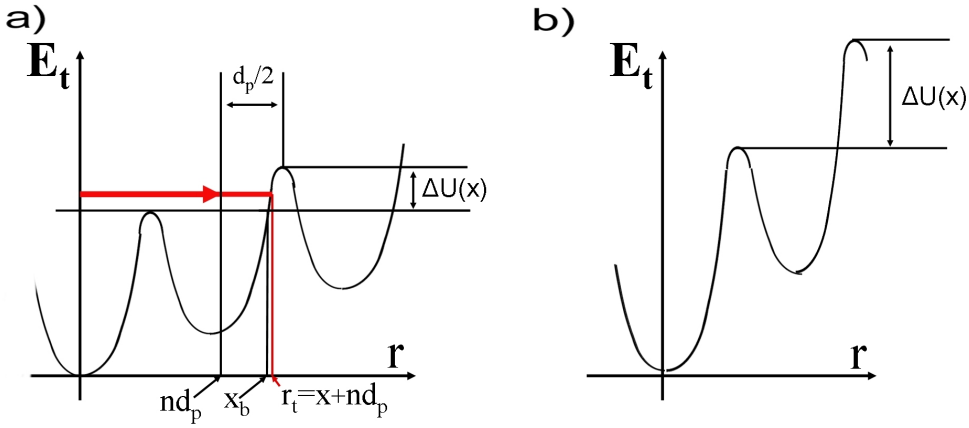

Figure 2.17: a) The effective potential at the turning point. b) An effective potential of a smaller radius with respect to the a) case: the reflecting area $\Delta U_{eff}(x)$ increases.

distance between the crystal planes (d_p): $U(r+nd_p) = U(r)$. If $r_t = nd_p + x$ (where x is defined as the distance between the reflection point and the nearest channel center), $\theta_r = 2\sqrt{\frac{2U(r_t)}{pv}}$. In case of large bending radii ($R \gg R_c$) the effective potential has a small component due to the centrifugal force (pv/R), so the x_b value (figure 2.17) will be close to $d_p/2$ so that $x \simeq d_p/2$ and the volume reflection angle can be approximated as:

$$\theta_r \simeq 2\sqrt{\frac{2U(d_p/2)}{pv}} = 2\theta_c \tag{2.51}$$

This approximation takes into account the limit $R \to \infty$ which clearly does not allow the reflection so that the maximum reachable θ_r value is just below $2\theta_c$. It is important to note that although different particles can be reflected in different turning points depending on their initial transverse energy, they will have the same reflection angle because the x value is almost fixed. In case of a crystal radius decrease, the reflection region ($x_b < x < d_p$) of the potential barrier increases (figure 2.17(b)) and the volume reflection angle being a function of x will assume a larger distribution of values. An experimental validation has been given in the 2007 beam test, as described in section 4.1.1.

Equation 2.51 describes the volume reflection angle under the following conditions:

1. $R \gg R_c$;
2. the particle enters and leaves the crystal in the center of the channel.

These conditions favor a large volume reflection angle; Monte Carlo simulations [54] and analytical calculations [55] give a more precise estimation of the volume reflection angle to be $1.5\theta_c$ rather than $2\theta_c$.

Soon after its discovery in Monte Carlo simulations, volume reflection has not been considered as an alternative to channeling for beam steering. Even if the deflection angle is almost fixed and small, if compared to the channeling one, it must nevertheless be admitted that there are several advantages in VR with respect to channeling for collimation purposes:

- the channeling angular acceptance (θ_c) is fixed which could be a problem with a beam with a large divergence ($\theta > \theta_c$). On the other hand, the volume reflection acceptance is large, making this effect less affected by the beam divergence;

- at very high energy the scaling properties favor volume reflection ($\theta_c \propto E^{-\frac{1}{2}}$) with respect to multiple scattering ($\theta_c \propto E^{-1}$) and channeling ($\theta_c \propto \frac{1}{R_c} \propto E^{-1}$);

- volume reflection is characterized by high efficiency (close to 100%).

2.3 Energy loss by heavy and light particles

This section describes the anomalous energy loss of heavy and light particles in straight and bent crystals in the channeling and volume reflection orientations with respect to amorphous materials or misaligned crystals. As far as heavy particles are concerned, the energy loss for ionization is suppressed because charged particles are confined in a region with a small electron density (section 2.3.1). The radiation emitted by light particles in channeling and volume reflection (in straight and bent crystals) is described in sections 2.3.2 and 2.3.3, respectively, and can open a new door on the application of crystals.

2.3.1 Energy loss by heavy particles

Charged particles lose energy in matter mainly because of electronic collisions. A particle motion in an amorphous material or in a misaligned crystal could be described like a number of uncorrelated collisions with the single atoms and electrons, so that the impact parameter of a collision is not influenced by the previous ones; thus the energy loss can be described by the Landau distribution [56]. Because of the equipartition rule [48], the energy loss at high energy is equally given by the hard and close collisions and the soft and distant ones.

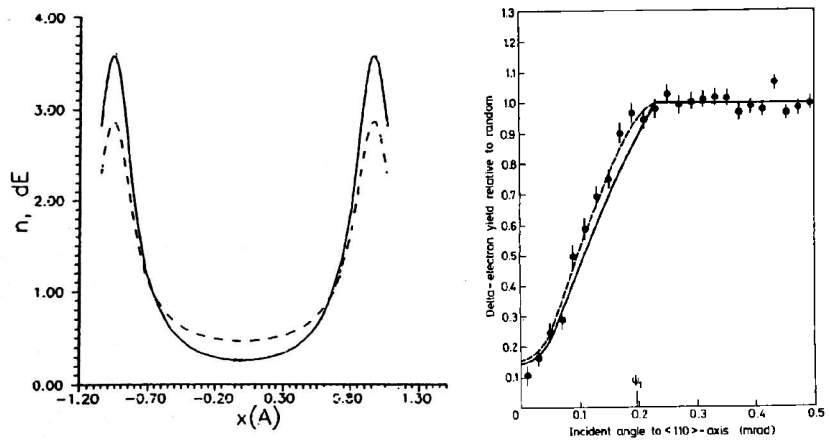

(a) (b)

Figure 2.18: a) Electron density (solid line) and the mean energy loss (dashed line) as a function of the transverse coordinate normalized to the amorphous value in a (110) silicon crystal. b) Calculated and measured δ-rays yield as a function of the incident particle angle for 11.9 GeV protons on a 0.54 mm Ge crystal [57].

In the channeling orientation, particles feel a series of correlated collisions which means a suppression of the large Rutherford scattering, nuclear reactions and close scattering with electrons, which is the most significant way to lose energy. The positive channeled particle, in fact, moves in a crystal region with a small electronic density $\rho_e(x)$ with respect to the average amorphous value: this fact is represented in figure 2.18(a) which shows the electron density in a silicon crystal as a function of the transverse coordinate; the distribution has been obtained from the second derivative of the interplanar Molière potential.

The δ-rays yield as a function of the incident angle with respect to the (110) axis for 11.9 GeV protons which impinge on a 0.54 mm Ge crystal is shown in figure 2.18(b) [57]: δ-rays are atomic electrons which are emitted in hard knock on collisions and their yield is proportional to the electron density along the particle trajectory since they are produced only in close impacts. The suppression of the close scatterings in the channel produces the decrease of both the mean value and the spread of the energy loss: the reduction depends on the average transverse position in the channel, as shown in figure 2.18(a) (dashed line).

To be more quantitative, the minimum energy loss occurs when a particle with the minimum transverse energy goes through the crystal in the channel center where the electron density is minimum. Because of the equipartition rule, the ratio between the energy loss in channeling and amorphous is:

$$\frac{\langle \Delta E \rangle_{chan}}{\langle \Delta E \rangle_{amo}} = 0.5[1+\rho_e^r(0)] = \frac{12(d_p/a_{TF})}{[(d_p/a_{TF})^2+12]^2} \simeq 0.6 \qquad (2.52)$$

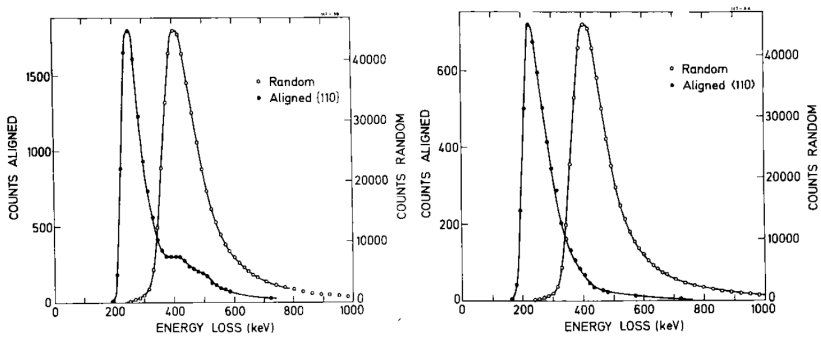

(a) (b)

Figure 2.19: Energy loss spectra of 15 GeV/c protons in a 0.74 mm germanium crystal: comparison between misaligned (random) particles and planar (a) and axial (b) channeled ones.

where the second term represents the contribution of the distant collisions (which does not change in channeling) and of the close ones which scales down with the electron density; $\rho_e^r(0)$ gives the electron density in the center of the channel. The numerical value has been computed taking into account Lindhard's approximation (equation 2.6) for (110) and (111) silicon planes.

The energy loss in the crystal can be used to study the crystal properties [57] or to tag the channeled particle, greatly simplifying the channeling measurements especially when the efficiency is low (as it happens for a beam divergence larger than the critical channeling angle) and the channeled particles are difficult to identify. To perform the measurements, the crystal is doped like a diode, so the energy deposited in the depleted crystal zone can be collected.

The energy loss spectra in a 0.74 mm germanium crystal for 15 GeV/c protons is shown in figure 2.19: the amorphous condition (random) is compared to the planar (a) and axial (b) channeling ones. The most probable value is reduced (of a factor two) and the spread of the distribution is smaller. The high energy tail in the planar case corresponds to particles with a transverse energy close to the critical value.

2.3.2 Channeling radiation in straight and bent crystals

The radiation emitted in bent crystals by positrons and electrons is still an open field because of the stringent requirements on the beam and the experimental setup. However, in literature, it is possible to find a detailed theoretical description of such an emission, distinguishing the spectra produced in straight or bent crystals.

2.3.2.1 Radiation in straight crystals

As for the amorphous matter, the radiation emitted by electrons and positrons in misaligned crystals is described by incoherent bremsstrahlung. In aligned crystals, instead, the radiation is the result of two contributions: the coherent bremsstrahlung and the channeling radiation; a strong increase of radiation due to the coherent emission takes place.

A particle which impinges on a crystal feels the crystalline structure, producing a coherent emission of radiation which gives a peaked structure to the coherent bremsstrahlung [58]. The peak energies depend on the crystal geometry and on the incident angle with respect to the crystallographic planes; the shape is equivalent for positrons and electrons. The coherent bremsstrahlung happens when particles are not in channeling, or, in other words, when the particle trajectory angle is small but anyway larger than the critical channeling angle. If the angle between the incoming particle trajectory and the crystallographic planes is smaller than the critical channeling one (θ_c), particles are trapped in the channels, producing coherent radiation which is called *channeling radiation*.

The channeling radiation depends on the interplanar potential form: positrons and electrons feel a different potential, producing different channeling radiation spectra. As far as positrons are concerned, they oscillate in a nearly harmonic potential with a wavelength (according to equation 2.37):

$$\lambda = \pi d_p \sqrt{\frac{pv}{2U_0}} \tag{2.53}$$

The corresponding angular frequency is:

$$\omega_0 = 2\pi\frac{\nu}{\lambda} = \frac{2}{d_p}\sqrt{\frac{2U_0}{m\gamma}} \tag{2.54}$$

where the relativistic relation $pc^2 = \nu E$ is considered. The intensity of the radiation emitted by a channeled positron is very high at this frequency (and in the superior harmonics) apart from the Doppler effect:

$$\omega_\gamma = n\frac{\omega_0}{1-\beta\cos\theta} \tag{2.55}$$

The resulting peak structured spectrum is shown in figure 2.20(a), where the contributions of the first two harmonics are present.

The electrons move in a strongly non-harmonic potential and the oscillation frequency becomes a function of the transverse energy. This generates the broad spectrum shown in figure 2.20(b). The different behavior for positive and negative particles is a peculiarity of the channeling radiation with respect to the bremsstrahlung one (both coherent ad incoherent).

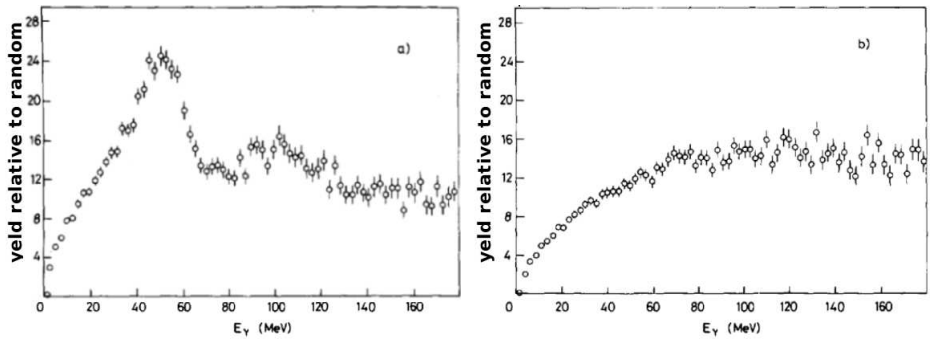

(a) (b)

Figure 2.20: Radiation emitted by 10 GeV/c a) positron and b) electron beams which impinge on a (110) 0.1 mm thick silicon crystal. In the positron case, the peak structure relative to the first and second harmonics is evident. In the electron case, instead, the spectrum shows an increase with respect to the bremsstrahlung one (as for the positron case), but no peaks are present [59].

2.3.2.2 Radiation by channeled particles in bent crystals

A relativistic positron or electron in bent crystals in the channeling orientation moves along an arc of circumference (following the channels), simultaneously performing radial oscillations in the channel field [60], as shown in figure 2.21.

The radiation emitted by light leptons in a bent crystal can be described as an undulator one if the radiation formation length (l_{coh}) is greater than the spatial oscillation period in the channel (λ). l_{coh} is defined as:

$$l_{coh} = R\gamma^{-1}$$

where R is the radius of the circumference of the crystallographic bent channel and γ is the Lorentz factor (which will be considered of the order of 10^4). This is, in practice, equal to the channeling radiation in straight crystals described in the previous section. In case of $l_{coh} \ll \lambda$, the radiation can be described as a quasi-synchrotron one.

The instantaneous radiation intensity $I(x)$ can be quantified starting from the following equation [61]:

$$I(x) = -\frac{\mathrm{d}E}{\mathrm{d}t}(x) = \frac{2e^2}{3m^2c^3}\gamma^2|\nabla U(x)|^2 \tag{2.56}$$

where $\frac{\mathrm{d}E}{\mathrm{d}t}(x)$ is the radiative energy loss rate, e and m are the charge and rest mass of the electron/positron, c is the speed of light. The effective potential felt by the particles is given by two contributions:

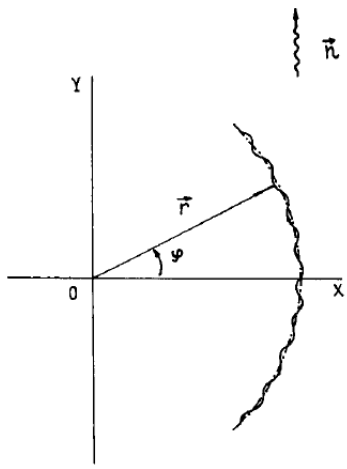

Figure 2.21: Schematic view of a channeled particle motion in a bent crystal [60].

- the average channel potential which is considered harmonic: $U(x) = U_0(x/l)^2$;
- the centrifugal force (due to the bending) $F_c = pv/R$, where p is the particle momentum and v its velocity.

The effective potential becomes:

$$U_{eff}(x,R) = U_0[(x - x_{min})/l]^2 \tag{2.57}$$

where $x_{min} = (pv/2U_0)(l^2/R)$ is the coordinate of the minimum potential position (see equation 2.33). Averaging over the crystal thickness and the initial particle condition and integrating, the intensity can be expressed as:

$$I(R) = \frac{2e^2}{3m^2c^3}\gamma^2\left(\frac{2U_0}{l^2}\right)^2\left[\frac{l^2}{6} + \frac{x_{min}^2 - 2x_{min}l}{6} + x_{min}^2\right] = I_{st} + I_a(R) + I_s(R) \tag{2.58}$$

where I_{st} describes the intensity for the straight crystal case, while I_a and I_s describe the changes in the radiation intensity due to the crystal curvature and the particle motion inside the crystal itself. In particular

$$I_s(R) = \frac{2}{3}\frac{e^2c}{R^2}\beta^4\gamma^4 \tag{2.59}$$

is the synchrotron contribution, which increases as R^{-2}.

Figure 2.22 shows the radiation intensity spectra produced in (110) silicon crystals with $\gamma = 10^4$ positrons. Curve 1 shows the radiation intensity in a straight

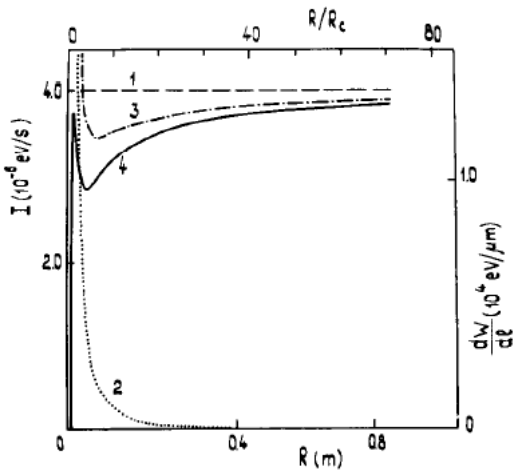

Figure 2.22: The intensity of radiation emitted by relativistic positrons ($\gamma = 10^4$) in bent crystals as a function of the crystal curvature: curve 1 refers to the radiation emitted in a straight crystal, curve 2 describes the synchrotron contribution, curve 3 is the intensity spectrum for a bent crystal and curve 4 takes into account the quasi-channeled particle contribution [60].

crystal (I_{st}), curve 2 refers to the synchrotron term (I_s). Increasing the crystal curvature the radiation emitted in a bent crystal (curve 3) decreases at the beginning, but then it increases because of the synchrotron radiation; the minimum position corresponds to $R = 7R_c$ (critical radius $R_c = \dfrac{pv}{2U_0}l$).

However another contribution should be taken into account: the quasi- channeled particles. These particles, moving in an average potential and crossing atomic planes, contribute to radiation. The efficiency of particles which are captured in the channeling regime is $P_c(R) = 1 - x_{min}(R)/l$: the result is a more rapid decrease of radiation intensity with an increasing bending radius. The radiation intensity, in fact, depends on the angle θ between the incoming particle trajectory and the atomic planes. In straight crystals, if $\theta \leq \theta_{ch}$, $I_{ch} \approx 3I_{st}$, otherwise $I_{ch} \approx 2I_{st}$. In bent crystals, instead, θ changes during the motion, so the intensity is maximum at the turning point and it becomes equal to $I_{ch} \approx 3I_{st}$.

As far as the radiation energy spectrum is concerned, it can be explained considering the expression for the forward direction (the direction tangent to the crystal middle point) and then integrating the expression on the solid angle. In general the spectral-angular distribution can be expressed as [62]:

$$\frac{\mathrm{d}^2 W}{\mathrm{d}\hbar\omega\Omega} = \frac{\alpha}{4\pi^2}|A_\omega|^2 \tag{2.60}$$

where $\alpha = 1/137$, n is the unit vector in the radiation direction (figure 2.21) and

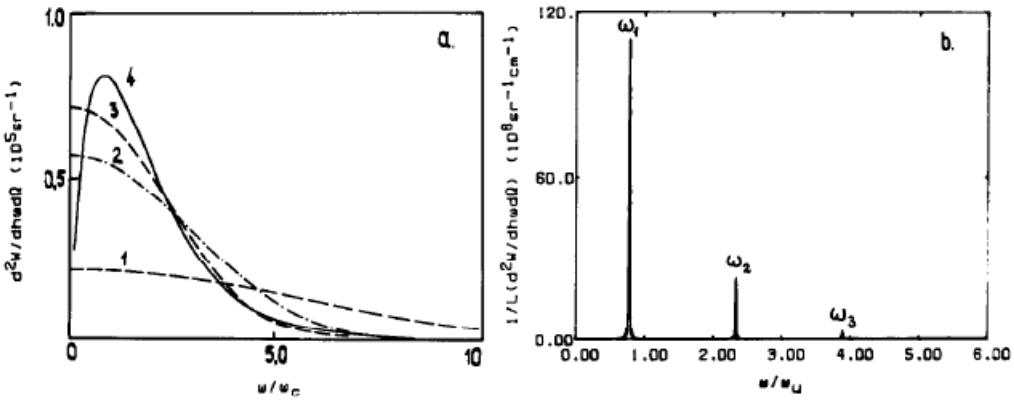

Figure 2.23: a) Radiation spectra in the forward direction of a relativistic positron ($\gamma = 10^4$) moving in a bent channel ($R = 10.8$ cm) of length L. The different curves refer to different L values: 1λ, 2λ, 4λ, 24λ. b) Radiation emitted by positrons in a (110) straight silicon crystal of length $L = 32\lambda$ with an oscillation amplitude $x_0 = 0.8L$ [60].

A_ω is the vector proportional to a Fourier-component of the electrical field intensity. According to figure 2.21, in the forward case this quantity can be expressed as [60]:

$$A_\omega = \beta \int_{\phi-\Delta s}^{\phi+\Delta s} \frac{\cos s - \beta}{(1-\beta\cos s)^2} \times \exp\left\{ i\frac{\omega}{\omega_0}[s - \beta \sin s] \right\} ds \tag{2.61}$$

where $\omega_0 = (c/l)(2U_0/E)^{1/2}$, $\Delta s = \omega_0 \Delta t$ and $\Delta t = L/2c\langle\beta\rangle$, with L the crystal length and $\langle\beta\rangle$ the mean longitudinal velocity. Two cases can be considered:

- radiation emitted by a particle in a bent channel without a transverse oscillation (the oscillation amplitude $x_0 = 0$);
- radiation emitted by a particle in a straight channel.

Figure 2.23(a) shows the radiation spectra emitted by $\gamma = 10^4$ positrons in a bent crystal without transverse oscillation ($x_0 = 0$) with a radius $R = 10.8$ cm and different crystal lengths. The radius value has been chosen one order of magnitude greater than the critical one. The curves in the figure correspond to different lengths: 1λ, 2λ, 4λ, 24λ; increasing the arc length, the energy emitted in the soft frequencies first increases and then decreases. The quasi-synchrotron radiation spectrum occurs when $L \gg l_{coh}$.

Figure 2.23(b) shows the spectrum emitted by positrons in a straight crystal: as said in the previous section, it can be described as a quasi-undulator, considering the higher harmonics.

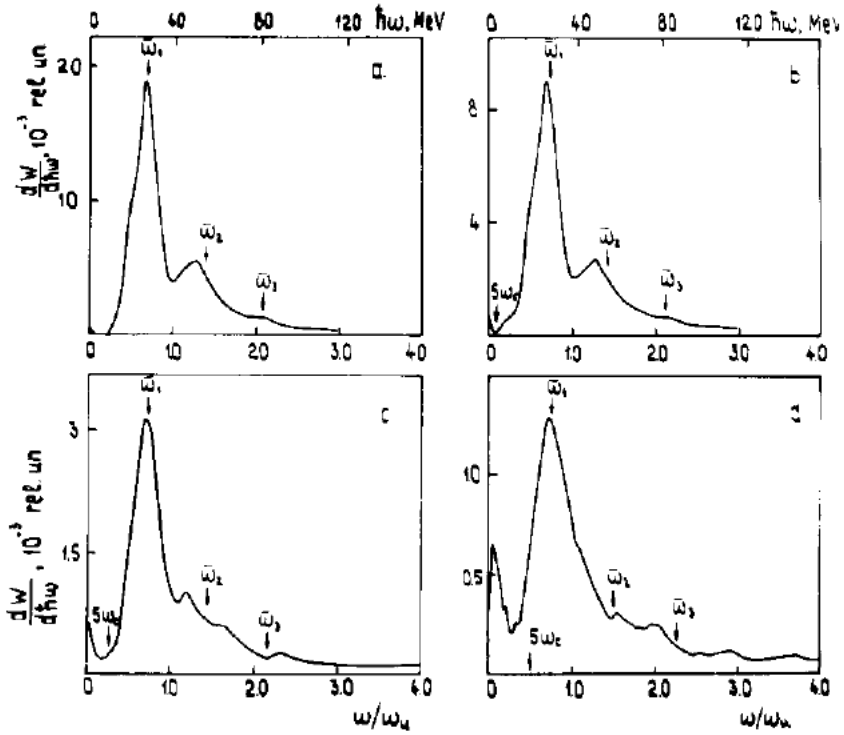

Figure 2.24: Integral radiation spectrum (integrated on a solid angle $\Delta\Omega$) for positrons channeled along the (110) planes in a bent silicon crystal. The positron beam impinges on the crystal with a null divergence. The plots correspond to: a) $R = 76.38$ cm, $\omega_u/\omega_c = 100$, $l_{coh}/\lambda \gtrsim 11$; b) $R = 38.19$ cm, $\omega_u/\omega_c = 50$, $l_{coh}/\lambda \gtrsim 5$; c) $R = 15.28$ cm, $\omega_u/\omega_c = 20$, $l_{coh}/\lambda \gtrsim 2$; d) $R = 7.64$ cm, $\omega_u/\omega_c = 10$, $l_{coh}/\lambda \gtrsim 1$ [60].

Integrating on the whole solid angle, it is possible to evaluate the integral radiation spectrum for relativistic positrons ($\gamma = 10^4$).

Figure 2.24 shows the integrated radiation spectra of positrons (with a null incoming divergence) which impinge on a (110) silicon bent crystal, under different conditions. The characteristics of the forward spectra are clearly evident in the integral ones. For small crystal radii (figures 2.24(a) and (b)), the maxima correspond to the different harmonics produced in straight crystals ($\omega_u = 2\gamma^2\omega_0$). The odd harmonics positions are determined by the oscillation in the forward direction of the positron with an oscillation amplitude $\langle\omega_k\rangle = \omega_k(\theta = 0, x_0 = 1 - x_{min})$. On the other hand, the even harmonics are shifted from $\langle\omega_k\rangle$ to the smaller frequencies.

Increasing the crystal bending radius, the radiation yield decreases at the frequencies that correspond to the radiation harmonics in a straight crystal (fig-

ures 2.24(c) and (d)).

2.3.3 Radiation emitted in volume reflection

The study of the radiation emitted in the volume reflection orientation is very up-to-date: the first prediction (presented in September 2007 [63]) has been confirmed by the experimental results which are shown in this thesis work (see chapter 4).

The theoretical explanation of this process is based on the analytical description of volume reflection [52] and on the equations derived with the quasi-classical operator method [64], where the probabilities of QED processes may be expressed by classical trajectories of charged particles in electric fields.

In general, the radiation emitted by electrons and positrons in volume reflection is different from the motion in a straight crystal because there is an aperiodicity of oscillations and the deflection of particles is of the same order of magnitude of the channeling critical angle.

It is possible to describe the radiation emitted by light leptons in the volume reflection regime with the ρ parameter [64]:

$$\rho = 2\gamma^2 \langle v_t^2 - v_m^2 \rangle / c^2$$

where $\langle v_t^2 - v_m^2 \rangle$ is the squared mean deviation of the transverse velocity from its mean value v_m.

Two important cases have to be considered:

- $\rho \ll 1$: the radiation intensity is the result of the interference on a large part of the particle trajectory and depends on the peculiarities of the particle motion;

- $\rho \gg 1$: the particle radiates during a small part of the trajectory (its motion direction does not change on the angle $1/\gamma$) and the contributions from far parts can be neglected.

The case $\rho \sim 1$ is an intermediate one.

In straight crystals, the first case ($\rho \ll 1$) takes place when θ is $\gg \theta_c$, and the coherent bremsstrahlung occurs. The opposite case ($\rho \gg 1$) corresponds to the synchrotron-like radiation and takes place when $\theta \ll \theta_b$, where $\theta_b = U/mc^2$ (m is the particle mass and U is the planar potential barrier). In case of a thin crystal, a particle conserves the radiation type during its motion.

In a bent crystal, the planar angle θ changes during the particle motion; it corresponds to a change of the radiation type during the motion itself. In particular, in the volume reflection orientation, far from the reflection point, $\rho \ll 1$ and the

radiation is due to coherent bremsstrahlung. Approaching the reflection point, the ρ parameter increases: if the bending radius is significantly greater than the channeling critical one [46, 47], the mean volume reflection angle is $\theta_{vr} \approx \sqrt{2}\theta_{ch}$ for positrons and $\theta_{vr} \approx \theta_{ch}$ for electrons [65]. Near the reflection point it is possible to estimate $\rho = \gamma\theta_b$ for positrons and $\rho = 0.5\gamma\theta_b$ for electrons. At $\rho = 1$, for the (110) and (111) planes of a silicon crystal, the particle energy E corresponds to 12 GeV for positrons and 24 GeV for electrons. Figure 2.25 shows the transverse particle velocity in the area near the reflection point as a function of time: a particle performs an aperiodic oscillation in the transverse plane and the amplitude of the oscillations increases as the particle approaches the reflection point.

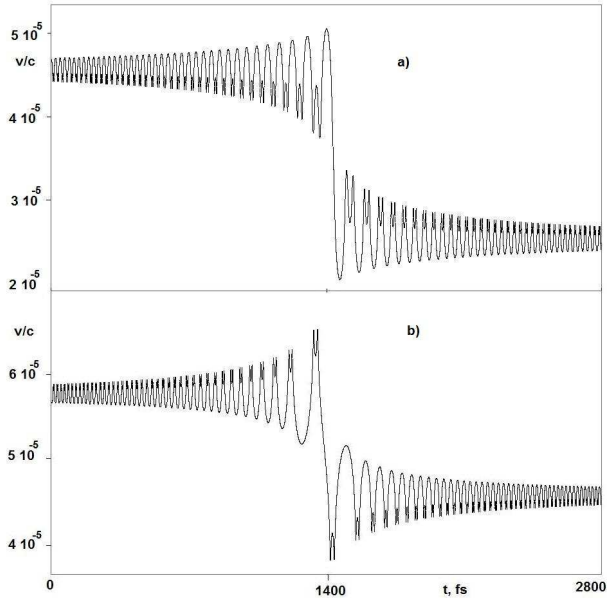

Figure 2.25: The relative transverse velocities (v_t/c) of 180 GeV/c positrons (a) and electrons (b) at volume reflection in a (111) silicon plane (0.84 mm thick) as a function of time (in fs).

An estimation of the emitted γ energy range is given by the equations [64]:

$$\omega = \frac{2\gamma^2\omega_0}{1+\rho/2} \tag{2.62}$$

$$E_{\gamma,max} = \frac{\hbar\omega E}{E+\hbar\omega} \tag{2.63}$$

where $\omega_0 = 2\pi/T$ and T is the period of one oscillation set. These equations in practice define the maximum γ energy (the minimum energy is close to zero). These relations are written for the radiation first harmonic and for the case of an

infinite periodic motion and are in good agreement with calculations (in fact when $\rho \lesssim 1$ the first harmonic gives the main contribution to radiation).

Figure 2.26(a) shows the energy range of the emitted γ-quanta calculated according to equations (2.62-2.63): the vertical lines correspond to the energy computed with the ρ parameter for every oscillation.

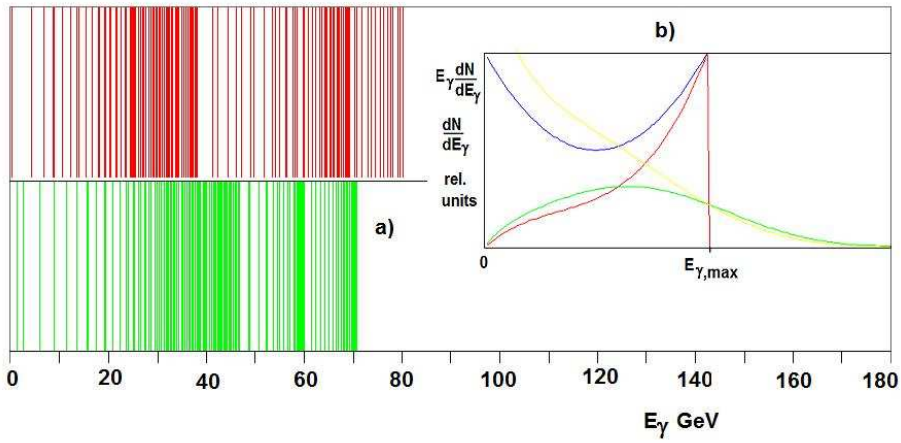

Figure 2.26: The maximum energies of the γ-quanta (a) calculated according to equations (2.62-2.63) from the corresponding frequencies of the motion. Red and green lines correspond to 180 GeV/c positrons and electrons, respectively. The shapes (b) of the γ-quantum spectra and energy losses in periodic structures: the yellow and green curves are the γ spectrum and distribution of energy losses for a structure with one period. The blue and red curves are the same values but for an infinite periodic structure.

Figure 2.26(b) shows the behavior of the intensity and the number of γs as a function of the energy for a simple harmonic motion in a periodic structure (like an undulator) when this structure has only one oscillation and an infinite number of periods. In the one period structure the energy could overcome the maximum energy $E_{\gamma,max}$; it is anyway possible to use equations (2.62-2.63) to estimate the radiation spectra because the number of emitted γ-quanta rapidly decreases above $E_{\gamma,max}$. The greater is $E_{\gamma,max}$, the smaller is the probability of radiation of the first harmonic as a whole. From the theory of coherent bremsstrahlung it is possible to evaluate the relative variation of radiation intensity as a function of $x = E_\gamma/E$ via the relation $I_{max} = [1+(1+x)^2])(1-x)/x$: in the considered case, $x = E_{\gamma,max}/E$. This behavior is due to an increase of the longitudinal recoil momentum and hence a decrease of the process formation length.

The radiation energy spectra is shown in figure 2.27: for 200 GeV/c positrons (electrons), a peak is expected at about 40 (30) GeV; moreover the radiation emit-

ted in volume reflection is higher than the amorphous contribution (curve 3).

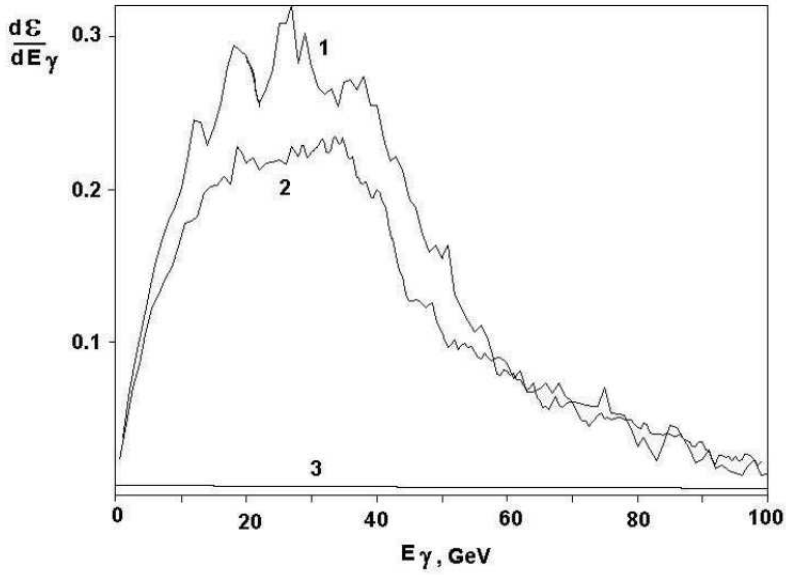

Figure 2.27: Differential radiation energy spectrum for (1) positrons and (2) electrons in a 0.45 cm silicon crystal with respect to the amorphous contribution (3) [63].

The semiqualitative study used here is valid for electron (positron) beams (and silicon crystals) in the range of hundreds of GeV: at energies > 1 TeV the synchrotron-like character of the radiation in a thin crystal should become the dominant one.

It must be underlined that these calculations are subject to some limitations:

- the particle multiple scattering has not been taken into account;
- some particles may be captured in the channeling regime (volume capture): the motion (and therefore the radiation emitted) changes;
- the radiation of two or more γ-quanta has not been taken into account.

Chapter 3

The 2007 experimental setup

As illustrated in chapter 2, the first studies on a collimation system based on a bent crystal were made in the '70s at Fermilab [46, 47]. Until 2006, the basic detector system to understand the crystal behavior consisted in integration detectors (emulsion films) and beam monitors (beam loss monitors, ionization chambers). For the first time in 2006 the H8RD22 collaboration has used a real time system based on microstrip silicon detectors for high precision studies of the particles steered by different kinds of crystals (strip and quasimosaic). This system was able to provide a precise measurement of the outgoing angle ($\sim$ 10 μrad), selecting the particles which hit the crystal [66].

In 2007 the system has been improved with the use of very high precision silicon detectors, providing a 0.5 μrad angular resolution and able to acquire data at $\sim$ 3 kHz.

This chapter presents a description of the setups used in 2007 on the CERN SPS H8 line: the silicon detectors, the crystals, the goniometer system, the sampling calorimeter and the trigger system and their performances with different beams. The last part of this chapter describes the basic procedure for crystal measurements: the crystal is pre-aligned with respect to the beam with a laser system; a lateral scan is performed to position the crystal on the beam; the behavior of the crystal as a function of the goniometer angle is evaluated by an angular scan.

The procedure of raw data stripping is described in appendix A.

3.1 The CERN SPS H8 beamline

The beam tests have been performed on the H8 line at the CERN Super Proton Synchrotron (SPS). The SPS (figure 3.1) is a 7 km circumference circular accelerator which provides particles with a momentum up to 450 GeV/c to external lines (North Area), LHC, COMPASS and CNGS.

Figure 3.1: The CERN accelerator complex.

The Super Proton Synchrotron is one of the actors of the history of particle physics: as an example it is possible to cite the UA1-UA2 experiments in 1983 when the SPS was a proton-antiproton collider (Sp$\overline{\text{p}}$S) allowing Carlo Rubbia and Simon van der Meer to win the Nobel Prize thanks to their pioneering discovery of the gauge bosons $W^{\pm}$ and Z^0 [67].

The SPS is formed by 1317 magnets of which 744 are bending magnets to curve particles along the ring. Radiofrequency cavities can accelerate protons, antiprotons, oxygen and sulfur nuclei, electrons and positrons up to 450 GeV/c: the particles are first accelerated by a LINAC (up to 50 MeV) and the Proton Synchrotron (PS), up to 26 GeV. In 2007 the beam was extracted in the North Area (where H8 is sited, figure 3.2) in spills of 4.8 s every 16.8 s (supercycle duration).

Figure 3.2: The North Area complex. The H8 line is the first from the bottom.

Particle tracking systems, scintillators, beam loss monitors and calorimeters are used to understand the beam behavior along the line.

3.2 The 2007 beam tests

In 2007 the H8RD22 collaboration has tested several crystals in three different beam tests:

- May 25th - June 10th (“May beam test”)
- September 23rd - October 14th (“October beam test”)
- October 29th - November 11th (”November beam test”)

The May and November beam tests have been characterized by a very high precision, fail proof, compact and simple setup to evaluate the behavior of several crystals with ultra relativistic 400 GeV/c protons; figure 3.3 shows the experimental layout.

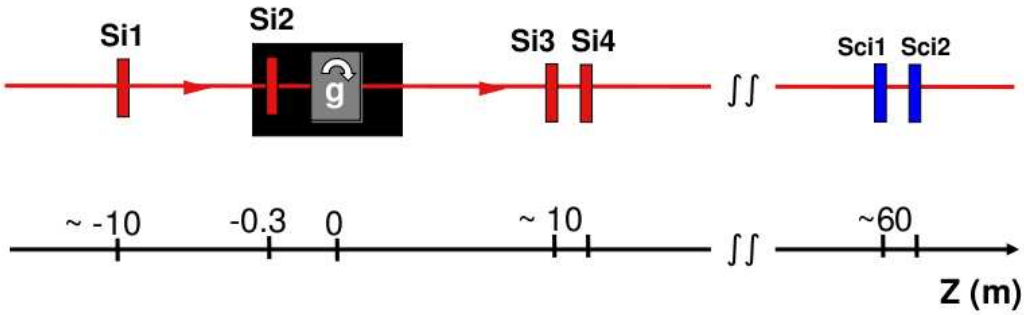

Figure 3.3: The May and November setup: a set of 50 μm readout pitch double side microstrip silicon telescopes (SiX), the high precision goniometer (g) and a pair of plastic scintillators (SciX) which provided the trigger signal. In May, the scintillators have been positioned at 60 m from the crystal because of space problems; in November, a rearrangement of the H8 line has allowed to put the scintillators close to the last detectors.

The incoming particle trajectory is computed using the spatial information of two 50 μm readout pitch double side microstrip silicon telescopes Si1-Si2 (section 3.2.1), while the outgoing one is based on the Si2 - Si3 or Si3 - Si4 pair (Si4 is used as a backup of Si3 only in case of a missing hit on Si3 due to a noisy or dead channel). In the horizontal direction the spatial resolution of the silicon telescope is $\sim$ 5 μm, so the angular resolution is about:

$$\sigma_{ang} \cong \frac{5\ \mu\text{m}}{10\text{m}} = 0.5\ \mu\text{rad} \tag{3.1}$$

Different types of crystals have been tested (section 3.3): each crystal has been positioned on a high precision goniometer ($\sim$ 1.5 μrad angular resolution) which provides an angular rotation, two independent linear movements and a cradle for the studies on the axial channeling (section 3.4).

A pair of scintillators (positioned in the downstream area in May and close to the last detectors in November) provided the trigger signal for the DAQ system. The goals of the May-November beam tests were:

- the study of the behavior of the volume reflection phenomenon as a function of the primary crystal curvature;
- the study of the multicrystals. Quasimosaic crystals have been aligned for these studies using remote controls (remote screwdrivers and piezoelectric motors);
- the study of the axial channeling;
- the study of crystals made of different materials (germanium and diamond).

In the October beam test, the crystals were tested with ultra relativistic light leptons (both electrons and positrons) of 180 GeV/c of momentum: figure 3.4 shows the experimental setup.

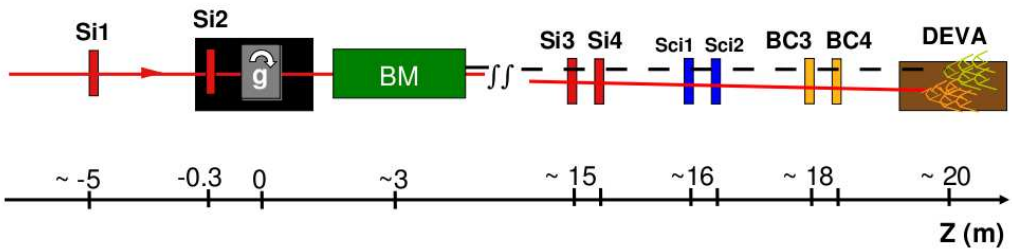

Figure 3.4: The October setup: the microstrip silicon telescope (SiX), the high precision goniometer (g), a bending magnet (BM), a 9.5×9.5 cm^2 silicon beam chamber (BC1,BC2) system, a pair of scintillators (SciX) and the electromagnetic calorimeter (DEVA). The black dashed line corresponds to gammas produced in crystals, while the red line shows the charged particle trajectories after the bending magnet.

The goals of the October beam test were:

1. the study of the crystal behavior as a collimator: the channeling and the volume reflection orientation have been measured; moreover the volume reflection regime has been observed for the first time with negative particles;

2. the evaluation of the radiation emitted by light leptons in the amorphous and volume reflection cases.

The first goal required the same procedure followed in the other tests: the incoming particles (which could be light particles, muons or light hadrons) are detected by the silicon telescopes (Si1-Si2) and hit the crystal positioned on a high precision goniometer. The outgoing trajectory is computed from the information of Si2 and Si3 or Si4.

For the VR studies, the trigger signal has been provided by a pair of scintillators (SciX); for the radiation data taking a sampling calorimeter (DEVA) has been implemented in the trigger system using the signals from the last two tiles with high threshold.

The radiation emitted by light leptons in the volume reflection orientation, as explained in section 2.3, has been measured using a spectrometer method: a bending magnet steers the charged particles (red line in figure 3.4) depending on their momentum and the silicon detectors reconstruct the outgoing trajectory. To increase the sensitive area in these measurements, a set of 9.5×9.5 cm^2 silicon beam chambers (BC1,BC2) has been used.

3.2.1 The silicon detectors

In the 2007 beam tests two different types of silicon detectors have been used: a set of four *telescopes* and a set of two *AGILE beam chambers*.

Each *telescope* consists of a double side high resistivity 300 μm thick 1.92×1.92 cm^2 microstrip silicon detector (figure 3.5(a)) with a very high spatial resolution [68]. The detector p-side (or junction side), which measures the horizontal direction, has a p$^+$ strip every 25 μm while the readout pitch is 50 μm; in practice a one floating strip scheme is implemented. The vertical side (n-side, or ohmic side) has a n$^+$ implantation every 50 μm, perpendicular with respect to the p-side strips. The modules have been biased with 36 V and the bias current was measured to be 17 nA per module.

Each silicon side is readout by three VA2[1] 128 channel ASICs (Gamma Medica-IDEAS, Norway), built with a 1.2 μm N-well CMOS technology. The VA2 ASIC architecture is shown in figure 3.6. Each ASIC channel consists of:

- a low-noise/low power charge sensitive preamplifier;
- a CR-RC shaper;
- a sample & hold circuit.

[1] http://www.ideas.no/products/ASICs/pdf/VA2S2.pdf

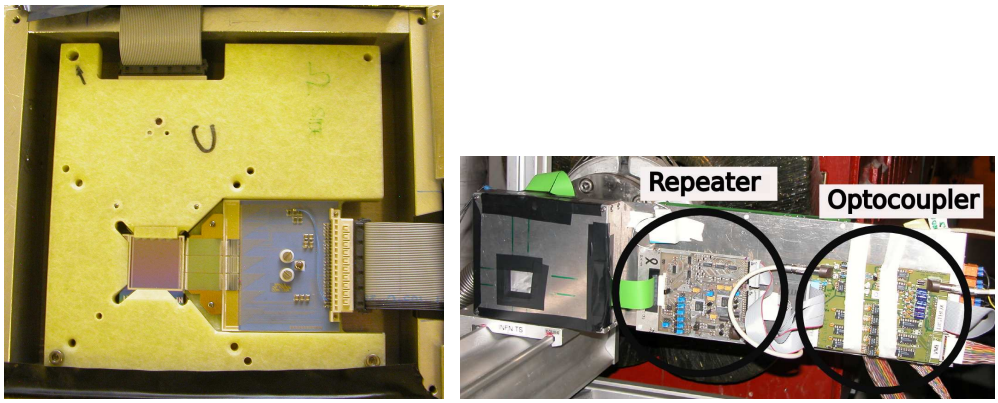

(a) (b)

Figure 3.5: a) The telescope module: the strips are readout by the VA2 ASICs, which amplify and shape the signals. b) The telescope box (ohmic side), which contains the module and its electronics, in the beam line: the repeater and the opto-coupler are shown.

The 128 output signals are multiplexed on a single output line with a maximum frequency for the readout clock of 10 MHz. The three ASICs are AC coupled to the CSEM[2] double side silicon detector with external quartz capacitors. They are interfaced with the rest of the frontend electronics with a multi-layer ceramic hybrid.

The n-side signals are level shifted by an opto-coupler and the output signals of both sides are conditioned by a repeater card (the readout electronics is shown in figure 3.5(b)); this card provides the bias voltage, the power and the control signals to the hybrid. The analog signal is converted to a digital one by a CAEN V550 Analog to Digital Converter (ADC), which is able to perform the so-called "zero suppression": the DAQ system reads only the strips which exceed a predefined threshold, reducing the amount of data to transfer and collect.

In the commissioning phase, the telescope spatial resolution (figure 3.7) has been evaluated using the residual method. The residual distributions of a detector are measured positioning the detector itself between other two: since residuals are a function of the multiple scattering and the spatial resolution, the detectors have to be very close in order to reduce the first factor. The residual consists, in practice, of the difference between the position readout by the detector and the one reconstructed by the external ones: for the module in figure, the RMS values are 4.76 μm for the horizontal plane (junction side) and 12.37 μm for the vertical one (ohmic side).

[2] *Centre Suisse d'Electronique et de Microtechnique SA*, Rue Jaquet-Droz 1,CH-2002, Neuchâtel

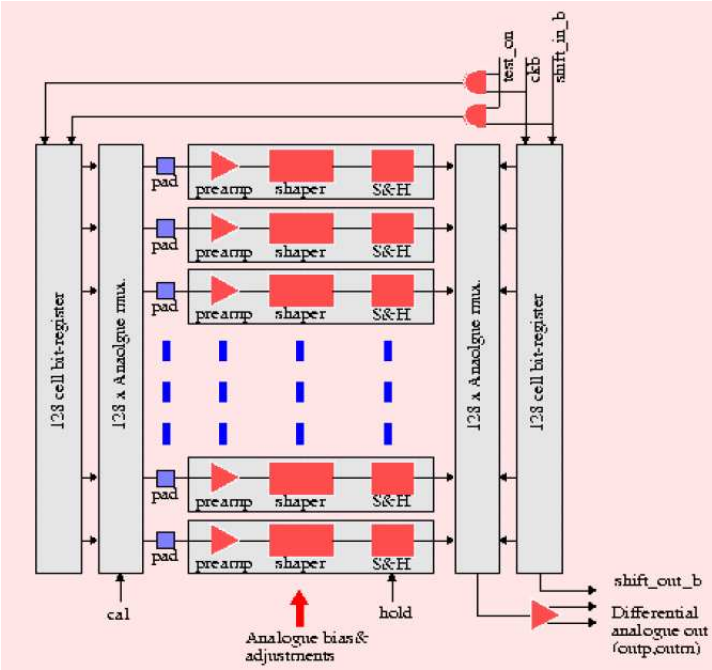

Figure 3.6: The VA2 ASIC architecture (from datasheet). S&H stays for sample & hold.

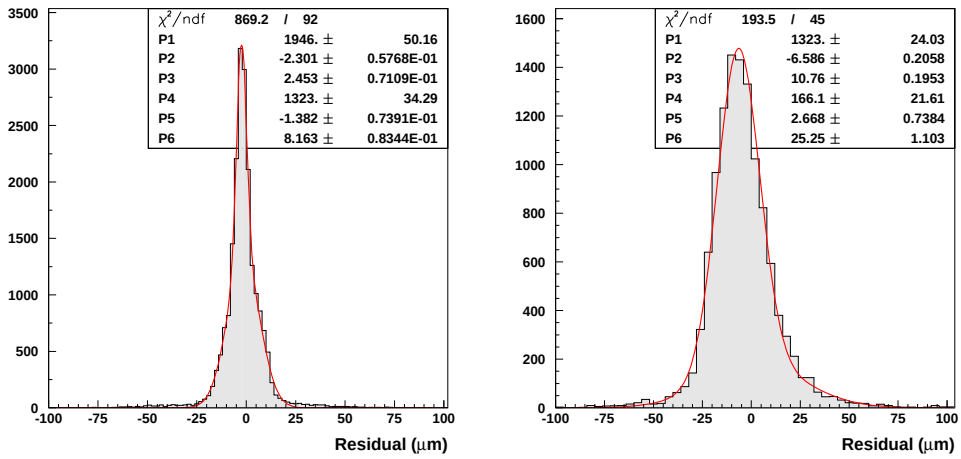

(a) (b)

Figure 3.7: The residual distribution of a telescope: the average RMS values of the (a) horizontal and (b) vertical sides of the telescope are 4.76 μm and 12.37 μm.

The *AGILE beam chambers* have been built for the test phase of the ASI space

experiment AGILE [69, 70]. Each chamber is formed by two single side silicon tiles of 9.5×9.5 cm^2 and 410 μm thickness arranged in a x-y scheme; the physical pitch is 121 μm, while the readout one is 242 μm: thus a one floating strip readout scheme is adopted. Each tile is readout by three 128 channel self-triggering ASICs (TA1, Gamma Medica-IDEAS, Norway[3]); the readout is a multiplexed one with a maximum clock frequency of 10 MHz. Figure 3.8(a) shows an AGILE module, while figure 3.8(b) presents a photo of a two beam chambers assembly on the beam line.

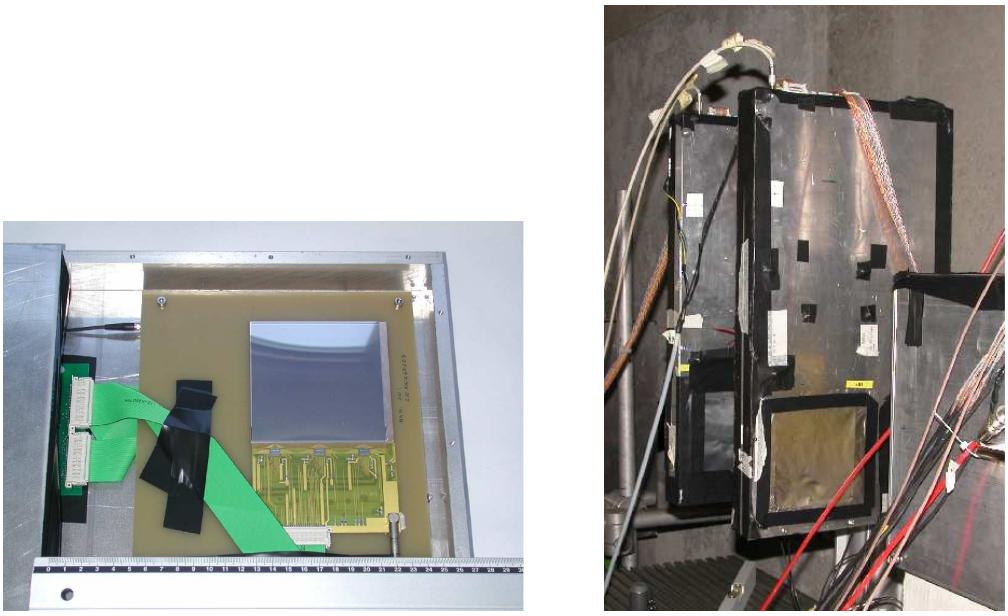

(a) (b)

Figure 3.8: a) The AGILE beam chamber: the strips are readout by the self-triggering TA1 ASICs. b) A pair of the AGILE beam chambers in the beam line.

The residual distribution of the AGILE beam chambers has been measured at the H8 line in the 2006 beam test [66] (figure 3.9).

In appendix A, the procedure for the analysis of the raw data produced by the silicon detectors is described.

3.2.2 Calorimeter for the October 2007 beam test

An electromagnetic calorimeter, DEVA, was built for the October 2007 beam test. DEVA (figure 3.10) is a sampling calorimeter formed by 12 plastic scintillator tiles interleaved with 11 lead tiles (eight tiles 0.5 cm thick and three 1 cm thick): the

[3] http://www.ideas.no/products/ASICs/pdf/TA1.pdf

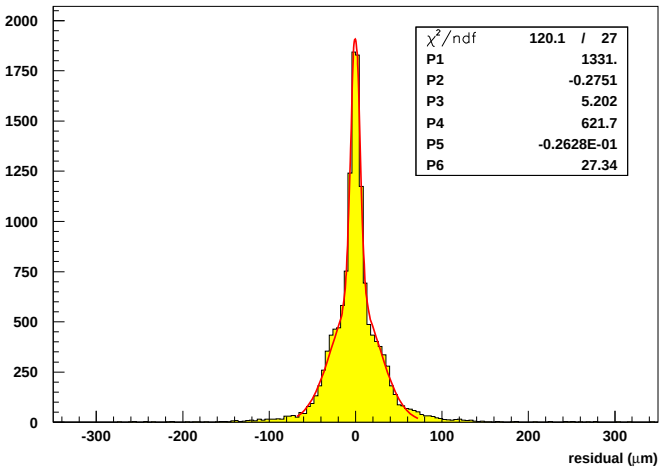

Figure 3.9: The residual distribution of an AGILE beam chamber: the average RMS value is 20.9 μm.

total radiation length is about 13 X_0. Each plastic scintillator tile measures $15 \times 15 \times 2$ cm^3 (the "radioactive" window in figure 3.10(a)) and the light produced is carried by wave-length shifter (WLS) fibers to a multi-anode photomultiplier tube[4] (PMT) (figure 3.10(b)).

A test performed at the Beam Test Facility (BTF) at the INFN National Laboratories in Frascati (LNF) has allowed to measure an energy resolution of the order of $\sigma_E = \frac{9\%}{\sqrt{E}}$+2% for energies lower than 500 MeV/c.

DEVA has been used in the October 2007 beam test both as an electromagnetic calorimeter and a trigger system. The H8 beam, in fact, is not pure (that is it is not made only of electrons or positrons), but contains a percentage of different particles: light leptons were only 23% of the total, while the rest consisted of muons (65%) and light hadrons (π, K). A typical energy spectrum measured by DEVA is shown in figure 3.11(a).

For this reason, in order to select online the lepton events, DEVA has been used in the trigger system; the trigger signal was generated by the coincidence of the scintillators (SciX) and the DEVA last two tile signals discriminated with a high threshold. The resulting spectrum is shown in figure 3.11(b).

The difference between the lepton peak positions in the two figures is due to a

[4]HAMAMATSU 16 anode PMT (R5600-M16).

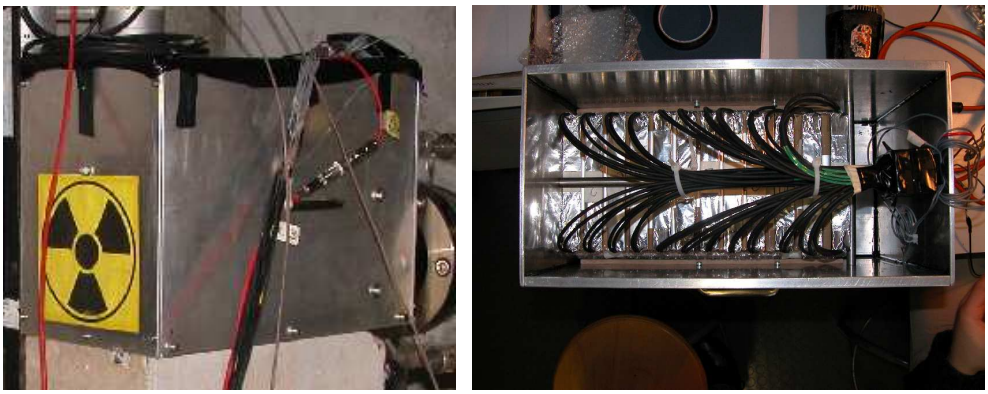

(a) (b)

Figure 3.10: a) The DEVA calorimeter in the H8 beam line: the sensitive area is shown as a yellow ”radioactive“ window. b) Inside the calorimeter: DEVA is formed by 12 plastic scintillator tiles and 11 lead tiles for a total of 13 X_0. The light produced in the scintillators is carried by WLS fibers to a 16 channel PMT.

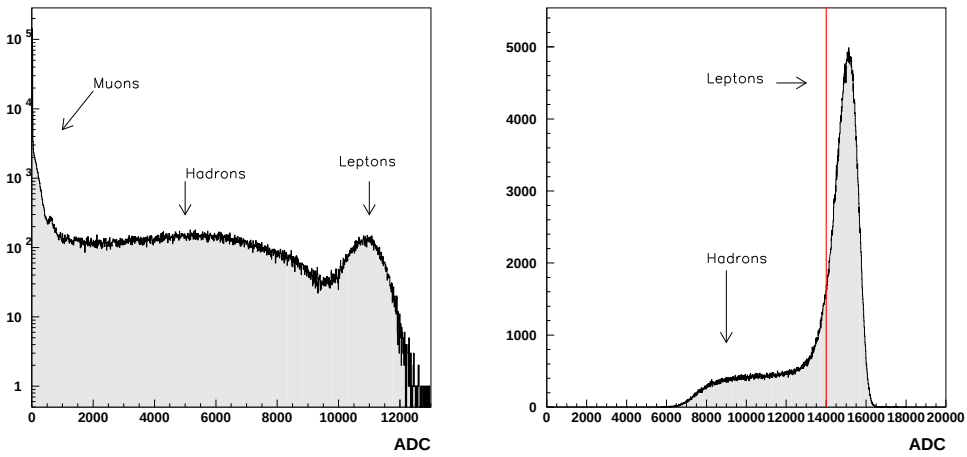

(a) (b)

Figure 3.11: a) The spectrum measured by the DEVA calorimeter: the first peak corresponds to muons, the central region is populated by hadrons while the last peak consists of light leptons. b) The DEVA spectrum for an ”electron” data taking (that is with the last two tiles in the trigger system).

variation of the calorimeter gain[5], because of a different PMT bias voltage.

[5]The runs used in this analysis have an energy spectrum equal to the one in figure 3.11(b).

3.2.3 The DAQ

Figure 3.12 shows the data acquisition (DAQ) chain used in the 2007 beam tests.

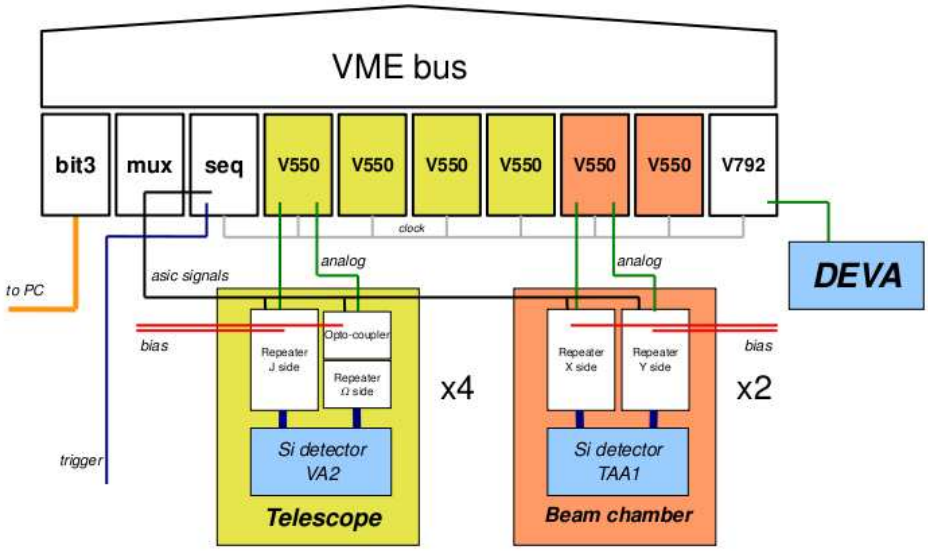

Figure 3.12: The DAQ chain.

The system is a VME one based on a SBS[6] Bit3 620 optically linked to the PC, which allows a VME cycle duration of 1 μs in DMA (Direct Memory Access). The DAQ software is written in C with Tcl/Tk[7] for the user graphical interface (figure 3.13).

An online monitor allows to check the beam profile on a spill by spill basis and on the overall acquired events. The output data are written as PAW[8] ntuples which are processed online to obtain an ASCII file with all the relevant information (appendix A).

The trigger signal is generated by the coincidence of two plastic scintillators (hadron/proton trigger) and the last two tiles of DEVA (electron/positron trigger). The signals used in the trigger are conditioned with a Nuclear Instrumentation Module (NIM) crate and standard NIM electronics. The discriminated signal is sent to a VME sequencer board (seq, INFN Trieste) to generate the DAQ trigger which is the one starting the readout sequence.

The ASIC control signals are generated by the sequencer and carried to the detectors by a 16 pin scotchflex cable; since the sequencer has a single output, a

[6]SBS Technologies, Inc., US, http://www.sbs.com

[7]Tcl (Tool Command Language) is a dynamic programming language and Tk is its graphical user interface toolkit, *http://www.tcl.tk/*

[8]Physics Analysis Workstation, *http://paw.web.cern.ch/paw/*

Figure 3.13: The DAQ user interface.

multiplexer (mux) is necessary to cope with all the modules, that are readout all in parallel.

The interface between the frontend (the detector and the hybrid with the ASICs) and the readout (the VME boards) electronics is represented by the repeater boards (figure 3.14), which are 4 layers PCBs (Printer Circuit Board) with the following tasks:

- transform the RS422 differential signals to single ended ones as requested by the ASICs; the signals are differential in order to transport them to long distances without being affected by noise;

- provide the bias and the digital signals to the ASICs through 50 pin ERNI cables; in particular, silicon detectors require 36 V for the depletion while the repeaters need ± 6 V. The ASIC power rails are ± 2 V and they are generated by power regulators on the repeaters themselves. The digital and the analog supplies are filtered separately. As described in section 3.2.1, the ohmic sides are optocoupled to the readout electronics, that is the "ohmic ground" is set to the bias voltage on the repeater side and to the real ground on the ADC side;

- amplify the analog output of the hybrid (that is the 384 multiplexed channels

of the three ASICs). The output is a differential voltage one (it is converted from current to voltage on the hybrid itself) and is amplified by a NE592;

- in the TA1 case, condition the trigger signal generated by the silicon detectors.

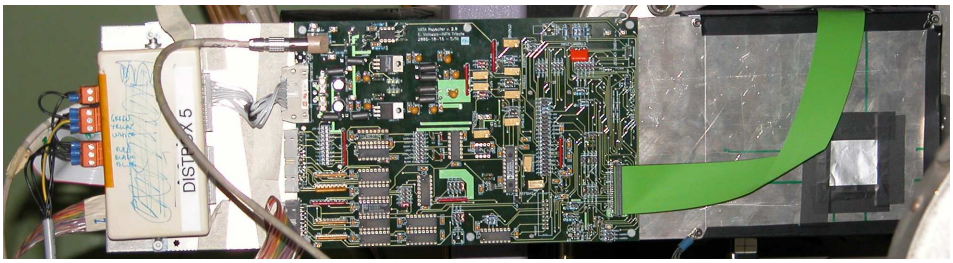

Figure 3.14: The repeater board on a telescope module (junction side). The repeater board is linked to the hybrid by the green ERNI cable on the right. On the left side, from top to bottom, it is possible to see the connectors for the analog signals, power supply, trigger (generated by the module, not used in the telescopes) and the ASIC digital signals.

The analog signals are converted in digital ones by flash ADCs (CAEN V550) for the silicon detector case and an integrating ADC (CAEN V792) for DEVA.

The V550 ADCs work in "zero suppression" mode that is only the channels over a given threshold are readout. During the readout, data are transferred from the ASICs to the ADCs with a 5 MHz clock; in the ADCs, pedestals (see appendix A) are subtracted and the result compared with a threshold that depends on the channel noise. In general, less than 5 strips (out of 384) are over threshold, reducing the readout time dramatically. The readout times can be summarized as follows:

- for the ADC conversion: 384×0.2 μs=76.8 μs; all the module signals are converted in parallel;
- for the transfer from the ADCs to the PC: 5 strips $\times$ 8 modules $\times$ 5 μs (VME cycle) $= 200$ μs.

The total readout time per event is ~ 300 μs, allowing a maximum DAQ rate of 3 kHz.

3.3 The crystals

In 2007 several crystals have been tested: silicon single strip and quasimosaic, germanium and diamond strip crystals, multicrystal systems.

Quasimosaic crystals exploit the anisotropy due to the selection of certain crystallographic planes and orientations. One of these, the QM2 crystal, has been used as a reference because of the detailed analysis performed in 2006 [66]; other quasimosaic crystals (QM3-QM4) have been tested to find the best candidate for the multicrystal system.

Strip crystals bend particles as a function of the only anticlastic force provided by the mechanical holder. The ST9 crystal has been used to investigate the VR dependence on the bending curvature.

Two different multicrystal systems have been tested: the multistrip (from 2 up to 8) and the multi-quasimosaic, where the relative alignment of each crystal is controlled by micrometric screws which can be moved by a remote controlled system (remote screwdrivers or piezoelectric motors).

3.3.1 The quasimosaic crystal

The quasimosaic crystal (figure 3.15) has been prepared exploiting the elastic quasimosaicity effect, which originates from the crystal anisotropy that leads to the curvature of the normal cross sections of the crystal plate under bending.

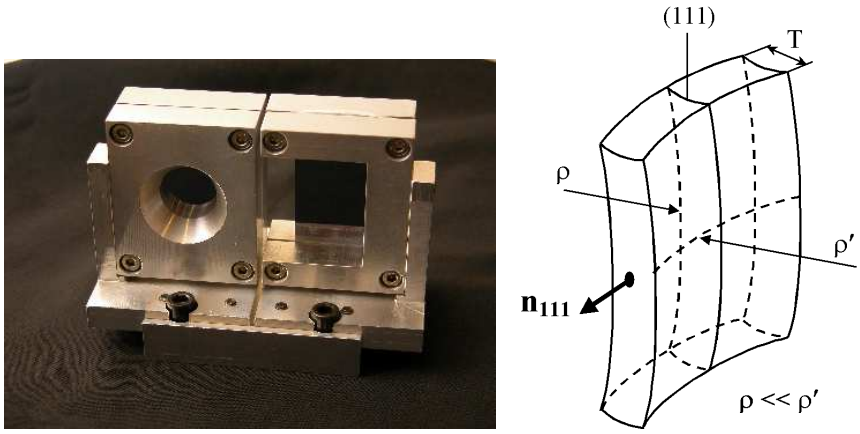

(a) (b)

Figure 3.15: The quasimosaic crystal: a) a pair of quasimosaic crystals mounted on their mechanical holder and b) the mechanism exploited to bend particles.

The quasimosaic crystals are typically prepared in plates of large dimensions (up to $50 \times 50 \times 3$ mm^3); the channeling (111) planes are normal to the large faces and parallel to the long edges. The crystal plates are bent using a special mechanical holder as shown in figure 3.15(a); this primary curvature induces a quasimosaic curvature of the atomic (111) planes in the XZ plane with a curvature angle of the order of 100 μrad (figure 3.15(b)).

The value of the bending angle was cross-checked with X-rays on each crystal finding also that the thickness of the damaged (amorphous) layer (see chapter 1) of the plate surfaces is less than 1 μm.

The quasimosaic crystals used in the H8RD22 experiment have been provided and characterized by the PNPI (Gatchina) group.

3.3.2 The strip crystal

Figure 3.16 shows an example of a strip crystal and the principle behind this technology: a custom process is able to produce strips from (110) or (111) silicon wafers. After a standard cleaning procedure, the wafers are diced to obtain different size strips: in this thesis work, a 7 cm high, 0.5 mm wide and 2 mm long strip has been used (ST9, chapter 4).

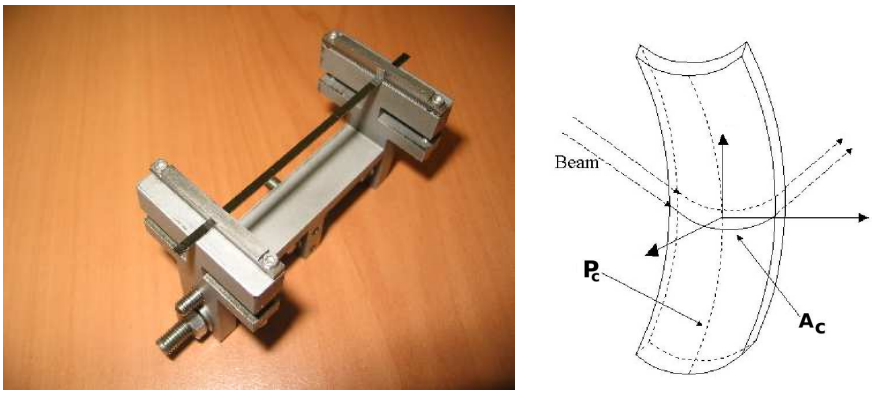

(a) (b)

Figure 3.16: a) A strip crystal mounted on its mechanical holder and b) the mechanism exploited to bend particles. (Courtesy of the INFN Ferrara group)

The crystal is mounted on a specific holder which provides a primary curvature (P_C in figure 3.16(b)) and the consequently anticlastic curvature (A_C), which is used to deflect particles.

In order to induce a minimal lattice damage, a fine grane blade was used to dice the samples. The residual lattice damage was removed through chemical etching in acid solutions: the quality of the etching is verified by RBS (Rutherford BackScattering) measurements [17].

The strip crystals for the H8RD22 experiment have been prepared by INFN Ferrara and IHEP [71].

3.3.3 The multicrystal system

As shown in section 2.2.3, VR is characterized by a large acceptance and efficiency. However the typical deflection angle (of the order of 10 μrad at 400 GeV/c) is too small for crystal collimation; so a multireflection idea was considered to increase the deflection angle, maintaining the VR most important features. The idea is very simple: several crystals are aligned with respect to the beam; when a particle is reflected in the first crystal it enters the second one where it is reflected once more and so on. This idea, validated in the 2006 beam test [66], is schematically shown in figure 3.17.

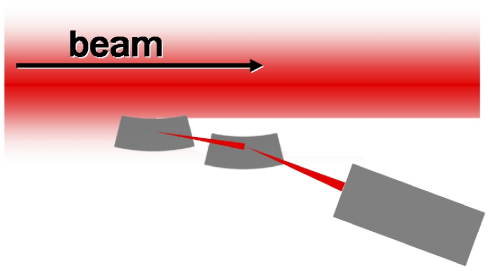

Figure 3.17: The multireflection principle in a collimation system: the particles are reflected in each crystal and the total deflection angle is about $N * \theta_{VR}$, where N is the number of crystals and θ_{VR} the VR deflection angle.

In order to test both the strip and quasimosaic multicrystal systems, two different holders have been used: figure 3.18(a) shows the typical holder (similar to the single strip case) with a eight strip crystal (M8 crystal), while figure 3.18(b) presents the holder for five quasimosaic crystals (MQM5 crystal).

One of the most critical constraints in the multireflection collimation system is the relative alignment among crystals which, in general, is obtained through micrometrical screws on the holder; however this system is too expensive from the point of view of time because, for each alignment step, the beam must be stopped and then checked (in terms of position, divergence, etc.) once the alignment modification has been performed. For this reason two different alignment control systems have been tested in November 2007: the crystals were moved by screws controlled by remote screwdrivers (figure 3.19(a)) or by a piezoelectric system (figure 3.19(b)). In particular this last system has provided excellent results in terms of time, costs and, most important, repeatability (see chapter 4).

(a) (b)

Figure 3.18: The multireflection system: a) eight strips are bent by a holder; the beam comes from the left. b) A new holder conception for five quasimosaic crystals.

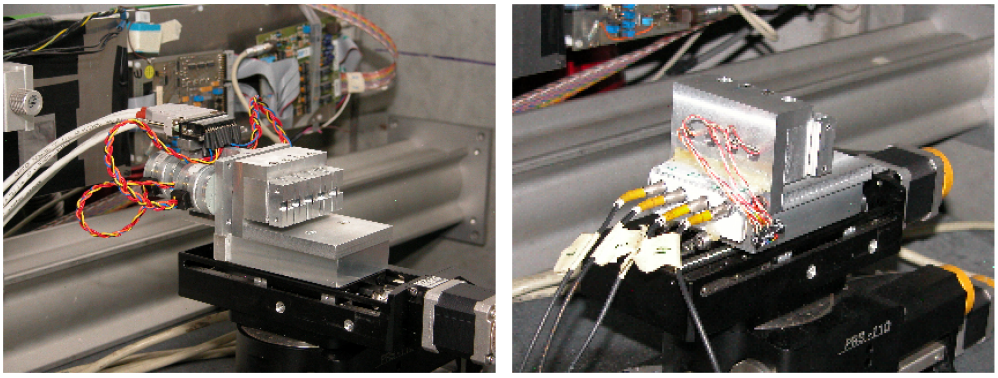

(a) (b)

Figure 3.19: The remotely controlled alignment systems: a) remote screwdrivers and b) piezoelectric motors.

3.4 The goniometer

The holders are positioned on the high precision goniometer system shown in figure 3.20 [71]. The channeling and VR phenomena should be studied with a precision better than the critical angle (which, for a silicon crystal, is about 10 μrad at 400 GeV/c), so the goniometer should provide an alignment precision with respect to the crystallographic planes of the order of 2 μrad.

The goniometer consists of four principal stages (figure 3.20(b) from top to bottom):

- cradle;

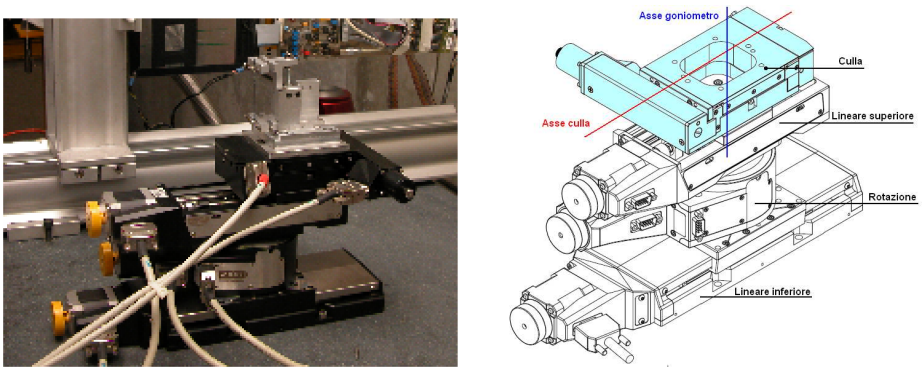

(a) (b)

Figure 3.20: a) A photo of the goniometer in the beam line and b) the goniometer scheme; from top to bottom: the cradle, the small linear stage, the angular stage, the big linear stage.

- small linear stage (upper stage);
- angular stage;
- big linear stage (lower stage).

Table 3.1 shows the performances of the goniometer system in terms of accuracy[9], repeatability[10], resolution and range.

	Accuracy	*Repeatability*	*Resolution*	*Range*
Lower stage	1.5 μm	2 μm	5 μm	102 mm
Upper stage	1.5 μm	2 μm	5 μm	52 mm
Angular stage	1 μrad	2 μrad	5 μrad	360°
Cradle	1 μrad	1 μrad	5 μrad	$\pm 6^o$

Table 3.1: The goniometer system features.

All the stages are equipped with two-phase microstep motors and mechanical limit switches are integrated in the two linear stages.

In order to improve the mechanical stability of the goniometer and to precisely define its relative position with respect to the beam, the whole system was installed on a precisely machined granite table. The goniometer is remotely controlled via the DAQ system.

[9] Accuracy is the degree of closeness of a measured quantity to its true value.
[10] Repeatability is the ability to repeat a motion.

3.5 The new setup at work

For the experiment a very small and parallel beam is necessary: figure 3.21(a) (3.21(b)) shows the beam size in the horizontal (vertical) direction for the 400 GeV/c proton beam. The horizontal RMS is $\sim$ 300 μm, the vertical one is 772.4 μm.

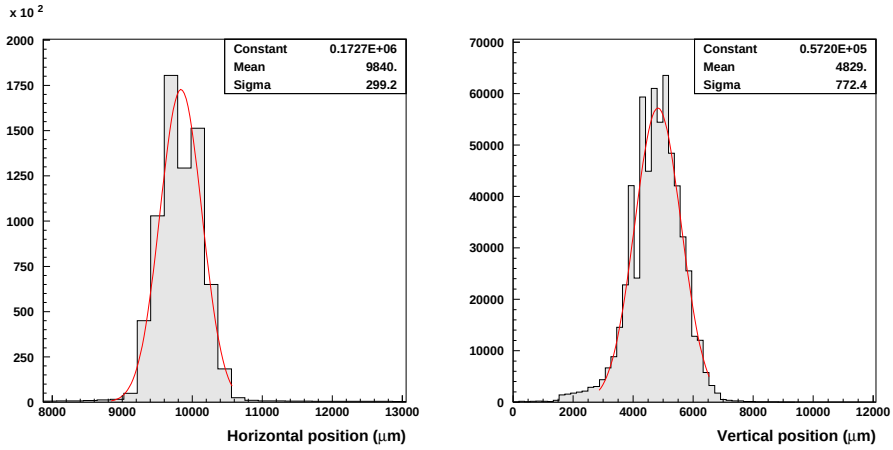

(a) (b)

Figure 3.21: The horizontal (a) and the vertical (b) beam sizes for the proton beam.

The beam size for the light leptons case is bigger. This is principally due to the fact that it is a secondary beam, while the proton beam is a primary one. The beam size for the positron beam is shown in figure 3.22.

The beam profiles can be, in first approximation, fitted with a Gaussian function. During the analysis, both for protons and leptons, a small beam region is considered to reduce the background events present in the Gaussian tails.

The second important beam feature is the incoming divergence: the beam should have a low divergence in order to have a lot of particles with an incoming angle smaller than the channeling critical angle. The incoming divergence is measured by the first two silicon telescopes (Si1-Si2): for protons (figure 3.23) it is 8.66 μrad in X and 12.70 μrad in Y, while for positrons (figure 3.24) it is 25.68 μrad in X and 48.01 μrad in Y. In the analysis, small angular ranges ($\pm$3 μrad for protons, $\pm$4 μrad for leptons) will be considered.

The analysis presented in this thesis work is based on the concept of *deflection angle*, that is the difference between the incoming and the outgoing angles, which allows to become practically independent from the beam features. Figure 3.25 shows the deflection angle in the amorphous and VR positions; note that in the amorphous case the Gaussian spread is only due to the multiple scattering (the detector system angular resolution is, in fact, about 0.5 μrad).

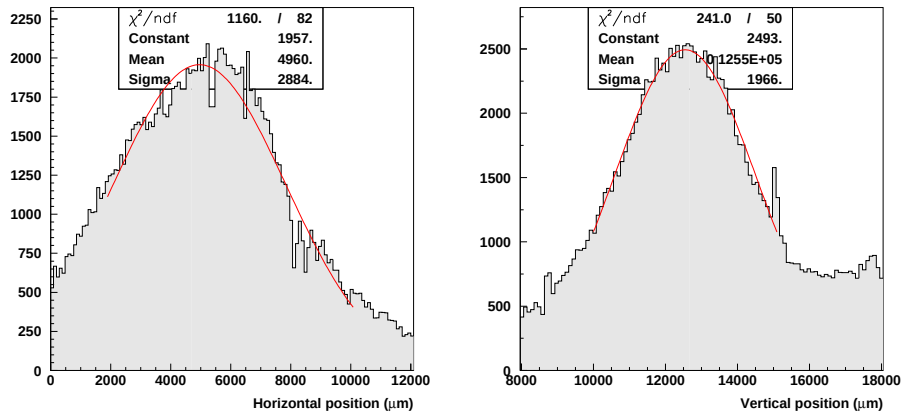

(a) (b)

Figure 3.22: The horizontal (a) and the vertical (b) beam sizes for the positron beam.

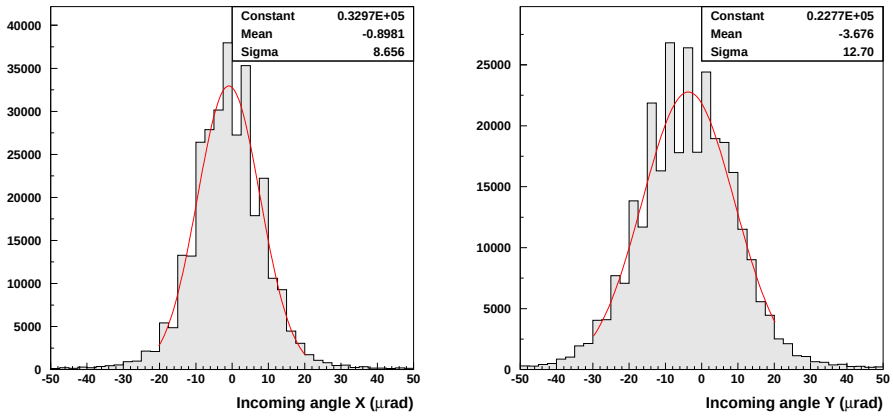

(a) (b)

Figure 3.23: The horizontal (a) and the vertical (b) incoming divergences for the proton beam.

For each crystal measurement, a basic procedure has been followed:

1. the crystal (in its holder) is positioned on the goniometer;
2. the crystal is aligned with respect to the beam with a laser system (section 3.5.1) with a precision of the order of 100 μrad at best;
3. the crystal is positioned on the beam performing a lateral scan and it is identified via its multiple scattering (section 3.5.2);

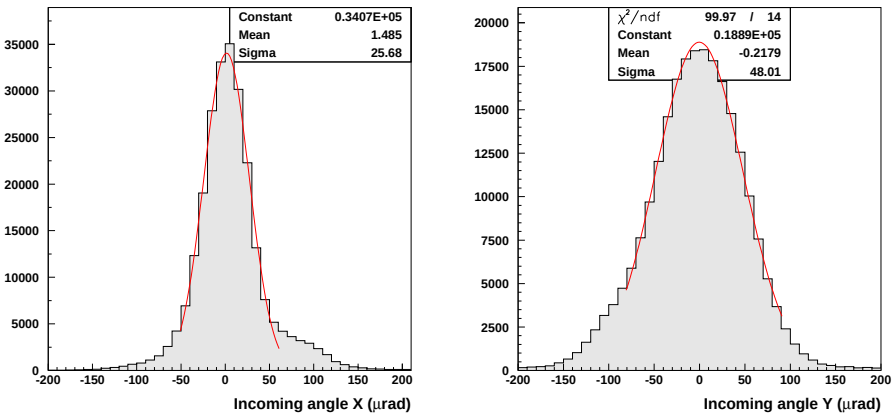

(a) (b)

Figure 3.24: The horizontal (a) and the vertical (b) incoming divergences for the positron beam.

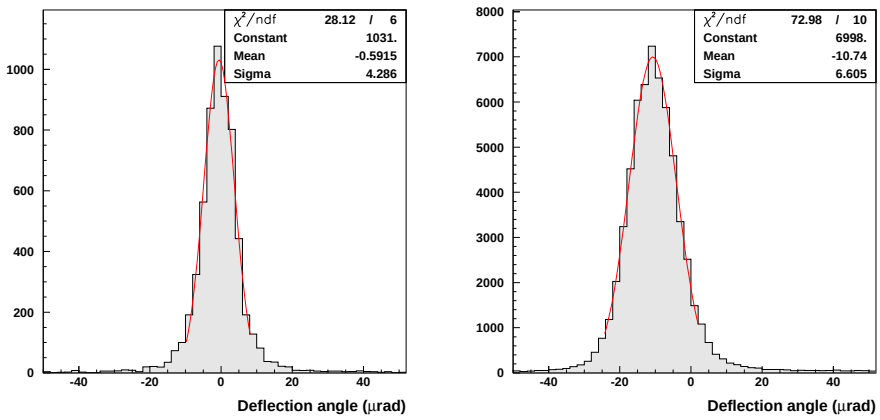

(a) (b)

Figure 3.25: The deflection angle distribution for the amorphous (a) and volume reflection (b) cases. The Gaussian spread in the amorphous case is due to the multiple scattering.

4. a fast angular scan (the step value depends on the VR acceptance) is performed to understand the angular positions of the channeling and volume reflection orientations;

5. a fine angular scan is performed to allow a better analysis of the phenomena with a high statistics.

3.5.1 Pre-alignment

A pre-alignment laser system has been integrated in the setup to align the crystallographic plane with respect to the beam; the method is presented in figure 3.26.

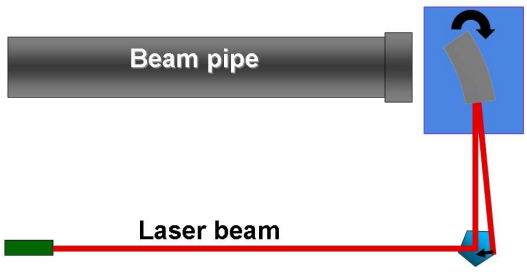

Figure 3.26: The pre-alignment laser system.

A laser light runs parallel to the beam and is projected at 90° towards the crystal surface with a pentaprism. The crystal reflects the beam and when the direct and reflected spots overlap, the crystal is aligned. The precision of this method is of the order of 100 μrad at best.

3.5.2 Lateral scan

In the 2006 experiments, the crystal position was found looking for the multiple scattering of a lead strip located in front of the crystal. Given the performances of the new detector system, the crystal position can be computed exploiting its own multiple scattering.

Thus, after the crystal installation, a lateral scan is performed as shown in figure 3.27.

The crystal is moved through the beam by the goniometer linear upper stage in steps of (typically) 0.5 mm. The multiple scattering of the crystal allows to define its position. Moreover from the lateral scan it is possible to select the geometrical range wherein the particles hit the crystal to apply a geometrical cut to the data to reduce the background events.

3.5.3 Angular scan

Figure 3.28 shows a typical crystal behavior as a function of the goniometer angular position or, in other terms, as a function of the angle between the incoming particle and the crystallographic planes; in the electron/positron cases the angular scan shows also an evidence of the radiation emitted by particles in channeling and VR (chapter 4).

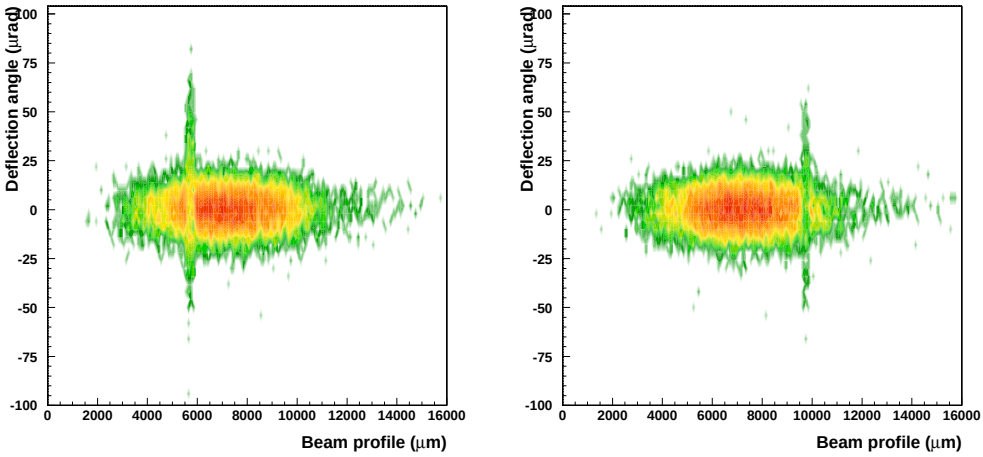

(a) (b)

Figure 3.27: The lateral scan: the goniometer linear upper stage moves the crystal on the beam in steps of 0.5 mm.

Depending on the goniometer angular position the crystal works in different regimes:

Amorphous the deflection angle is characterized by the multiple scattering induced by the crystal and the detectors;

VR volume reflection (VR) is characterized by a large acceptance range ($\sim$ 75 μrad in this case) and a high efficiency. The non-reflected particles can be captured in the channels and form the volume capture (VC) region;

Channeling the channeled particles (CH) are steered with a deflection angle which depends on the critical angle and on the crystal curvature. If a particle loses its channeled condition, the dechanneling (DECH) process occurs.

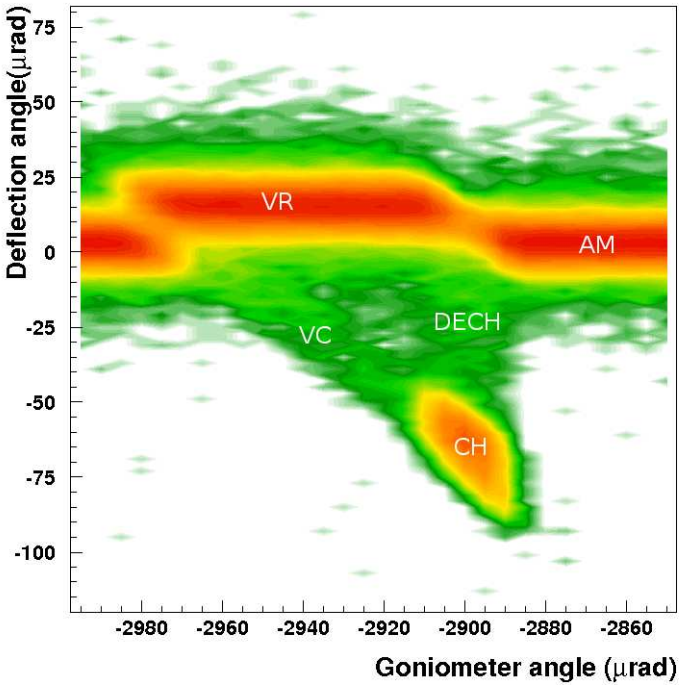

Figure 3.28: The angular scan: depending on the goniometer angular position the crystal could be operated in volume reflection (VR) and channeling (CH); the dechanneling and volume capture are also shown. AM indicates the crystal in the amorphous position, that is non oriented with respect to the beam.

Chapter 4

The experimental results

The first chapter of this thesis work has described a few possible applications of bent crystals in several fields: from collimation to microbeams, from focusing to radiation generation. In several cases, the theoretical hypotheses of new phenomena and their experimental study have been a real breakthrough in the crystal field. The combination of the possibility of using a beam with stringent features and the development of dedicated setups with high resolution and fast detectors allowed "crystal science" to move several steps forward. At the time of writing, the H8RD22 collaboration is being taking data since a month with negative and positive particles, with single and multicrystals.

This chapter intends to summarize at least a part of the studies performed in 2007. The measurements can be divided in two groups:

- study of crystals behavior using relativistic positive and negative hadron beams;
- study of the radiation emitted in bent crystals by light leptons.

As far as the studies with hadrons are concerned, the H8RD22 collaboration goal is the development of a bent crystal based system for the second phase of the LHC collimation. The 2006 results [66] confirmed the VR phenomenon and its possible use for collimation; thus, in 2007, the VR characteristics have been studied with 400 GeV/c protons and 180 GeV/c positive and negative muons and pions to maximize the crystal performance. A deep study of the VR parameters (deflection angle, RMS and efficiency) as a function of the primary crystal curvature has been performed; multicrystal systems have been tested to exploit the multireflection effect and volume reflection with negative particles has been studied with 180 GeV/c muons and pions.

Concerning collimation, another important task is the choice of the crystal material: germanium and tungsten have a potential well greater than the silicon

one (thus the channeling acceptance and efficiency are larger), while diamond can be used for its radiation hardness (and for its thermal properties). In this chapter, the behavior of a diamond crystal is shown.

Bent crystals and channeling related phenomena can be exploited for photon production: a light lepton (electron or positron) which impinges on a bent crystal releases part of its energy as γs; high intensity radiation can be emitted in a single crystal both in the channeling and volume reflection orientations. For the first time, the radiation emitted by 180 GeV/c volume reflected light leptons has been evaluated with respect to the amorphous contribution. This radiation can be used in several fields, from medicine to biology and synchrotron applications. Moreover, concerning the accelerator applications, the study of this radiation is very important for the future International Linear Collider (ILC) in two ways:

- the generation of intense γ beams for a positron source [72];
- the collimation of electron-positron beams [73].

The analysis of the VR dependence on the crystal bending radius and the radiation spectrum emitted by volume reflected electrons and positrons are described in detail. On the other hand, the other items are briefly summarized giving the main results to demonstrate both the vastity of this topic and the amount of work which is being performed.

4.1 Studies with hadrons

The studies with 180 GeV/c and 400 GeV/c hadrons (and muons) have been performed mainly to understand the behavior of the VR phenomenon in different conditions. The measurements performed with positive beams can be summarized in the following way:

- study of the behavior of the VR parameters (the deflection angle, the corresponding RMS and the efficiency) as a function of the primary crystal curvature; the experimental results have been successfully compared with analytical calculations and simulations;
- study of the multireflection effect with two different multicrystal systems: multistrip (from 5 to 8 strips) and multi quasimosaic; in particular, this last system has been remotely controlled with screwdrivers and piezoelectric motors which have demonstrated an excellent repeatability;
- study of a diamond crystal.

The last part of this section is dedicated to the analysis of volume reflection with negative particles, which is a world premiere.

4.1.1 VR as a function of the crystal curvature

One of the goals of the 2007 activity was the study of the behavior of the VR parameters as a function of the primary curvature and the comparison with simulation: a deeper understanding of VR is an important step in the development of novel techniques of collimation for future particle accelerators. A strip crystal (7 cm (high) $\times$ 500 μm (wide) $\times$ 2 mm (thick)), ST9, has been chosen and six different primary bending values have been considered.

In this section the analysis is described in detail for the maximum curvature case (about 36 m). In general, for each bending radius, the measurement procedure required:

- the evaluation of the crystal behavior performing an angular scan;
- the identification of the channeling, volume reflection and amorphous positions where to perform high statistics runs for the offline analysis. In these angular positions, 500000 events have been usually taken.

As an example, figure 4.1 shows the fast (low statistics) angular scan of the 36 m primary curvature ST9 crystal: the black lines indicate two high statistics positions (maximum channeling and volume reflection) while the amorphous position is $\sim$ 80 μrad before the beginning of the scan, and it is not present in the plot.

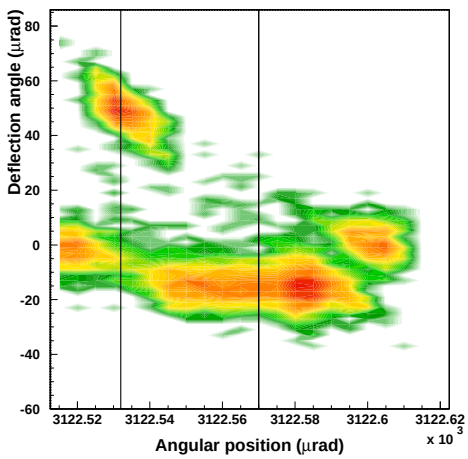

Figure 4.1: Angular scan of the ST9 crystal with a primary curvature of about 36 m.

4.1.1.1 Geometrical and divergence cuts and the critical angle evaluation

In order to improve the analysis, geometrical and divergence cuts have been implemented to select only the particles which hit the crystal. Moreover, the crystal critical angle has been computed from the data to obtain the primary crystal radius from the corresponding channeling position: the primary bending radius, in fact, depends on the mechanical holder curvature which is measured with a pair of micrometers. This measurement has an intrinsic precision on the channeling deflection angle of tens of μrad; moreover, uncontrolled forces on the screws which hold the crystal to the holder could influence the anticlastic curvature (section 3.3.2).

The hit position of a particle on the crystal surface is given by the propagation of the track reconstructed by the first two detectors (Si1-Si2) on the crystal itself. Since Si2 is 33 cm before the crystal, this hypothesis introduces an error of $<1\%$ on the deflection angle measurement.

To select particles which hit the crystal reducing background events, horizontal and vertical cuts have been implemented. As already shown in chapter 3, the beam size at the crystal position is:

- horizontal RMS: 299.23 ± 0.93 μm
- vertical RMS: 772.78 ± 4.84 μm

The crystal is about 500 μm wide; so a part of the beam doesn't hit the crystal itself. Figure 4.2(a) shows the horizontal behavior of the crystal in a volume reflection position: the region limited by the two black lines (9500-9800 μm) indicates the position of the crystal; the rest is due to the multiple scattering induced by detectors and air.

As far as the vertical direction is concerned, the crystal height is about 7 cm; thus a vertical cut is not necessary. However, the Gaussian tails of the beam in the Y direction (corresponding to 20% of the total events) have been excluded from the analysis to reduce background events. Figure 4.2(b) shows the vertical range (from 4000 to 6000 μm) that will be considered in the rest of the analysis.

Divergence cuts are also implemented: in order to know exactly the channeling position and its efficiency (and therefore the curvature radius value, see later on), it is necessary to select only the particles which have an incident angle smaller than the critical one, or, in other terms, the particles which hit perpendicularly the surface of the crystal. The channeling position is typically found with an angular scan as schematically shown in figure 4.3: the crystal positioned on the goniometer (figure 4.3(a)) is rotated till the beam and the crystallographic planes are parallel (figure 4.3(b)).

Given the hypothesis of a parallel beam (divergence equal to 0), this method has an intrinsic resolution due to the angular scan step, which is typically of

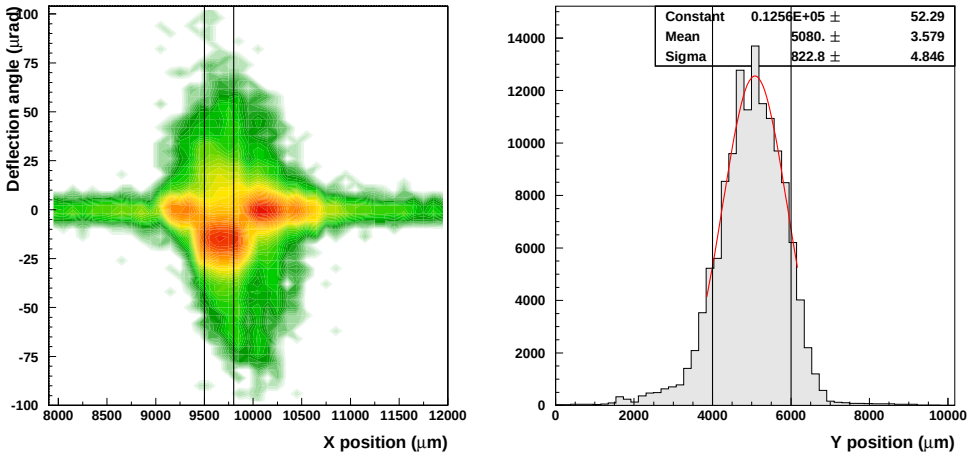

(a) (b)

Figure 4.2: Horizontal (a) and vertical (b) geometrical cuts applied in the analysis to reduce the background events.

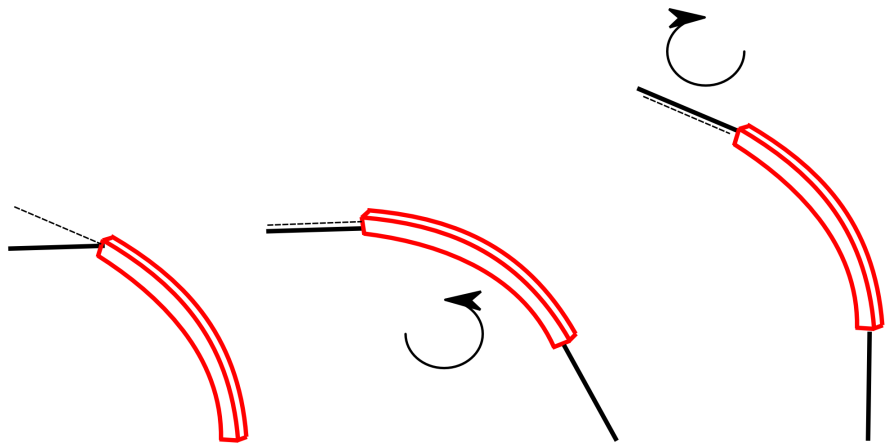

(a) (b) (c)

Figure 4.3: a) A crystal before the alignment: the dashed line corresponds to the atomic plane direction, while the solid line is the beam. The channeling orientation occurs when the two lines overlap (within the channeling critical angle) and can be obtained in two ways: b) rotating the crystal or c) selecting an angular region in the beam.

10 μrad. In order to have a more precise measurement of the channeling position,

a second method has been implemented: the channeling efficiency has been evaluated considering several divergence regions (slices); in practice, it corresponds to performing an angular scan, maintaining the goniometer fixed (figure 4.3(c)). This method is characterized by an intrinsic high resolution since it is independent from the hardware: the larger is the statistics, the more precise is the measurement.

The channeling position is thus evaluated via the measurement of the channeling efficiency which is defined as (if the channeling mean value is positive):

$$\Gamma = \frac{\text{particles in the range greater than}(-3\sigma)\text{ from the channeling peak}}{\text{total particles}} \tag{4.1}$$

and the corresponding error is defined by the binomial statistics:

$$\sigma_\varepsilon = \frac{\varepsilon(1-\varepsilon)}{N_{events}} \tag{4.2}$$

A ± 15 μrad divergence range has been analyzed in slices of 2 μrad using the high statistics run in the channeling position. Figure 4.4 shows the divergence scan in the indicated range: the maximum efficiency position is -3.016 μrad, which can be considered the real channeling position.

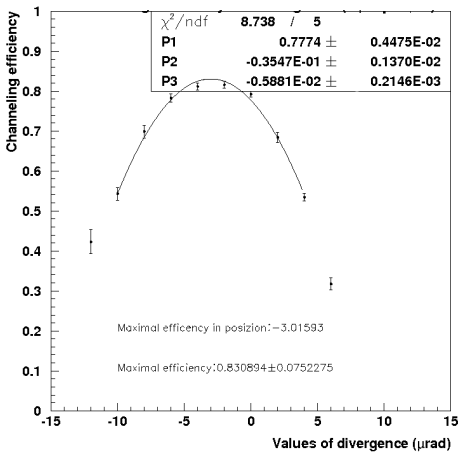

Figure 4.4: The channeling efficiency evaluated considering divergence slices of 2 μrad.

Starting from the new channeling position, the efficiency has been computed increasing the divergence region in steps of 0.2 μrad. The efficiency value has to be constant for deflection angles smaller than the critical one and should decrease from there on. Figure 4.5 shows the efficiency constant behavior until the

critical angle cut-off at ∼8 μrad; the large errors in the first points (due to a very low statistics) are the main reason for a not completely constant behavior of the efficiency: it is, anyway, the first experimental evidence of the channeling critical angle.

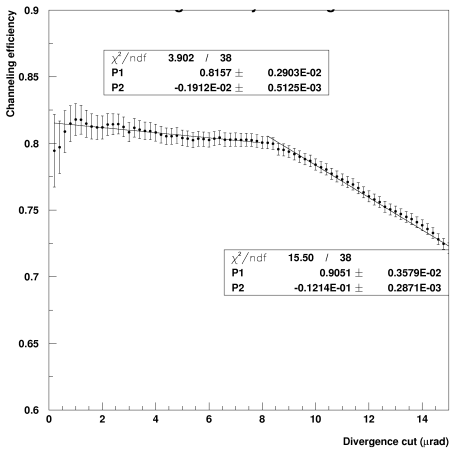

Figure 4.5: The channeling efficiency as a function of the amplitude of the divergence region in the horizontal direction. The step is 0.2 μrad.

According to the previous results, only the particles with a horizontal deflection angle in the range ± 3 μrad will be considered for the analysis.

The vertical divergence is much less critical than the horizontal one. Figure 4.6 shows the efficiency behavior as a function of the increasing divergence region in steps of 0.2 μrad: the trend is clearly constant.

In order to reduce the background events, only the particles with a vertical deflection angle in the range ± 4 μrad are selected.

4.1.1.2 The VR behavior as a function of the crystal primary curvature

The VR parameters (the deflection angle, its RMS and the efficiency) depend on the crystal primary curvature. In order to evaluate the effective VR deflection angle and the RMS, the amorphous contribution due to the multiple scattering produced by the detectors, the crystal itself and the air should be subtracted. Thus, high statistics runs have been taken in the amorphous regions for each different curvature. The amorphous peak has been fitted with a Gaussian to extract its mean and RMS value. Figure 4.7 shows the Gaussian fit of the deflection angle for the 36 m case.

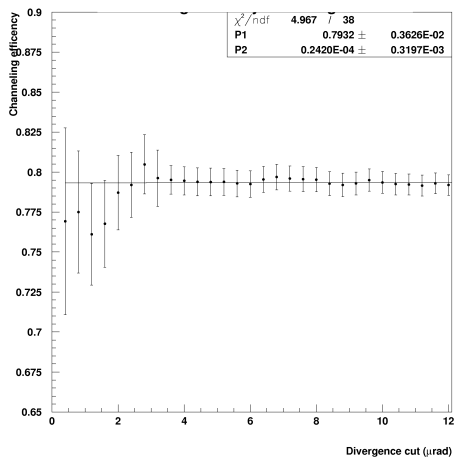

Figure 4.6: The channeling efficiency as a function of the considered divergence region increased in steps of 0.2 μrad in the vertical direction.

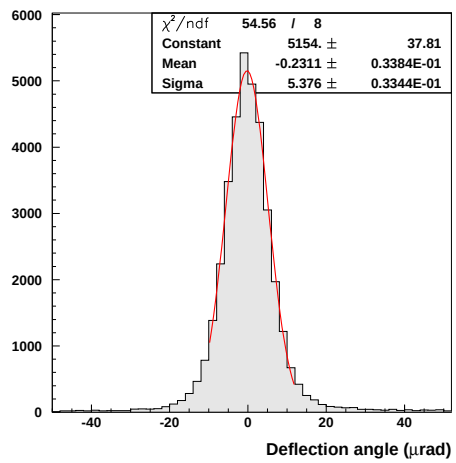

Figure 4.7: Gaussian fit of the deflection angle in the amorphous position for the 36 m case.

If the bent crystal is described as an arc of circumference, the primary curvature dependence on the channeling angle is described by the following equation:

$$R = \frac{T\,[\mathrm{mm}]}{\theta_{chan}[\mu\mathrm{rad}]} * 1000 \tag{4.3}$$

where R is the primary bending radius, T is the thickness of the crystal along the beam direction and θ_{chan} is the channeling angle.

θ_{chan}(μrad)	σ_{chan} (μrad)	R (m)	σ_R (m)
804.36	2.65	2.41	0.02
516.90	3.40	3.75	0.05
433.79	4.22	4.47	0.09
224.56	3.66	8.64	0.28
93.06	2.88	20.85	1.30
53.95	2.72	35.96	3.60

Table 4.1: The channeling peak position, its sigma and the primary bending value with the corresponding error.

The channeling peak has been fitted with a Gaussian function as shown in figure 4.8: θ_{chan} is defined as the difference between the channeling angle obtained from the fit (θ'_{chan}) and the amorphous peak position (θ_{amo}).

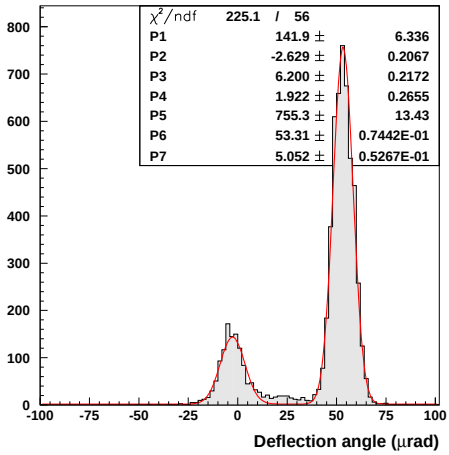

Figure 4.8: Channeling position for the 36 m case: the channeling peak is on the right; the efficiency is not 100%.

Its corresponding sigma is defined as:

$$\sigma^2_{\theta_{chan}} = \sigma^2_{\theta'_{chan}} - \sigma^2_{\theta_{amo}} \tag{4.4}$$

The values of the peak position (θ'_{chan}) and its sigma, the corresponding primary curvature and its error are summarized in table 4.1.

The primary bending radius error can be computed with the propagation of

errors:

$$\sigma_R^2 = \left(\frac{1000}{\theta_{chan}}\right)^2 \sigma_T^2 + \left(\frac{1000\ T}{\theta_{chan}^2}\right)^2 \sigma_{\theta_{chan}}^2 \tag{4.5}$$

The VR peak has been fitted with a Gaussian function as shown in figure 4.9.

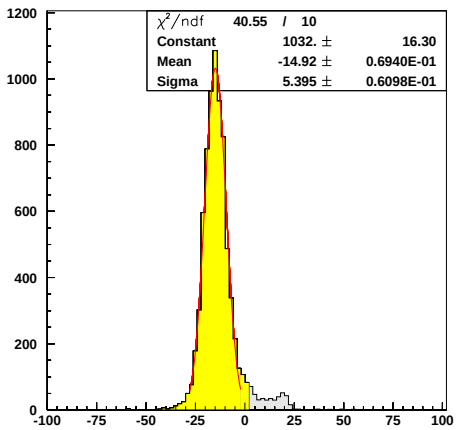

Figure 4.9: The volume reflection position for the 36 m case. The particles with a deflection angle less than +3σ are highlighted in yellow.

The volume reflection angular value (α) is defined as the difference between the peak value obtained with the Gaussian fit (θ'_{VR}) and the amorphous position deflection angle (θ_{amo}):

$$\alpha = \theta'_{VR} - \theta_{amo} \tag{4.6}$$

The VR RMS is defined as:

$$\sigma^2 = \sigma_{\theta'_{VR}}^2 - \sigma_{\theta_{amo}}^2 \tag{4.7}$$

If the VR mean value is negative (that is the amorphous one is 0), the VR efficiency is defined as:

$$\Gamma = \frac{\text{particles in the range lower than}(+3\sigma)\text{ from the VR peak}}{\text{total particles}} \tag{4.8}$$

In figure 4.9 the particles with a deflection angle less than +3σ are highlighted in yellow.

Its corresponding error can be computed with the binomial distribution:

$$\sigma_\Gamma^2 = \frac{\Gamma(1-\Gamma)}{N_{events}} \tag{4.9}$$

Bending radius (m)	$\lvert\theta_{VR}\rvert$(μrad)	σ_{VR}(μrad)	ε (%)
2.41	5.43±0.10±0.64	6.39±0.08±0.47	1.56±0.11±0.1
3.75	8.68±0.14±1.19	4.50±0.12±0.42	2.07±0.21±0.8
4.47	9.89±0.09±0.68	3.80±0.08±0.33	2.64±0.16±0.4
8.64	12.48±0.08±0.45	1.76±0.07±0.17	3.98±0.19±0.2
20.85	13.90±0.16±0.49	1.68±0.15±0.22	5.52±0.31±0.9
35.96	14.08±0.11±0.41	1.10±0.11±0.09	6.22±0.38±1.5

Table 4.2: The VR parameters: the peak position, its sigma and the inefficiency for each value of the primary bending radius with their statistical and systematic errors.

The data obtained in this step of the analysis are shown in table 4.2; ε is defined as the VR inefficiency:

$$\varepsilon = 1 - \Gamma \tag{4.10}$$

To evaluate the systematic errors, each parameter has been computed with different cuts: the cuts implemented in the analysis have been varied and the values for θ_{VR}, σ_{VR} and ε have been recomputed. The maximum difference between the values with the optimal cuts and the recomputed ones has been taken as systematic error. The following cuts have been varied and represent the main contribution:

- geometrical cuts: three horizontal crystal central regions of width 200, 300 and 400 μm and three vertical geometrical cuts have been considered. As far as the horizontal cuts are concerned, a contribution of a few % has been obtained, which is very small due to homogeneity of the strip crystal. The vertical contribution is larger because of a torsional effect of the crystal itself (expecially for the lower bending radii); the total contribution to the final value of the systematic error for the VR mean value and sigma is of 40% at maximum (2.41 m case);

- divergence cuts: the incoming particle angular ranges of ±3, ±4 and ±5 μrad have been considered. The contribution to the systematic error for the VR mean value and sigma is 60% at least;

- the 3σ parameter in the efficiency definition (equation 4.8) has been varied to 2 and 4σ. This contributes $\sim$50% to the efficiency systematic error, while the rest is due to the contributions of the geometrical and divergence cuts;

Figure 4.10 shows the comparison among the experimental, analytical and simulation data: the black dots are the experimental values of the volume reflection peak superimposed on the simulation ones (red squares) and the analytical

curve (continuous line); the pink triangles are the VR RMS values obtained from the data compared with the simulation ones (blue triangles) and the analytical calculation (dashed line).

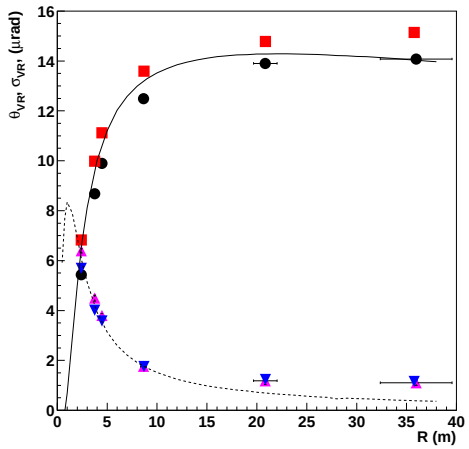

Figure 4.10: The VR peak position and its corresponding RMS: comparison between experimental (black dots for the mean value and pink triangles for the RMS) and simulation data (red squares and blue triangles) and the analytical calculation (lines).

Figure 4.11 shows the comparison among the VR inefficiency experimental (black dots), simulation (red squares) and analytical data (black lines): ε_1 is the probability of the particle to lose a transverse energy smaller than the critical energy and ε_2 is the probability for the particle to enter in the channeling regime; the experimental data should be positioned in the region between ε_1 and ε_2.

Taking into account the obtained results, an optimal bending radius for a short silicon crystal (few millimeters) to maximize the VR performance is found to be about $10R_c$ (15 m, see equation 2.30). At this value, the deflection angle is maximum and the efficiency is high. In general, the higher is R, the larger is θ_{VR}, but the efficiency and the angular acceptance decrease. To obtain the same acceptance, the crystal length should be increased but this generates more particle losses in inelastic interactions with the crystal nuclei.

4.1.2 The multicrystal

As explained in section 3.3.3, the multicrystal effect can play an important role for collimation. In the 2007 beam tests, two different multicrystals have been studied:

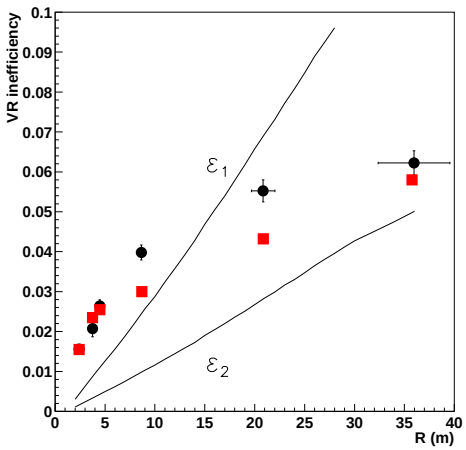

Figure 4.11: The VR inefficiency: comparison between analytical (lines), experimental (black dots) and simulation (red squares) data. ε_1 is the probability of the particle to lose a transverse energy smaller than the critical energy and ε_2 is the probability for the particle to enter in the channeling regime.

- a multi quasimosaic crystal (MQM5) remotely controlled by screwdrivers and piezoelectric motors (figures 3.19(a) and 3.19(b), respectively).
- several multistrip crystals (from the IHEP and Ferrara groups) with 5, 6 and 8 strips each.

The MQM5 analysis presented in this section is based on the results obtained with the piezoelectric motors: the relative crystal alignment, the behavior of the channeling and volume reflection orientation and the system repeatability are given.

MQM5 consists of five $5 \times 5 \times 1$ mm^3 crystals with a channeling deflection angle of ~ 80 μrad and a volume reflection one of ~ 10 μrad. In a first phase, the crystals have been aligned among them in order to optimize the volume reflection deflection angle: the crystals have been moved with the piezoelectric motors in order to send the volume reflected particles of the first crystal to the second one and so on (figure 4.12).

Considering the best relative alignment among crystals, the final result is shown in figure 4.13: the channeling peaks seem to be very close (moreover the total acceptance is more or less that of a single crystal), while the volume reflection deflection angle has reached ~ 50 μrad, preserving the acceptance of ~ 80 μrad.

To be more quantitative, figure 4.14 shows the performance of the MQM5 crystal. High statistics runs in the crucial angular positions allow to note that

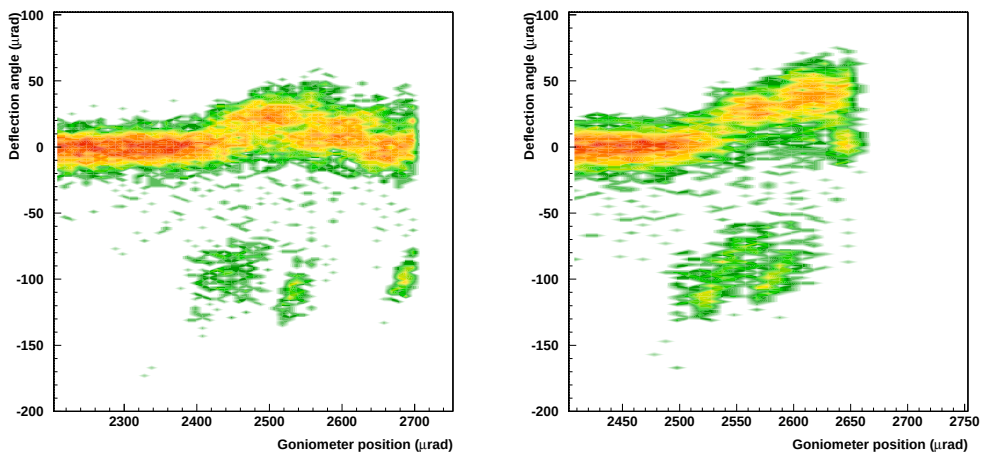

(a) (b)

Figure 4.12: The MQM5 alignment: going from a) to b), the piezoelectric motors have been moved to optimize the angular behavior of the crystals. The scans are fast (low statistics) angular scans.

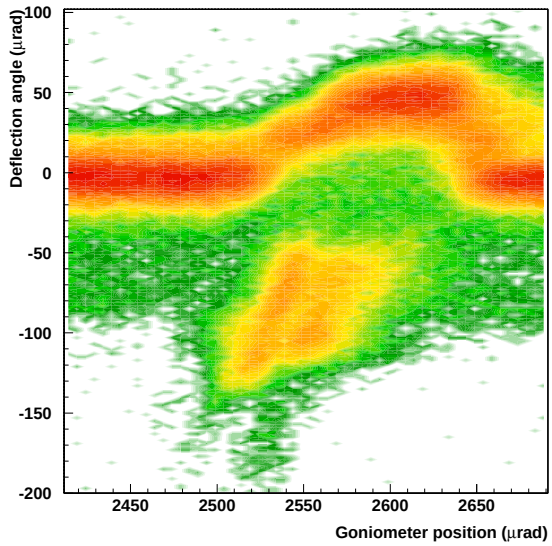

Figure 4.13: The MQM5 fine angular scan.

crystals were not perfectly aligned, which is the reason why in figure 4.14(a) there are two channeling peaks at -107.3 ± 0.7 μrad and -66.53 ± 0.75 μrad.

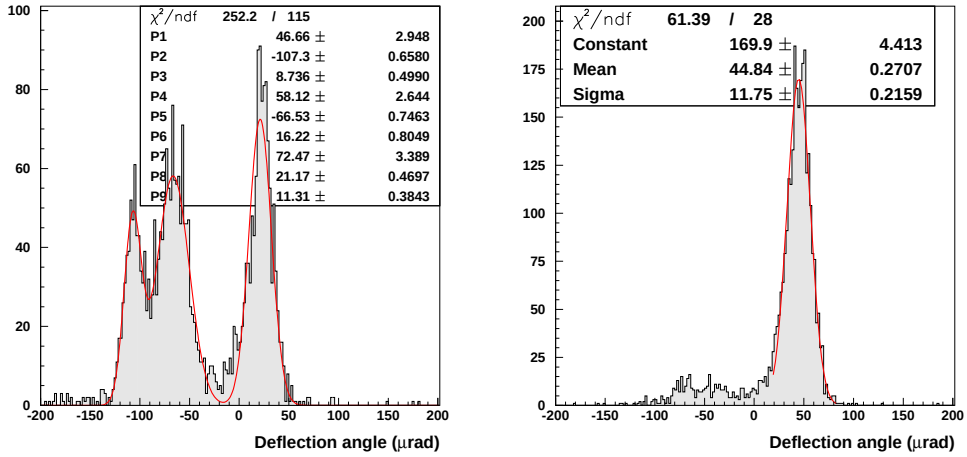

(a) (b)

Figure 4.14: The MQM5 performances: a) two channeling defection angle peaks are present at -107.3 ± 0.7 μrad and -66.53 ± 0.75 μrad; b) the VR final deflection angle is 44.84 ± 0.27 μrad.

On the other hand, in the VR orientation the crystal behaves as expected: the acceptance remains of the order of 80 μrad, but its deflection angle increases up to 44.84 ± 0.27 μrad. The efficiency has been evaluated according to equation 4.8 and reaches a maximum value of $(80.0 \pm 0.4)\%$; in the acceptance range $(2570 - 2650$ μrad) the efficiency is higher than 60%, as shown in figure 4.15.

The efficiency value is due to several factors, among which the two most important are:

- an intrinsic inefficiency of each single crystal due to a non homogeneity of the quasimosaic technique and an eventual amorphous layer on the crystal surface;
- a non perfect relative alignment of the crystals: in the middle of the VR, where the efficiency is the largest, a channeling peak anyway is present; it means that a part of the beam is steered in a direction by the multireflection effect and a part in the other direction through the channeling orientation.

A repeatability test on the system has been performed: the volume reflection mean deflection angle value and maximum efficiency has been measured for three times. The repeatability test procedure was the following:

- the five piezoelectric motors (one per crystal) have been switched off and have been left off for 10 minutes to cope with hysteresis;

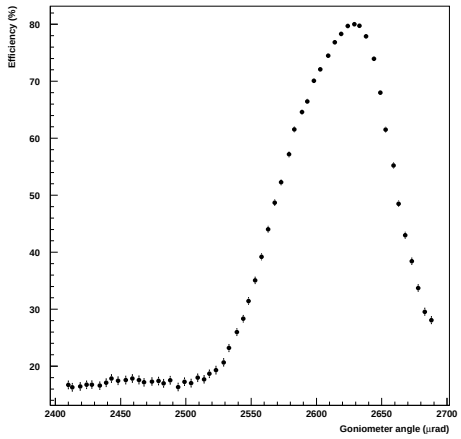

Figure 4.15: The MQM5 VR efficiency: in the acceptance range (2570 − 2650 μrad) the efficiency is higher than 60%, with a maximum value of (80.0 ± 0.4)%.

	VR deflection angle (μrad)	*Efficiency (%)*
1	44.84 ± 0.27	80.0 ± 0.4
2	44.04 ± 0.39	80.4 ± 1.1
3	44.83 ± 0.32	80.8 ± 0.8
Mean value & standard deviation	44.57 ± 0.45	80.4 ± 0.42

Table 4.3: The repeatability test results on the MQM5 crystal remotely controlled by piezoelectric motors.

- each piezoelectric motor power supply has been switched on and the voltage values (from 10 to 70 V) used for the first alignment have been set.

The procedure has been repeated for three times; the results are summarized in table 4.3. The piezoelectric system resulted to be very stable in terms of repeatability: the standard deviation is, in fact, comparable with the experimental errors.

A second multicrystal system has been tested in 2007: M8 (IHEP) consists of 8 strip crystals bent by a common holder (shown in figure 3.18(a)). The multistrip crystal system doesn't foresee an independent relative crystal alignment as in the quasimosaic case: it means that if a crystal is not aligned, it is not possible to correct its position. The M8 crystal performances are shown in figure 4.16: figure 4.16(a) presents the angular scan with the multireflection of six crystals. The main results can be listed as following:

- the total deflection angle reaches 61.21 ± 0.53 μrad;
- the efficiency is greater than 90% (figure 4.16(b)).

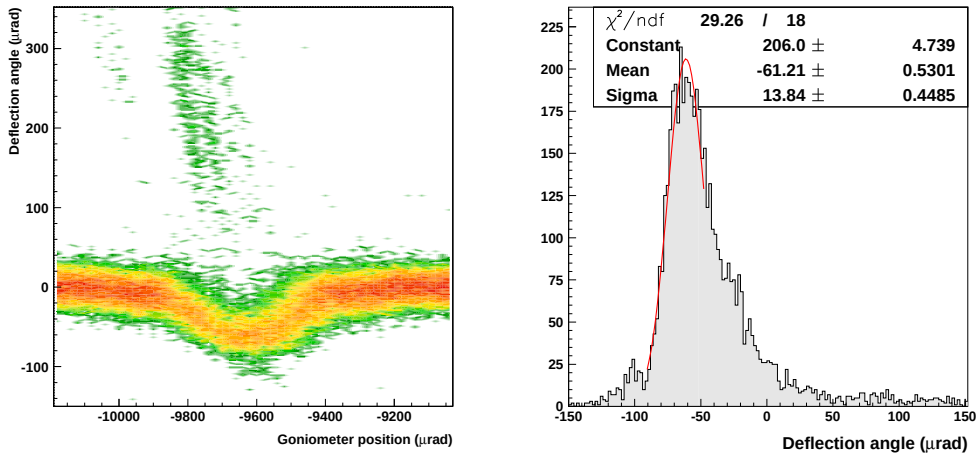

(a) (b)

Figure 4.16: The M8 multistrip crystal performances: a) the angular scan shows the multireflection of 6 crystals; b) the total deflection angle is 61.21 ± 0.53 μrad and the efficiency is greater than 90%.

This system has shown several positive features: strip crystals are typically positioned on a C-shaped holder (figure 3.16(a)), so no multiple scattering effects on the holder are foreseen; from this point of view the quasimosaic crystals, being smaller (figure 3.19(a)) and needing to be held all around, could have problems for a collimation application on an accelerator. Moreover the strips are simply bent by a common holder, so no remote controls are requested, making life much easier in an accelerator; no controls mean also more strips in a single assembly and thus a larger deflection angle. On the other hand, also the strip requires a few improvements: from the technology point of view a reliable technique has to be found to produce a multistrip crystal from a single piece of silicon; a mass production is needed to understand if the technology is fail proof and to analyze in detail the features of the strip crystals in view of a large scale application.

4.1.3 Diamond crystal

In general, bent crystals are made of silicon because of its abundance and of the level reached by the silicon technology (thanks to the fact that silicon is the base of microelectronics). However other materials like germanium, tungsten or diamond

are characterized by features that could result fundamental for some applications: the potential well is deeper in germanium and tungsten (see table 2.1), while diamond is radiation hard and thermally stable. In this section a description of the performance of a diamond crystal is given.

Figure 4.17(a) shows the diamond crystal on its holder: the crystal is the little piece at the end of the aluminum bar. Its dimensions are: 6 mm (height) $\times$ 2 mm (thickness) $\times$ 150 μm (width). Because of its small dimensions, it has been necessary to put a lead strip in front of the crystal to have a large multiple scattering to align the crystal itself on the beam.

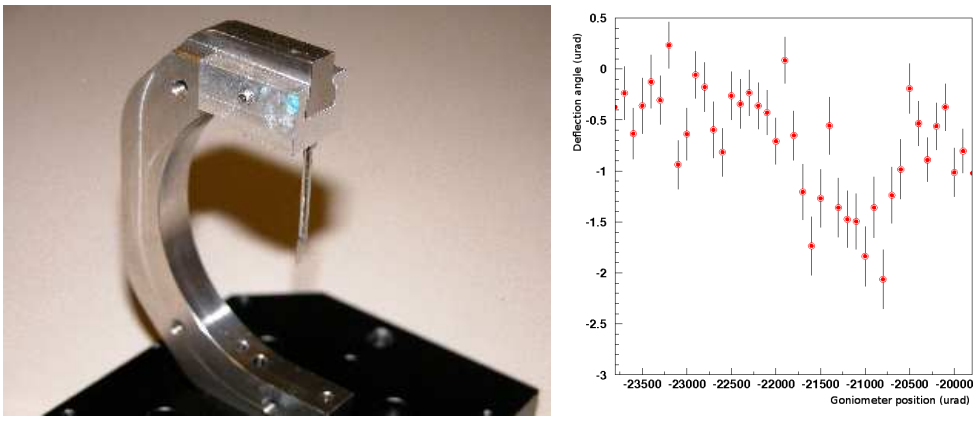

(a) (b)

Figure 4.17: The diamond crystal. a) The diamond crystal in its holder: the primary curvature is obtained by microscratches on one of the crystal faces. b) The volume reflection.

Like the crystal undulator, the crystal curvature has not been provided by a mechanical holder but through a series of microscratches on one of the crystal surfaces: if the grooves are implemented on a single side, the atomic electric field is rearranged to produce bent channels.

The performance of the diamond crystal is shown in figure 4.17(b): the red points correspond to the mean values of the deflection angle distribution for each point of the angular scan; the error bars correspond to the RMS. The mean volume reflection deflection angle is about 1.5 μrad, and the acceptance is of the order of 1 mrad; no channeling peak has been found.

The obtained results are not discouraging: the crystal has been characterized for the first time with the H8RD22 experimental setup; no X-ray measurement, in fact, had been performed before putting it on the beam. Such a limited performance is probably due to the fact that the microscratch method is not precise like the mechanical holder one, meaning that the bending could be very different from

what expected. The success of this trial lies in the fact that the H8RD22 setup can be seen as a factory to test new crystal materials and production technologies.

4.1.4 The negative particles

Volume reflection with negative hadrons and muons has been experimentally confirmed in the October 2007 beam test on the SPS H8 line and later, in August 2008, on H4, exploiting the same setup (figure 3.4). The 180 GeV/c incoming beam consisted mainly of negative muons (50%) and pions/kaons (50%); the energy loss spectrum (in ADC units, measured by DEVA) is shown in figure 4.18: the low energy peak corresponds to muons (which are MIPs), while the rest of the spectrum identifies negative pions and kaons.

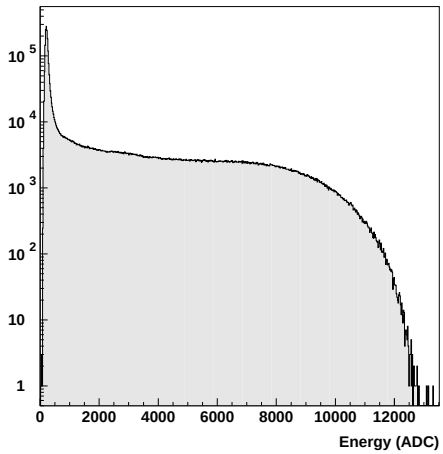

Figure 4.18: The 180 GeV/c negative beam energy loss spectrum: the peak at low energy corresponds to negative muons, the rest is populated by pions and kaons.

The negative beam features are presented in figure 4.19: figure 4.19(a) shows the horizontal beam profile which has a RMS of 1.8 mm (while the vertical one is 2.1 mm); the incoming X divergence is 34.37 μrad (figure 4.19(b)), while the Y one is 27.55 μrad.

In the analysis, a geometrical region of 1 mm^2 around the beam center has been considered. Particles with an incoming horizontal angle in the ± 8 μrad range (according to the critical angle that should be ~ 15 μrad at 180 GeV/c) have been taken into account.

Volume reflection with negative particles has been tested both with strip and quasimosaic crystals: in particular the studies presented in this section have been performed with the quasimosaic QM2 crystal (figure 3.15(a)).

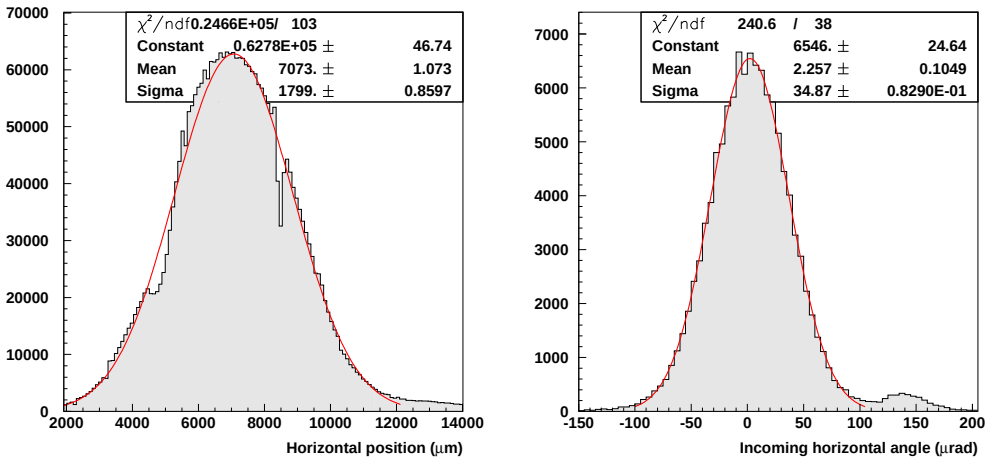

(a) (b)

Figure 4.19: The 180 GeV/c negative beam: a) the horizontal profile RMS is 1.8 mm (the vertical one 2.1 mm); b) the X divergence is 34.37 μrad (the Y one 27.55 μrad).

Figure 4.20 shows the angular scan of the QM2 crystal with negative particles: this plot should be compared to the one with positive particles in figure 3.28. As

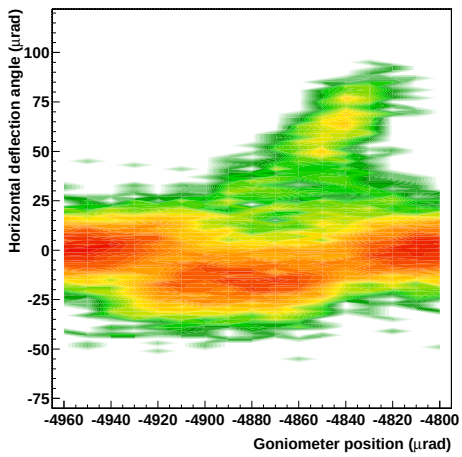

Figure 4.20: The angular scan of QM2 with negative particles.

far as the channeling orientation is concerned, negative particles have a higher dechanneling probability with respect to the positive ones. The mean channeling deflection angle (right peak in figure 4.21(a)) is 59.47 μrad and its efficiency is

(28.2 ± 1.6)%, while the dechanneling efficiency (events within the two peaks) is (9.3 ± 0.8)%[1], larger than the one measured with positive particles (∼5%) [66]. It is due to the fact that the minimum of the potential for negative particles is close to the atoms, so the probability to lose the channeling condition is higher. The volume reflection phenomenon has had the experimental confirmation in the

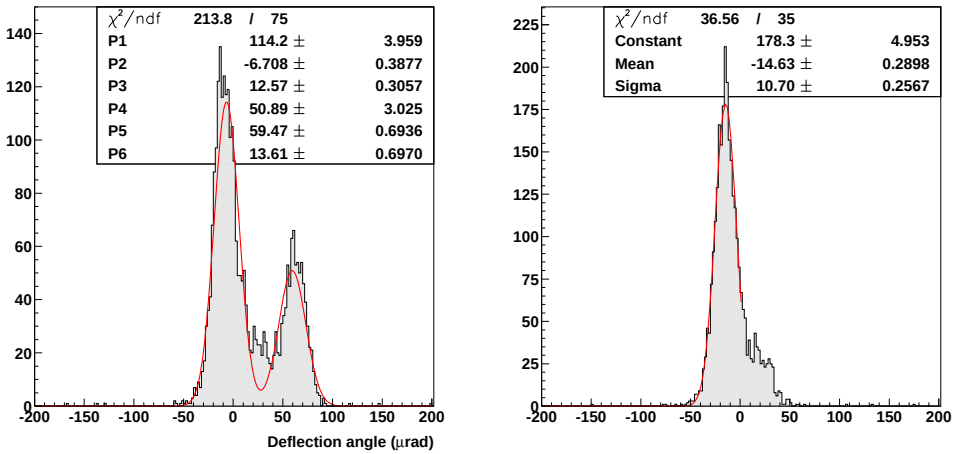

(a) (b)

Figure 4.21: The channeling (a) and volume reflection (b) orientations with negative particles in the QM2 crystal. In figure (a) the channeling peak is on the right.

October 2007 beam test; figure 4.21(b) shows the corresponding deflection angle distribution: the most probable value is 14.63 μrad, while its efficiency is (90.54 ± 0.6)%.

4.2 Light particles: electrons and positrons

The analysis of the radiation emitted by 180 GeV/c positrons/electrons in a volume reflection orientation is presented in this section. The study of the radiation emitted by volume reflected particles is still an open field, given the constraints on the beam and on the experimental setup. On the other hand, these studies could be a real breakthrough for several applications:

- the generation of intense γ beams for a positron source [72];

[1] The dechanneling efficiency has been evaluated as the difference of the channeling and amorphous ones, according to the definition given in equation 4.1.

- the collimation of electron-positron beams at the future linear collider [73];
- the generation of intense γ beams for medical applications.

For the 2007 beam test the setup shown in figure 3.4 has been used; the results have been obtained exploiting what can be defined a spectrometer method, which will be described in section 4.2.2, and have been compared with the analytical calculations.

4.2.1 The crystal behavior with light particles: analysis cuts and angular scan

Similarly to the proton case, the incoming particle trajectory is computed using the spatial information of the Si1-Si2 microstrip silicon detectors (section 3.2.1), while the outgoing one is based on the information of Si2 and BC3 (because of multiple scattering, BC4 is used in place of BC3 only in case of a missing hit on BC3 due to a dead channel); the quasimosaic QM2 crystal has been positioned on the high precision goniometer (section 3.4).

The beam particles (which could be light particles, muons or light hadrons) are "discriminated" by the electromagnetic lead-scintillator calorimeter, DEVA (section 3.2.2). The energy spectrum of the whole beam is shown in figure 3.11(a): the beam is formed by muons (65%), hadrons (12%) and leptons (23%). An event has been identified as a lepton if its signal exceeds an energy threshold of 14000 ADC (red line in figure 3.11(b)).

As far as geometrical cuts are concerned, it must be considered that in principle, a particle impinging on the crystal should be deviated independently from its hit position on the crystal surface. However, as already shown in previous beam tests, this is not true and the deflection angles depend on the hit position, especially in the vertical direction (further explanations can be found in [66], while an example will be presented later).

In order to obtain a homogeneous answer of the crystal behavior, therefore reducing the background events, geometrical cuts have been implemented. Figure 4.22 shows the horizontal and vertical beam profiles at the crystal position (reconstructed with the first two detectors): the Gaussian fits provide the RMS values that are of the order of ~ 2.8 mm in X and ~ 2 mm in Y.

The vertical red lines in figure 4.22 define the useful beam range: [5000,7000] μm in X, [12000,13500] μm in Y.

The incoming divergence has been measured by the first two silicon detectors to be 25.07 μrad in X and 46.50 μrad in Y (figure 4.23).

The bent crystal is characterized by a critical angle of the order of 15 μrad at this energy. As already said, it is fundamental to select particles with incoming

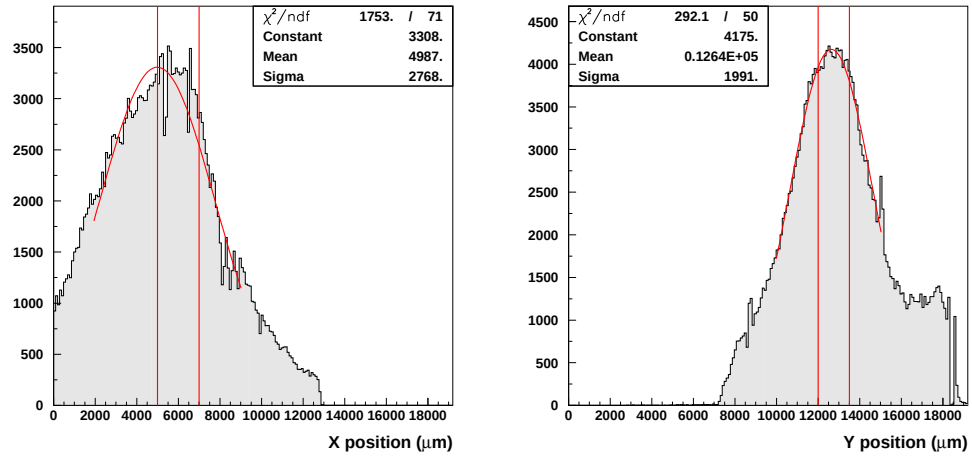

(a) (b)

Figure 4.22: The horizontal (a) and vertical (b) beam profiles at the crystal position.

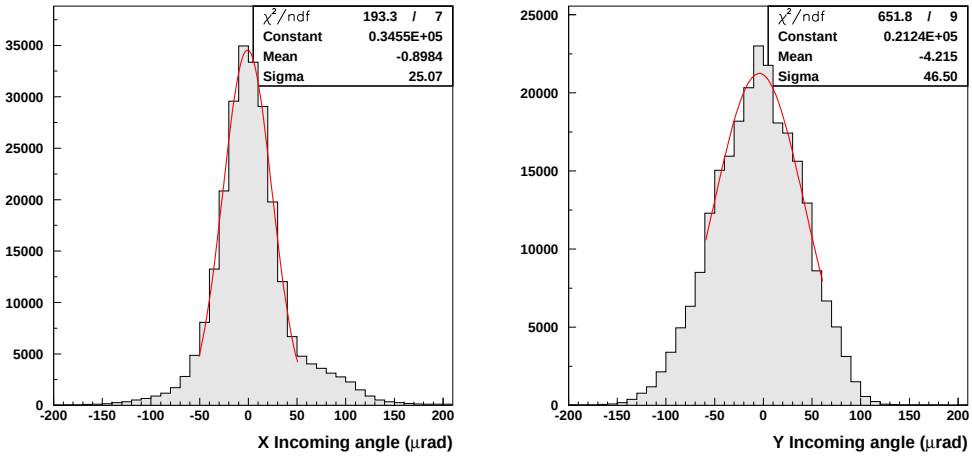

(a) (b)

Figure 4.23: The horizontal (a) and vertical (b) incoming angle distributions.

angles smaller than the critical one. In other terms, a horizontal divergence cut is necessary: only the particles with an incoming angle in the ± 4 μrad range have been considered for the analysis.

In the vertical direction the problem is not so critical, so no divergence cuts have been implemented.

Figure 4.24(a) shows an angular scan of the QM2 crystal with 180 GeV/c

positrons: the crystal goes from the amorphous condition to the VR effect (high efficiency and acceptance); then a channeling peak appears and finally the crystal goes back to the amorphous state.

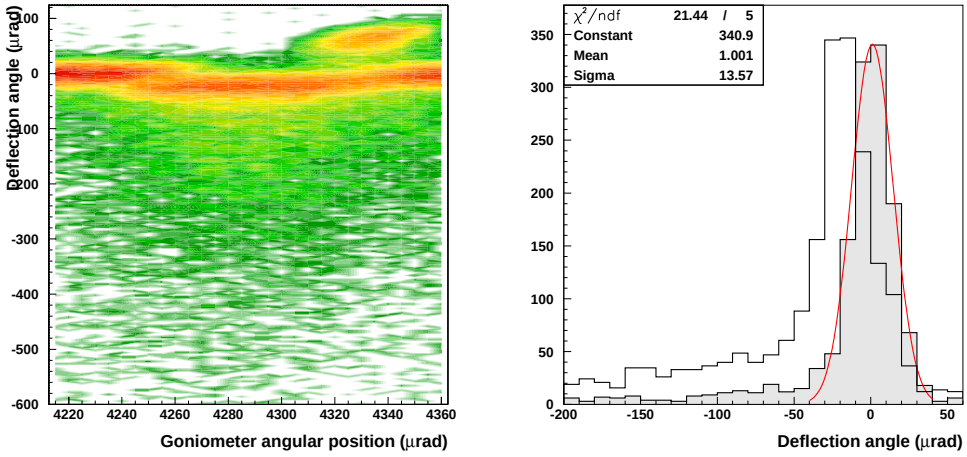

(a) (b)

Figure 4.24: a) Angular scan. b) Deflection angle distributions in the amorphous (gray) and VR (blue) positions.

For each angular position, a deflection angle (defined as the difference between the incoming and the outgoing angles) distribution is computed: figure 4.24(b) shows the angular distributions at the amorphous (gray) and volume reflection (blue) positions. A Gaussian fit of the amorphous peak provides a RMS of 13.57 μrad which is given by the squared sum of the first two detectors multiple scattering (most relevant) and the detector system resolution (negligible).

The fact that radiation has been emitted can be seen in both figures (4.24(a), 4.24(b)): the VR Gaussian left tail in figure 4.24(b), for example, is much higher than the amorphous one. The quantitative analysis is presented in section 4.2.2.

In order to show the non-homogeneous answer of the QM2 crystal, a comparison between angular scans considering different vertical regions is given in figure 4.25: considering two different vertical regions of 1.5 mm each, the mean deflection angles for the various effects are different. This difference is principally due to the non-homogeneous structure of the quasimosaic crystals and to a possible torsional effect of the crystal on its holder.

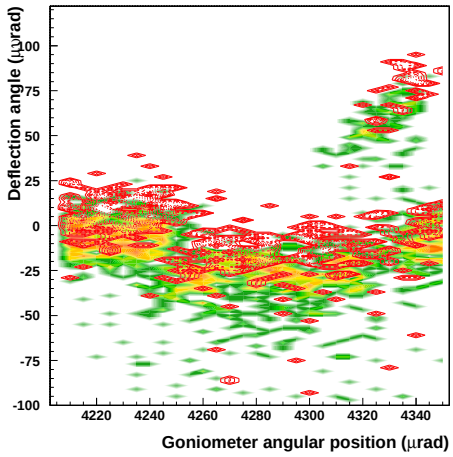

Figure 4.25: Angular scans considering different vertical regions.

4.2.2 Energy loss by light particles

The radiation emitted by light leptons has been measured exploiting what can be defined a spectrometer method, which is schematically shown in figure 4.26.

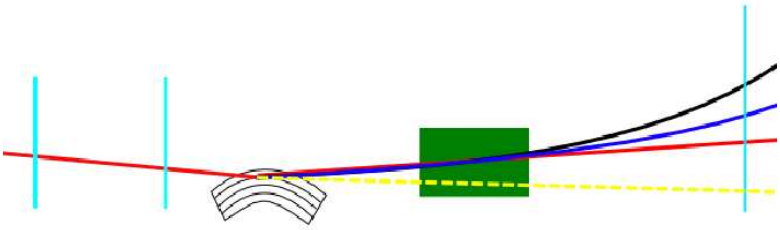

Figure 4.26: The spectrometer method: a particle in VR can emit photons (yellow dashed line), decreasing its momentum. A bending magnet steers particles depending on their momentum: the red line corresponds to a 180 GeV/c particle, while the black and blue lines correspond to particles which have lost energy. Silicon detectors (light blue) are able to reconstruct the particle trajectories.

A particle which impinges on the crystal can be in the amorphous, volume reflection or channeling states, depending on the incoming angle with respect to the crystallographic plane. In all these conditions, the particle can emit photons (yellow dashed line) and lose energy/momentum. In a bent magnet a particle is deflected depending on its momentum, following the equation:

$$p\,\theta = 0.3\,BL \tag{4.11}$$

where p is the particle momentum, θ the deflection angle, B the magnetic field and L the magnet length; in the 2007 beam test $BL = 1.041$ Tm.

Considering equation 4.11, a deflection angle distribution can be translated in an energy loss one: in figure 4.27 the main peak corresponds to the 180 GeV/c particles, while the tail is populated by particles which have lost energy.

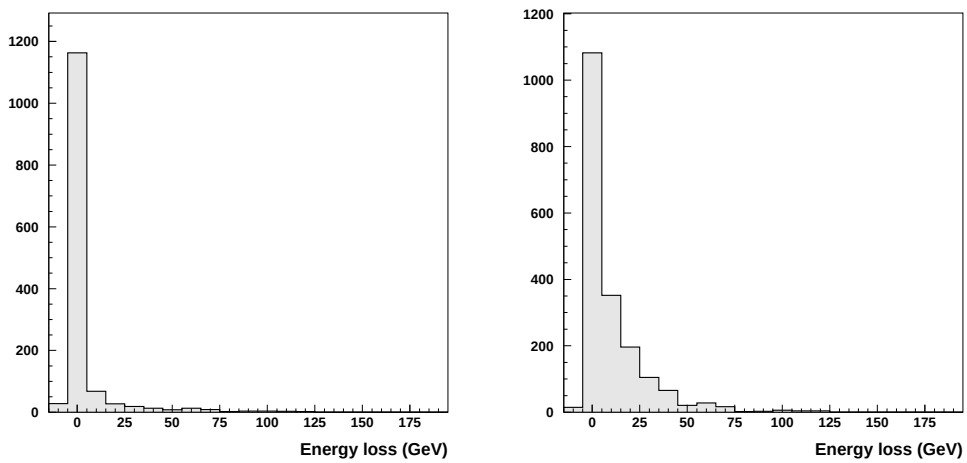

(a) (b)

Figure 4.27: The energy loss distributions for the amorphous (a) and volume reflection (b) cases.

To compare the spectrum intensity and shape in the amorphous and VR cases, the energy spectra dN/dE vs. E have to be computed: the number of the particles in a given bin is divided by the bin width energy value and normalized; for the positron case (thanks to the higher statistics) the bin width is 5 GeV, while for the electrons is 10 GeV. The normalization is given by the number of particles in the energy loss distribution (N); events with an energy smaller than 0 GeV or greater than 180 GeV are due to the system intrinsic resolution.

The errors on the experimental energy spectrum are given by the uncertainty on the particle numbers in a given bin:

$$\sigma^2_{\frac{dN}{dE}} = \frac{1}{(N\,dE)^2} dN \tag{4.12}$$

As far as the momentum uncertainty is concerned, it is evaluated according to equation 4.11:

$$\sigma^2_{Energy\ loss} = \left(\frac{0.3\,BL}{(\theta-\theta_0)^2}\right)^2 \sigma^2_\theta = \frac{(180-p)^4}{(0.3\,BL)^2}\sigma^2_\theta \tag{4.13}$$

σ_θ is the angular error mainly due to the multiple scattering contribution of the material before the bending magnet and is of the order of 15 μrad.

4.2.2.1 The amorphous contribution

The amorphous spectrum is given by the bremsstrahlung radiation in the different materials before the bending magnet; a positron which loses energy after the magnet cannot be distinguished from an unperturbed one, so the materials after the magnet must not be taken into consideration. The materials before the bending magnet were:

- two silicon detectors (2×300 μm);
- four aluminum sheets in the detector active windows (4×20 μm);
- six beam pipe flanges (Mylar) (6×180 μm);
- about 3 m of air;
- the quasimosaic crystal ($\sim$0.09 cm).

The amorphous radiation spectrum has been simulated in two ways: considering the analytical calculation [63] and a GEANT3 simulation. Figure 4.28 shows the comparison between the experimental data (blue dots) and the calculated (black line) and simulated (red line) ones for positrons.

4.2.2.2 VR radiation spectra

The volume reflection radiation experimental data have been compared with the simulation ones as shown in figure 4.29(a) for positrons ((b) for electrons).

As stated in section 2.3.3, radiation is usually described in terms of energy loss, that is as $dN/dE \cdot E$ vs. E: figure 4.30(a) shows the experimental results (blue dots for amorphous and red/green dots for VR) compared with the calculated ones (black lines) for positrons (figure 4.30(b) refers to electrons).

The comparison between the experimental and calculated energy losses spectra shows:

1. a good agreement between the experimental and calculated energy ranges of emitted γ-quanta for positrons and electrons with these ranges corresponding to the ones in the semiquantitative analysis of section 2.3.3 (figure 2.25);
2. the experimental energy losses are smaller than the computed ones of a factor ≈ 1.7 for positrons and ≈ 1.2 for electrons;

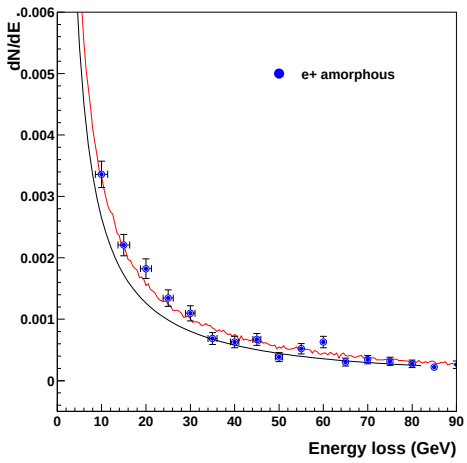

Figure 4.28: The amorphous spectrum for a positron beam: the figure shows a good agreement between experimental data (blue dots) and calculated (black line) and simulated (red line) ones.

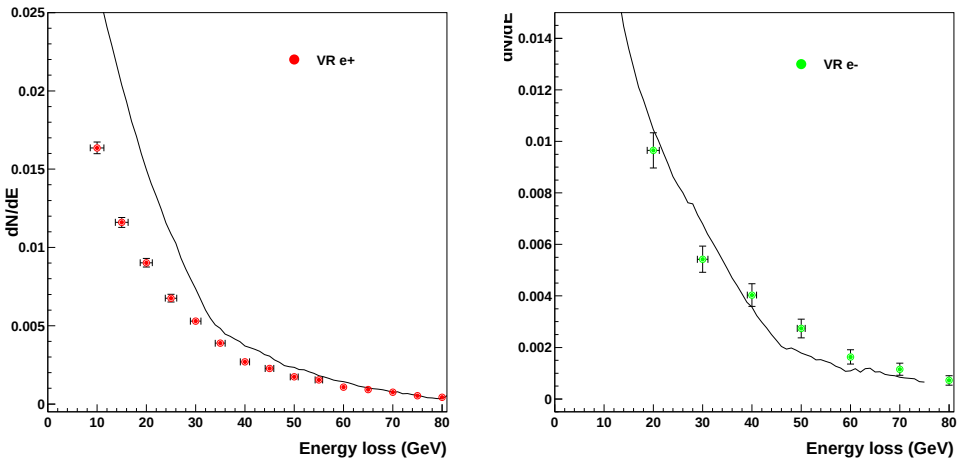

(a) (b)

Figure 4.29: The volume reflection spectrum for positrons (a) and electrons (b): experimental data (red/green dots) are compared with the calculated ones (black line).

3. an agreement good enough between experimental and computed spectra for the non-oriented case.

In particular the last item confirms the goodness of the spectrometer method;

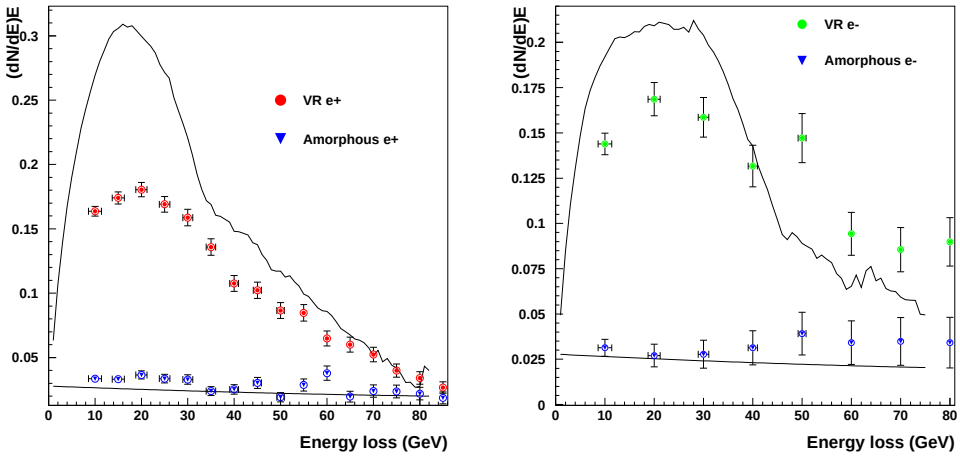

(a) (b)

Figure 4.30: The energy loss spectra ($dN/dE \cdot E$ vs. E) for the positron (a) and electron (b) cases: the blue dots are the experimental amorphous data, the red/green dots represent the volume reflection experimental results, the black lines identify the volume reflection and amorphous calculated spectra.

thus, the differences in the VR radiation spectra should be researched in the analytical calculation or in the crystal physics. After a discussion with the theoretical experts, the main reasons of the discrepancies could be explained as follows:

1. the multiple scattering of particles on the crystal atoms has not been considered in the analytical calculations;

2. the presence of a non homogeneity of the quasimosaic crystal structure and in particular the dependence of the bending radius from the particle hit position and the torsional effect due to the holder should be considered;

3. a consistent number of particles ($\sim 10-15\%$) may be captured in the channeling regime; even if they can exit channeling quickly, the motion changes;

4. the radiation of two or more γ-quanta by one particle has not been considered in the calculation.

4.3 And there is much more...

Only a small part of the results obtained in these two years have been presented in this chapter. The detection system and the beam features have allowed to collect

a huge amount of data that are still being analyzed. The understanding of the crystal related phenomena has convinced the CERN Research Board to approve a crystal collimation experiment in the SPS as described in the conclusions and have aroused the interest of the ILC groups. If a list of results were to be written down, it could be summarized as follows:

- **single silicon crystal**. Several tests have been performed with crystals with different features: the primary curvature (in particular the data collected with quasimosaic crystals have confirmed the results presented in section 4.1.1), the length and the shape (in particular with quasimosaic to check the uniformity);

- **multicrystals**. Several multicrystals have been tested: multistrip crystals formed by 7, 8 and 14 strips, 5 strips mounted on piezoelectric motors (like in the quasimosaic case, section 4.1.2) and multistrips obtained grooving a large silicon crystal;

- **axial channeling**. The study of the axial channeling has started in May 2007, thanks to the presence of a cradle on the goniometer. Axial channeling occurs when a particle is entrapped in a string of atoms, instead of two planes: the channeling in this case occurs both in the horizontal and vertical directions. In particular, in a beam test performed on the H4 line this year, a clear evidence of the "rosette" scattering (see section 2.1.5) has been observed. Moreover, the phenomenon of the multi volume reflection [74] (where a particle is volume reflected by the different secondary planes of a single crystal) allows to obtain a deflection angle of ~ 50 μrad in a single crystal;

- **germanium crystals**. Apart from diamond, a germanium crystal has been tested in 2007: volume reflection was present, while channeling has not been observed even if germanium was expected to be more efficient than silicon as far as channeling is concerned. Two reasons can explain this behavior: the crystal has been bent too much (the channeling deflection angle was ~ 1 mrad) and the raw material was not pure enough;

- **crystal undulator**. The behavior of particles which impinge on a crystal undulator has been studied in 2007 and 2008. The basic idea is to use crystal undulators with positrons and electrons to produce photons. The test with hadrons had to confirm its behavior as a bent crystal to optimize its manufacturing parameters (shape, length and primary curvature).

Chapter 5

Conclusions and outlooks

Crystals and channeling are in a way “old stuff”: from Stark’s theory in 1912 to the first experimental observations in the ’60s, from Tsyganov and its bent crystals in 1976 to the dream of using them as collimators dating something like 30 years ago.

The first part of this thesis work has tried to touch a few topics that can be considered the frontiers in the study of the channeling phenomena in bent crystals and to show how this “old stuff” is in fact extremely up-to-date: the replacement of heavy and big objects like magnets and collimators with small simple ones as silicon crystals is a captivating possibility which, anyway, requires a dedicated long and difficult R&D.

Since the middle of the ’70s, the natural application for crystals seemed to be beam collimation for high energy hadron colliders. The collimation system in a modern accelerator is typically based on a multi-stage system where a first collimator spreads the halo particles (which lower the luminosity) on the whole solid angle, while secondary and tertiary collimators absorb the produced shower. A bent crystal is able to steer particles in a given direction with a high efficiency, which means it could be used in place of the primary collimator increasing the cleaning efficiency, reducing the constraints on the alignment of the secondary collimator and finally increasing luminosity.

But collimation is just one of the possible applications of bent crystals: these devices are currently under test for their possible use in different fields, among which microbeams and radiation production. The focusing properties and the channeling phenomena in nanotubes should be able to provide very small beams for biological and medical studies; radiation could be produced in crystal undulators or in bent crystals in the channeling and volume reflection orientations.

The heart of this thesis work had a twofold purpose: describe the measurements performed by the H8RD22 collaboration in 2007 in order to develop a collimation system based on bent single and multi crystals for the second phase of

the LHC collimation and give a few details on experimental results that can be a real breakthrough in other fields.

In 2006 the volume reflection phenomenon has been experimentally confirmed at high energies and, from there on, has been studied as a valid alternative to channeling for collimation. In 2007 a new setup has been implemented to study the crystal behavior: a set of double side 5 μm resolution silicon detectors has been used to determine the trajectory of each particle which impinges on a bent crystal positioned on a high precision goniometer to align the crystal itself with the beam and perform an angular scan. The main improvement with respect to the 2006 beam test is represented by the possibility to compute the deflection angle, which is defined as the difference between the particle incoming and outgoing angles.

The 2007 beam tests have been performed with positive and negative particles: the crystals behavior has been evaluated with 400 GeV/c protons, 180 GeV/c positive and negative hadrons and muons and with 180 GeV/c electrons and positrons.

As far as the 400 GeV/c proton tests, this thesis focuses on the measurement of the dependence of the volume reflection parameters (the deflection angle, its sigma and the efficiency) from the crystal curvature: the analysis is described in detail together with the way systematic errors have been computed. The goal is not only to illustrate a result but to underline how the facility developed on H8 allows to take a huge amount of data and how the detection system is well suited in terms of spatial resolution for this kind of studies.

In order to increase the deflection angle (maintaining the acceptance and the efficiency), a series of crystals has been used to exploit the multi-reflection effect: different crystals have been aligned one with respect to the other so that the volume reflected particle on the first crystal is reflected in the second one, and so on. The measurements have been performed on several multistrip crystals (from 5 to 8 each) and on a 5 quasimosaic crystal system; in this second case the relative alignment has been obtained with remotely controlled screwdrivers and piezoelectric motors. The performance was as expected: the deflection angle increased up to 60 μrad (for the multistrip case), while the repeatability test performed on the quasimosaic crystal ensemble showed the stability of the system.

Several world premieres have been obtained in these two years: the behavior of bent crystals with negative particles (with a deep study of the volume reflection phenomena) at 180 GeV/c and the study of a diamond crystal are just an example.

At the time of writing, after the 2007 results (and in part presented in this thesis work), the CERN Super Proton Synchrotron Committee (SPSC) and the CERN Research Board have approved a crystal collimation test on the SPS accelerator ring [75].

Figure 5.1 shows a proposal of the setup for the CRYSTAL experiment, which will be installed in the SPS LSS5 straight section. It will consist of 4 stations:

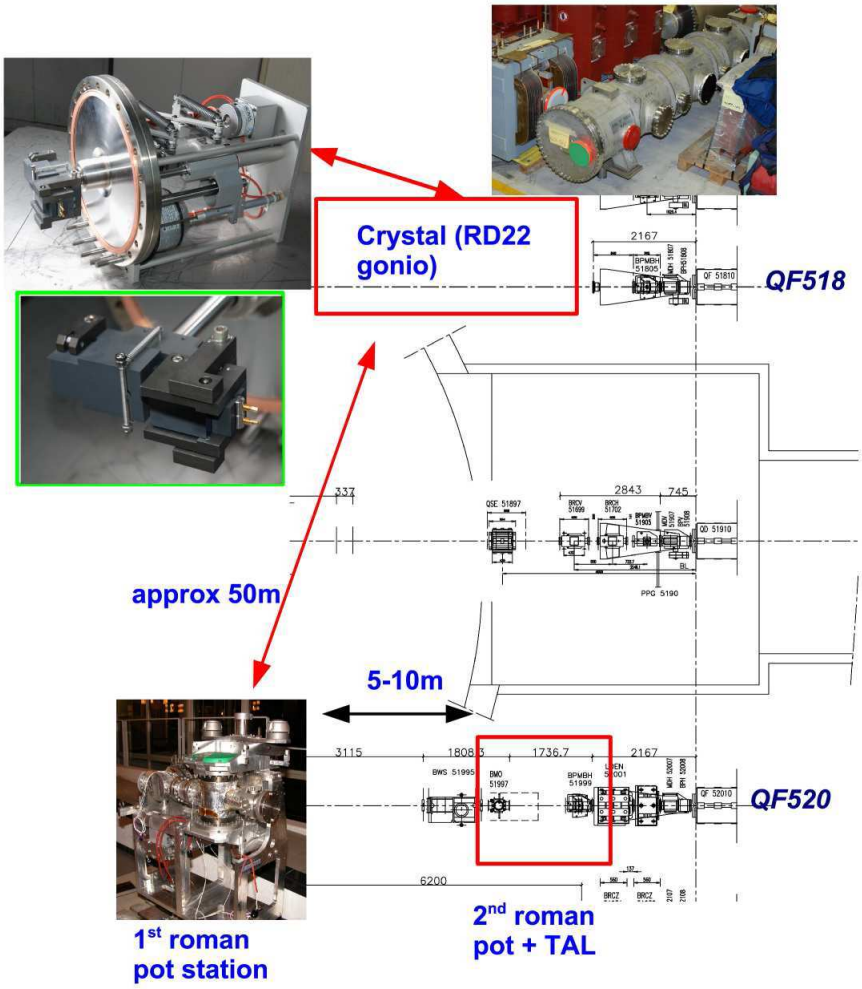

Figure 5.1: A proposal of the setup for the CRYSTAL experiment [75].

- **the crystal station**: four crystals will be placed in special vacuum tanks before the QF51810 quadrupole; the crystals will be both quasimosaic and strip in a single and multi configuration. They will be positioned on 4 goniometers which will provide the lateral (to position the crystal on the beam) and the angular movements;

- **the first roman pot** (which is a vacuum station) where the first silicon detectors will be placed. This station will monitor the beam halo in the horizontal direction to detect the volume reflection and channeling effects. The detectors will be double side microstrip silicon detectors readout by low noise self triggering ASICs;

- **the second roman pot** will consist of a similar set of detectors with the option of monitoring the vertical plane; the vertical detector will be a single side detector readout by the Mythen2 ASICs (PSI) [76]. This roman pot will be placed at 90° in phase (about 60 m) with respect to the crystal in order to maximize the distance of the steered beam particles from the beam core. The information given by the detectors in the two roman pot stations will allow to measure the phase space;

- **the TAL station** will consist of a tungsten secondary collimator to absorb the channeled or volume reflected particles.

The beam will have an energy of 120 GeV/c (but also 55 GeV/c and 270 GeV/c will be considered). The maximum flux must be compatible with a DAQ rate of 25 kHz but work is being done to increase this number to 100 kHz; as far as the counting electronics for the vertical plane is concerned, the DAQ rate is at least 3 MHz per strip. The tracking systems will be synchronized among them and with the goniometer movement.

The CRYSTAL experiment is very different from the H8 ones: in a circular accelerator, in fact, a particle can hit more than once the silicon detectors and the crystal; the contribution of the multiturn and multipass effects (see chapter 1) must be studied with a high precision. Moreover, the detectors cannot be positioned in the beam because of the large number of particles of the beam itself (up to 10^{12} particles) and because they could perturb it; thus just the beam halo has to be considered. The halo will be intercepted at around 6σ from the beam core (1σ = 0.71 mm at β_{max} (see chapter 1)); if the particle population were too low, the crystal will be moved towards the 3σ region. Locating the tracking system in a region with a phase difference of around 90° and considering a steering angle for the volume reflection of 100 μrad, a horizontal displacement of the particles of 3.6 mm is expected.

The beam halo will be created exploiting the technique used successfully for RD22 [77] in which the electrostatic deflector plates of the SPS dumper system apply random horizontal kicks to the particles. The kicks are produced by an external noise generator of limited bandwidth white noise, coupled to the power amplifiers of the plates. These uncorrelated kicks make the particles diffuse towards the crystal. A collimation test is also foreseen at the Tevatron (Fermilab) in 2010, using a particle beam of 980 GeV.

But crystals are not only collimation. The analysis performed on the radiation emitted by volume reflected light particles is a clear example in this sense. In the October 2007 beam test, the VR has been observed with 180 GeV/c electrons and positrons; high energy spectra (up to $\sim$100 GeV) have been measured exploiting a spectrometer method based on large silicon strip detectors and on

a sampling calorimeter for the electron identification. The good agreement between the experimental and analytical data for the non oriented case involves the necessity of a deep study of the analytical calculation for the volume reflection radiation spectrum and of a dedicated crystal for this kind of measurements: the theoretical explanations, in fact, are very complex and are not supported by experimental results. Moreover a complete study of the crystal behavior with light leptons foresees a complicate setup for the accurate measurement of the deflection angles depending on the crystal angular position and the evaluation of the radiation emitted by particles which impinge on the crystal (distinguishing it from the gamma background). The setup should be similar to the one shown in figure 5.2, consisting of a position sensitive high resolution calorimetric system and a high resolution spectrometer.

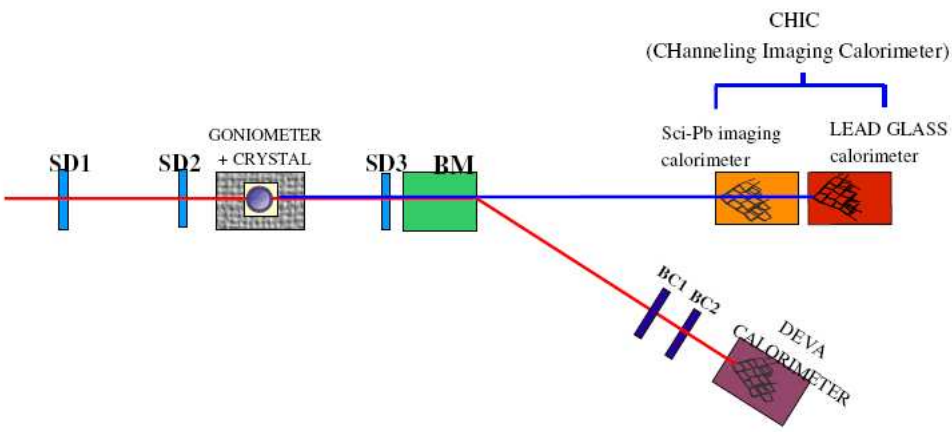

Figure 5.2: The ideal setup for the radiation spectrum measurements: the microstrip silicon telescope (SDX), the high precision goniometer (g), a bending magnet (BM), the 9.5×9.5 cm^2 silicon beam chambers (BCX), the electromagnetic calorimeter (DEVA) for the lepton line and the high energy resolution calorimeter system (CHIC) for the photon line.

The microstrip silicon detectors (SDX) are necessary to reconstruct the crystal behavior as a function of the angular position (as already done in the proton beam test). The SD3 telescope should be removed (to reduce the multiple scattering) and a bending magnet separates the charged particle beam from the gamma one. On the charged particle line, the silicon beam chambers (BCX) reconstruct the particle trajectories, while a calorimeter (DEVA) the energy (spectrometer method). Moreover, on the gamma line, a high energy resolution calorimeter system (CHIC) reconstructs the gamma spectrum: CHIC is formed by an imaging sampling calorimeter (to reconstruct the electromagnetic shower position) and a

homogeneous one (e.g. lead-glass, for high precision energy measurements). In order to select only light leptons, the trigger system can be implemented using the DEVA calorimeter.

The last word of this thesis work in then not an “end”.

Crystals have been studied for a long time. Now the technology seems mature to try the application Tsyganov dreamed of 30 years ago: hadron beam collimation.

The use of silicon detectors have allowed the crystal experts to make a jump forward in the amount and quality of the experimental data.

Radiation seems to be the next dream about crystals. Theory has to be studied, experiments will require a lot of R&D and results will not be easy to obtain. But we are just at the beginning of (hopefully) another interesting chapter of the story of crystals.

Appendix A

Data processing

The data used in chapters 3 and 4 are the result of a dedicated analysis procedure of the signals coming from the silicon detectors. To perform a data taking with this detector system, it is necessary to follow this "list of actions":

1. evaluation of the electronics baseline (*pedestal*), its *noise* and *common mode*; these information are fundamental to set a threshold for each silicon strip in the ADCs to perform the so-called *zero suppression* (section A.1);

2. for each event, particles can hit one or more silicon strips, depositing energy. The corresponding charge is collected, amplified and, if it exceeds a threshold, stored in the raw data files. A quasi online program selects the *clusters* of strips (which identify the passage of a particle) depending on their signal-to-noise ratio (SNR) for the final analysis (section A.2);

3. the quasi online program strips the raw data generating output ASCII files, containing all the necessary information on the detectors and the goniometer (section A.3).

A.1 Pedestal, noise and common mode

As explained in section 3.2.3, the energy released by a particle generates a charge which is integrated by a charge sensitive pre-amplifier, amplified, converted to current and sent to the ADC for the digitization. In case of no particles, there is anyway a signal in the ADCs due to the complete electronics chain (detector+ASICs+repeater+ADC itself): this baseline is called *pedestal*. In order to evaluate the pedestal, 200 random trigger events are generated by the sequencer in anticoincidence with the particles: the mean value for each channel is called pedestal, the RMS is called *noise*.

Figure A.1 shows an example of the pedestal analysis: the mean value for each strip (both for the junction and ohmic side) in figure A.1(a) and the RMS noise (black line) in figure A.1(b).

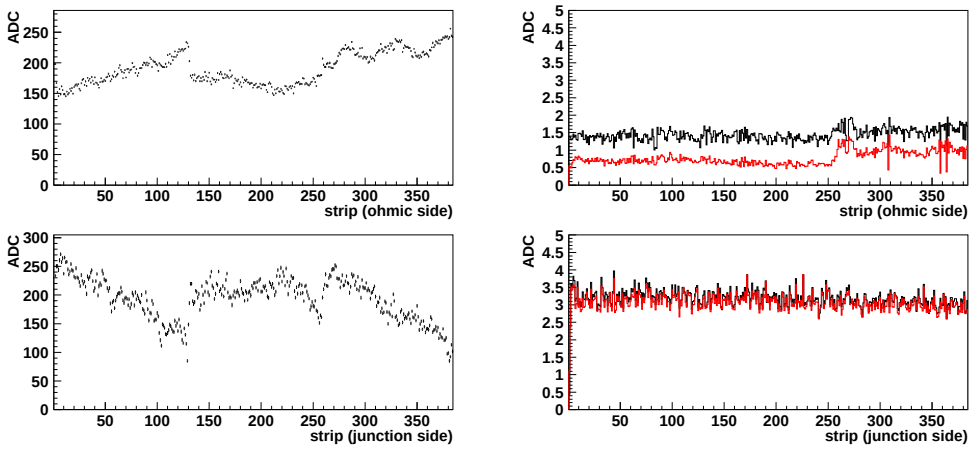

(a) (b)

Figure A.1: The pedestal analysis: a) the pedestal value for each strip of the ohmic and junction side of a telescope. b) The corresponding noise RMS (in black) and the noise RMS common mode subtracted (in red). The RMS values for the two sides cannot be compared in this plot given that the two ADCs have different gains.

The red histograms in figure A.1(b) represent the noise RMS when the so called *common mode* is subtracted. The common mode is the average shift of the pedestal around the mean value due to external noise on the detector bias lines. The evaluation of the common mode is performed for each ASIC as follows:

- the pedestal and noise values for each strip are computed;
- the pedestal value is subtracted from the raw data event by event. For each ASIC, the so obtained ADC values of the channels are summed to compute the mean value (which is the common mode); noisy and dead strips are excluded from this procedure;
- the common mode value is subtracted event by event from the raw data and the pedestal and noise values are re-computed.

Figure A.2(a) shows the common mode distribution for an ASIC: the mean value is 0, while the RMS is lower than 1 ADC. The common mode is a “detector

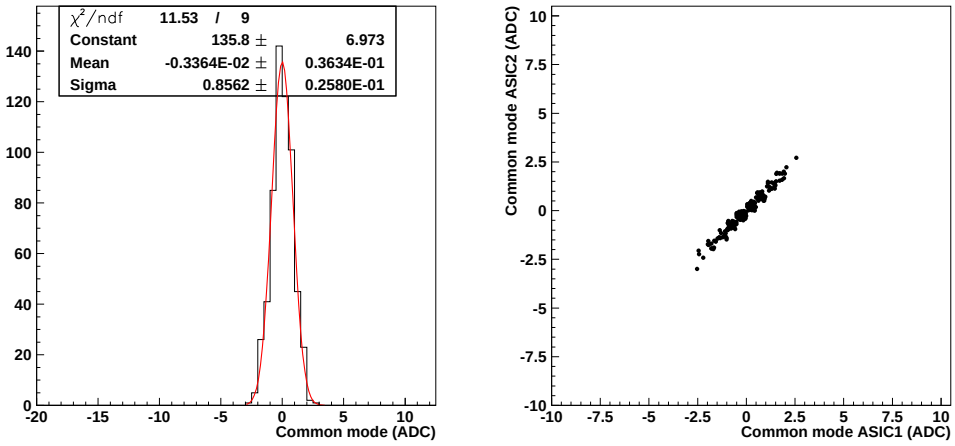

(a) (b)

Figure A.2: a) The common mode distribution for a single ASIC: its value is subtracted from the pedestal one for all the strips belonging to the ASIC itself on an event by event basis. b) The common mode correlation between two ASICs of the same silicon module.

feature": figure A.2(b) presents the common mode correlation between the first two ASICs of a detector.

Given the ADCs work is "zero suppression" (section 3.2.1), pedestals are subtracted online. The threshold for the zero suppression is set to 5 times the noise RMS value (the overall one, not the common mode subtracted one). To read silicon detectors in this mode, the common mode contribution to the total noise should be small; in presence of a high noise, the threshold should be increased, reducing the detector efficiency in the worst case or the number of strips per cluster (and thus the spatial resolution, see later on). On the other hand, high noise and standard threshold means a larger number of strips to read per module (since they are over threshold) and thus a smaller DAQ rate.

A.2 Processing data

The DAQ system produces PAW N-tuple files with the data regarding the detectors (strips over threshold) and the goniometer (the position of each motor) and further information such as the spill number, the number of steps for the scan, the trigger type, the calorimeter (if present) measured energy. The raw data are processed to produce ASCII files with the most relevant information for each event.

This pre-processing consists in the identification of the clusters (identifying

the hits position), the selection of the events with one cluster per module, the computation of the hit position in an absolute reference system (once the detectors have been aligned).

To perform the *cluster identification*, for each event and for each module, the SNR of the strip with the maximum signal is computed. The distribution is called *pull* and an example is shown in figure A.3. The strips with a SNR lower than 5 have not been readout because of the zero suppression.

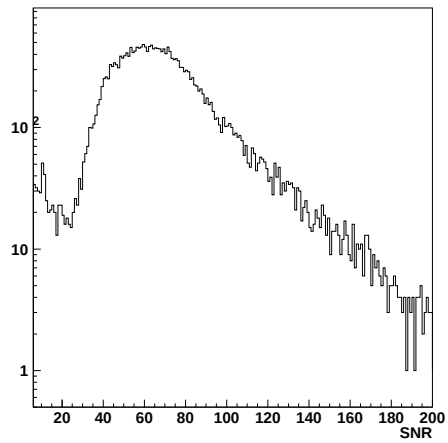

Figure A.3: The signal-to-noise ratio for one of the modules considering the strip with the highest signal on the event: in practice the distribution represents the signal in RMS units. Thanks to the zero suppression, the events with a signal lower than 5σ have not been readout; in the analysis, a signal corresponding to a SNR$>$20 has been considered a hit by a particle.

According to the pull distribution, a strip has been considered in the analysis if its signal was greater than 20σ.

A particle which impinges on a silicon detector releases energy creating electron -hole pairs that diffuse and doing so expand on several strips. This fact is enhanced in the floating strip scheme (as in the junction side of the telescopes or in the beam chambers), where the readout pitch is double with respect to the physical one. A *cluster* is a group of contiguous strips collecting the charge generated by one particle: the cluster central strip (according to the pull) must have a signal 20 times larger than its RMS; the lateral strips must have a SNR greater than 6. Figure A.4(a) shows the number of clusters in a module: 98% of the events have a single cluster. To produce the ASCII files (section A.3), a single cluster for every horizontal module at the same time is requested: the total “ASCII” events are in general more than 80% of the raw ones.

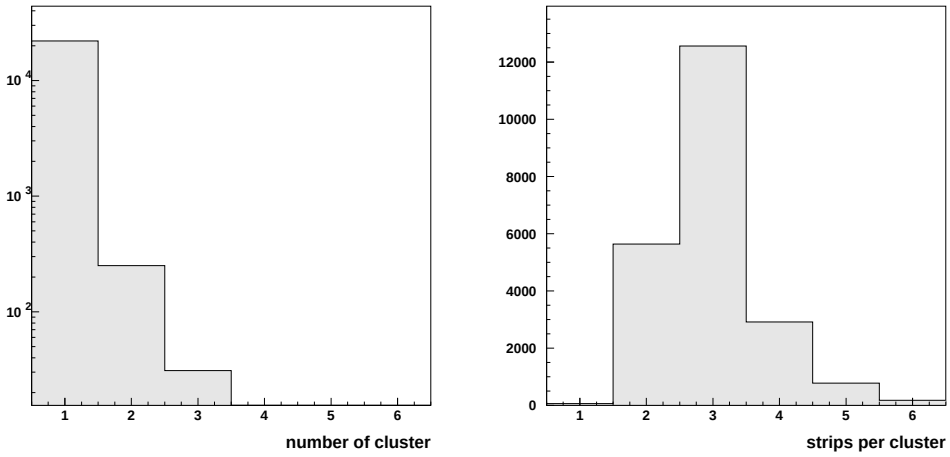

(a) (b)

Figure A.4: a) The number of clusters in a module in logarithmic scale: in 98% of the total cases there is only a single cluster per module. b) The number of strips per cluster: the most probable values are 2 and 3.

The number of strips per cluster is shown in figure A.4(b): in general there are 2 or 3 strips per cluster.

Being this system an analog one, it is possible to evaluate the energy deposited by a particle: the pulse height distribution is given by the sum of the signals of the strips which belong to a cluster and can be fitted with a simplified Landau function[1], as shown in figure A.5.

A.3 ASCII file

In the raw data stripping, an event is considered "good" if it has a single cluster for each horizontal module (single particle event). The stripped events are more than 80% of the total ones.

The ASCII file contains the following information (an ASCII row corresponds to one original event):

- the particle hit position for each silicon module;
- the number of strips per cluster;

[1] $F(x) = A * exp(-0.5 * (\lambda + exp(-\lambda)))$, where $\lambda = \frac{(x-C)}{(B/4.02)}$, C is the most probable value and B the FWHM.

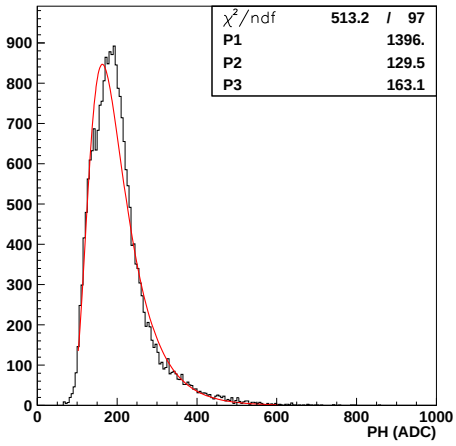

Figure A.5: The pulse height distribution.

- the energy released by the particle in the calorimeter tiles;
- the value of the goniometer motors;
- further information about the number of spill, number of step (for lateral, angular and cradle scans) and the absolute event number.

A.4 The detector alignment

An important task for the analysis is the detector alignment: in fact, the detectors have not been installed on the beam line with an absolute reference frame. Figure A.6 shows a typical situation: the red line which crosses the detectors is the mean trajectory of the unperturbed beam (without crystal or with a crystal in the amorphous orientation).

The crystal behavior is evaluated by the deflection angle (δ), that is defined as $\delta = \beta - \alpha$. The incoming (α) angle is defined as the ratio between the difference of the first and the second detector hit positions and the distance between the modules, the outgoing one (β) is the same, but considering the second and one of the farthest detectors.

If the detectors were perfectly aligned, the angular distributions would be centered on 0, which is not the case shown in figure. The first step of the analysis is the relative alignment of the detectors consisting in two phases:

1. alignment of the first and last detector;

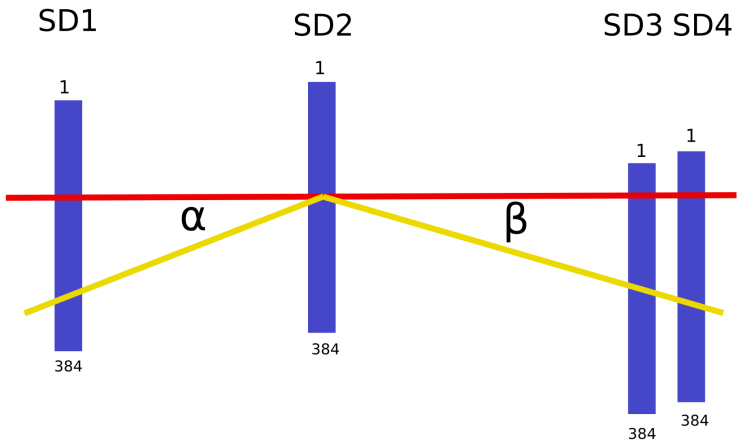

Figure A.6: The detector alignment.

2. alignment of the central detectors via the residuals method.

In the first step, the distribution of the difference between the first and the last detector hit positions (both in the horizontal and vertical direction) is considered: these two detectors (SD1-SD4) are “aligned” when the distribution mean value is very close to zero.

SD1 and SD4 are then used to reconstruct the track and compare the point it crosses SD2 and SD3 (real position) with the reconstructed one. This difference is called *residual*; as already said in section 3.2.1, the distribution RMS value can be used to evaluate the detector resolution. Shifting SD2 and SD3 in order to get a residual centered on 0 is the second phase of the alignment.

Using this method, the angular distributions (incoming, outgoing and deflection angles) are therefore centered on zero.

List of acronyms

ADC	Analog to Digital Converter
AGILE	Astro rivelatore Gamma a Immagini LEggero
ASCII	American Standard Code for Information Interchange
ASI	Agenzia Spaziale Italiana
ASIC	Application-Specific Integrated Circuit
bcc	body centered cubic
BNL	Brookhaven National Laboratories
BTF	Beam Test Facility
CERN	European Organization for Nuclear Research (Conseil Europeen pour la Recherche Nucleaire)
CFC	Carbon-Fibre-reinforced Carbon
DAQ	Data AcQuisition
DMA	Direct Memory Access
fcc	face centered cubic
FLUKA	A fully integrated particle physics Monte Carlo simulation package
FWHM	Full Width Half Maximum
IHEP	Institute of High Energy Physics
ILC	International Linear Collider
INFN	Istituto Nazionale di Fisica Nucleare
IP	Interaction Point
LET	Linear Energy Transfer
LHC	Large Hadron Collider
LINAC	LINear ACcelerator
LNF	Laboratori Nazionali di Frascati
MIP	Minimum Ionizing Particle
NASA	National Aeronautics and Space Administration
NIM	Nuclear Instrumentation Module
NSRL	NASA Space Radiation Laboratory
PAW	Physics Analysis Workstation
PCB	Printed Circuit Board

PIXE	Particle Induced X-ray Emission
PMT	Photo-Multiplier Tube
PNPI	Petersburg Nuclear Physics Institute
PS	Proton Synchrotron
R&D	Research & Development
RBE	Relative Biological Effectiveness
RBS	Rutherford BackScattering
RF	RadioFrequency
RMS	Root Mean Square
SNR	Signal-to-Noise Ratio
SPS	Super Proton Synchrotron
Tcl/Tk	Tool Command Language/Toolkit
VME	Versa Module Eurocard
VC	Volume Capture
VR	Volume Reflection
WLS	Wave Length Shifter

List of Figures

1.1 Transverse energy density as a function of beam momentum for several accelerators and the super-conducting magnets at the ALICE interaction point. 8
1.2 The geometric and dynamic apertures. 9
1.3 The beam intensity as a function of the local cleaning inefficiency for energies of 450 GeV and 7 TeV. 10
1.4 FLUKA simulations of the maximum energy deposit as a function of the mass length (and thus Z) for different materials. 12
1.5 Layout of the LHC collimation during phase I. 12
1.6 Principle of collimation and beam cleaning during collisions in phase I and normalized population of secondary and tertiary beam halo for protons impinging on the first collimators. 13
1.7 Consumable collimators based on bars, wheels and tapes. 14
1.8 Traditional multi-stage collimation system and with bent crystals. 15
1.9 Simulated channeling efficiency as a function of the crystal length for the injection and operational energies. 16
1.10 Single and multi-reflection collimation systems. 17
1.11 Simulated channeling efficiency as a function of the crystal surface roughness and X-ray images of a crystal surface. 18
1.12 Typical cell survival curves and two methods used for microbeams. 20
1.13 The Bragg peak: dose deposit of photons, protons and carbon ions in water and general layout of the PIMMS design study. 22
1.14 PIXE spectrum of a stormwater particulate. 24
1.15 An example of a microbeam facility for art studies. 24
1.16 Number of counts for several elements in two pages of the analyzed manuscript. 25
1.17 The principle of beam focusing with a bent crystal and an experimental example. 26
1.18 Simulation of several nanotube structures. 27
1.19 The continuous potential within a carbon nanotube of 1.1 nm of diameter and the same nanotube bent of $pv/R = 1$ GeV/cm 27

1.20 Number of channeled particles as a function of the nanotube curvature. 28
1.21 Synchrotron radiation emission and spectrum. 29
1.22 The undulator magnet. 30
1.23 Undulator radiation cone and radiation energy spectrum. 31
1.24 The wiggler continuous spectrum emitted in a cone. 33
1.25 Synchrotron radiation from bending magnets, multiple wigglers and undulators. 33
1.26 Crystallographic plane distorsion near a surface scratch, crystal undulator scheme and an example of a microgroove on the crystal surface. 34
1.27 X-ray test of a crystal undulator and a crystal undulator test on a circulating high-energy proton beam. 35
1.28 Deflection beam profile and efficiency for two values of the crystal orientation angle. 36
1.29 Schematics of the setup to measure the photon emission in a crystalline undulator. 37
1.30 The expected photon spectrum for 800 MeV and for 3 GeV positrons. 37

2.1 The main planes of the simple cubic lattice. 41
2.2 The diamond crystal structure is a face centered cubic. 41
2.3 Motion of a particle misaligned with respect to the crystal and the average potential due to the plane. 42
2.4 The (100) silicon potential in the Molière approximation at different temperatures. 43
2.5 The interplanar potential for the (110) and (111) silicon channels. 44
2.6 The particle motion in the channel is guaranteed by the small transverse momentum. 46
2.7 The trajectories of 450 GeV/c simulated protons in a (111) silicon plane for a straight crystal. 46
2.8 Computed L_D trend as a function of pv for (110) and (111) Si crystals and experimental results on the measurement of the dechanneling length in silicon. 50
2.9 The axial channeling. 50
2.10 The transverse electric fields in the Molière approximation. 51
2.11 The bent crystal scheme and the mechanical holder. 52
2.12 The channeling motion of a particle in a bent crystal 54
2.13 The effective interplanar potential for a (110) Si crystal in the Molière approximation for a straight channel. 54
2.14 Possible particle trajectories in a straight and bent crystal. 57
2.15 Volume capture effect. 58

2.16 Volume reflection phenomenon. 60
2.17 The effective potential at the turning point. 62
2.18 Electron density and the mean energy loss as a function of the transverse coordinate and calculated and measured δ-rays yield as a function of the incident particles angle. 64
2.19 Energy loss spectra of 15 GeV/c protons in a 0.74 mm germanium crystal. 65
2.20 Radiation emitted by 10 GeV/c positron and electron beams which impinge on a (110) 0.1 thick silicon crystal. 67
2.21 Schematic view of a channeled particle motion in a bent crystal. . 68
2.22 The intensity of radiation emitted by relativistic positrons ($\gamma = 10^4$) in bent crystals as a function of the crystal curvature. 69
2.23 Radiation spectra in the forward direction of a relativistic positron in a bent channel. 70
2.24 The radiation spectrum for positrons channeled along the (110) planes in a bent silicon crystal. 71
2.25 The relative transverse velocities (v_t/c) of 180 GeV/c positrons and electrons at volume reflection. 73
2.26 The maximum energies of the γ-quanta. 74
2.27 Differential radiation energy spectrum for positrons and electrons in a 0.45 cm silicon crystal with respect to the amorphous contribution. 75

3.1 The CERN accelerator complex. 78
3.2 The North Area complex. The H8 line is the first from the bottom. 78
3.3 The May and November setup. 79
3.4 The October setup. 80
3.5 The telescope detectors. 82
3.6 The VA2 ASIC architecture. 83
3.7 The residual distribution of one of the telescopes. 83
3.8 The AGILE beam chambers. 84
3.9 The residual distribution of an AGILE beam chamber: the average RMS value is 20.9 μm. 85
3.10 The DEVA calorimeter. 86
3.11 The DEVA spectra. 86
3.12 The DAQ chain. 87
3.13 The DAQ user interface. 88
3.14 The repeater board on a telescope module. 89
3.15 The quasimosaic crystal. 90
3.16 The strip crystal. 91
3.17 The multireflection principle in a collimation system. 92

3.18 The multireflection system. 93
3.19 The remotely controlled alignment systems. 93
3.20 The goniometer system. 94
3.21 The horizontal and the vertical beam sizes for the proton beam. . . 95
3.22 The horizontal and the vertical beam sizes for the positron beam. . 96
3.23 The horizontal and the vertical incoming divergences for the proton beam. 96
3.24 The horizontal and the vertical incoming divergences for the positron beam. 97
3.25 The deflection angle distribution for the amorphous and volume reflection cases. 97
3.26 The pre-alignment laser system. 98
3.27 The lateral scan. 99
3.28 The angular scan. 100

4.1 Angular scan of the ST9 crystal with a primary curvature of about 36 m. 103
4.2 Horizontal and vertical geometrical cuts applied in the analysis to reduce the background events. 105
4.3 The channeling orientation moving the crystal or selecting divergence slices. 105
4.4 The channeling efficiency evaluated considering divergence slices of 2 μrad. 106
4.5 The channeling efficiency as a function of the amplitude of the divergence region in the horizontal direction. 107
4.6 The channeling efficiency as a function of the amplitude of the divergence region in the vertical direction. 108
4.7 Gaussian fit of the deflection angle in the amorphous position for the 36 m case. 108
4.8 Channeling position for the 36 m case. 109
4.9 The volume reflection position for the 36 m case. 110
4.10 The VR peak position and its corresponding RMS. 112
4.11 The VR inefficiency. 113
4.12 The MQM5 alignment. 114
4.13 The MQM5 fine angular scan. 114
4.14 The MQM5 performances. 115
4.15 The MQM5 VR efficiency. 116
4.16 The M8 multistrip crystal performances. 117
4.17 The diamond crystal. 118
4.18 The negative beam energy loss spectrum. 119
4.19 The negative beam shape and divergence. 120

4.20 The angular scan of QM2 with negative particles. 120
4.21 The channeling and volume reflection orientations with negative particles in the QM2 crystal. 121
4.22 The horizontal and vertical beam profiles at the crystal position. . 123
4.23 The horizontal and vertical incoming angle distributions. 123
4.24 Angular scan and deflection angle distributions in the amorphous and VR positions for a positron beam which impinges on the QM2 crystal. 124
4.25 Angular scans considering different vertical regions. 125
4.26 The spectrometer method. 125
4.27 The energy loss distributions for the amorphous and volume reflection cases. 126
4.28 The amorphous spectrum for a positron beam. 128
4.29 The volume reflection spectrum for positrons and electrons. 128
4.30 The energy loss spectra ($dN/dE \cdot E$ vs. E) for the positron and electron cases. 129

5.1 A proposal of the setup for the CRYSTAL experiment. 133
5.2 The ideal setup for the radiation spectrum measurements. 135

A.1 The pedestal analysis. 138
A.2 The common mode analysis. 139
A.3 The pull distribution. 140
A.4 Number of cluster per module and number of strips per cluster. . . 141
A.5 The pulse height distribution. 142
A.6 The detector alignment. 143

List of Tables

2.1 Main parameters of the silicon, germanium and tungsten planar channels. 44
2.2 The potential well depth of some axial channels for silicon, germanium and tungsten crystals at room temperature. 52

3.1 The goniometer system features. 94

4.1 The channeling peak position, its sigma and the primary bending value with the corresponding error. 109
4.2 The VR parameters: the peak position, its sigma and the inefficiency for each value of the primary bending radius with their statistical and systematic errors. 111
4.3 The repeatability test results on the MQM5 crystal remotely controlled by piezoelectric motors. 116

Bibliography

[1] O. S. Bruning et al. . *LHC Design Report*. CERN, Geneva, 2004.

[2] J. Resta López. *Design and Performance Evaluation of Nonlinear Collimation Systems for CLIC and LHC*. PhD thesis, Valencia Univ., Valencia, 2007.

[3] G. Robert-Désmolaize. Design and performance optimization of the LHC collimation system. Technical report, CERN, 2006.

[4] R. W. Assmann et al. . Requirements for the LHC collimation system. *LHC-Project-Report-599*, page 4, 2002.

[5] R. W. Assmann et al. . Designing and building a collimation system for the high-intensity LHC beam. *LHC-Project-Report-640*, page 4, 2003.

[6] N. Catalan-Lasheras. *Transverse and Longitudinal Beam Collimation in a High-Energy Proton Collider (LHC)*. PhD thesis, Zaragoza Univ., Geneva, 1998.

[7] J. B. Jeanneret. Optics of a two-stage collimation system. *Phys. Rev. Spec. Top. Accel. Beam - LHC-Project-Report-243*, page 13, 1998.

[8] P. Sievers et al. . Appropriate materials for LHC collimators. *Workshop on LHC performance, Chamonix, France*, 2003.

[9] H. Burkhardt et al. . Measurements of the LHC collimator impedance with beam in the SPS. *LHC-Project-Report-831*, page 4, 2005.

[10] R. W. Assmann et al. . The final collimation system for the LHC. *LHC-PROJECT-Report-919*, page 4, 2006.

[11] A. Bertarelli et al. . Mechanical design for robustness of the LHC collimators. *21st IEEE Particle Accelerator Conference, Knoxville, TN, USA*, 2005.

[12] R. W. Assmann et al. . LHC collimation design and results from prototyping and beam tests. *LHC-Project-Report-850*, page 4, 2005.

[13] J. Frisch et al. . Advanced collimator prototype results for the NLC. *Beam Instrumentation Workshop 2000: Ninth Workshop*, 546(1):374–382, 2000.

[14] F. Zimmermann et al. . New final focus concepts at 5 TeV and beyond. *8th Workshop on Advanced Accelerator Concepts*, 1998.

[15] V. M. Biryukov. Crystal simulations: the road from the SPS to the LHC. Technical Report physics/0507130, 2005.

[16] R. W. Assmann. Collimators and cleaning, could this limit the LHC performance? *Workshop on LHC performance, Chamonix, France*, 2003.

[17] A. Vomiero et al. . Structure and morphology of surface of silicon crystals to be applied for channeling at relativistic energies. *Nucl. Instrum. Meth. B*, 249:903–906, 2006.

[18] A. G. Afonin et al. . High-efficiency beam extraction and collimation using channeling in very short bent crystals. *Phys. Rev. Lett.*, 87:94802, 2001.

[19] A. Baurichter et al. . Channeling of high-energy particles in bent crystals: experiments at the CERN SPS. *Nucl. Instrum. Meth. B*, 164:27–43, 2000.

[20] S. I. Baker et al. . Effects on channeling of radiation damage due to 28 GeV protons. *Nucl. Instrum. Meth. B*, 90:119–123, 1994.

[21] M. Folkard et al. . The use of radiation microbeams to investigate the bystander effect in cells and tissues. *Nucl. Instrum. Meth. A*, 280(1):446–450, 2007.

[22] J. M. Lagniel et al. . Status of the hadrontherapy projects in Europe. *Particle Accelerator Conference 2007*, 2007.

[23] U. Amaldi. The Italian hadrontherapy project CNAO. *Phys. Medica*, XVII(I), 2001.

[24] L. Badano et al. . Proton-Ion Medical Machine Study (PIMMS), 1. *CERN-PS-99-010-DI*, page 232, 1999.

[25] P. J. Bryant et al. . Proton-Ion Medical Machine Study (PIMMS), 2. *CERN-PS-2000-007-DR*, page 340, 2000.

[26] F. Meot et al. . Etoile hadrontherapy project, review of design studies. *European Particle Accelerator Conference 2002*, 2002.

[27] M. Durante et al. . Preparatory study of investigations into biological effects of radiation. *European Space Agency - ESA-ESTEC*, 2006.

[28] J. Kennedy et al. . Elemental analysis of urban stormwater particulate matter by PIXE. *Nucl. Instrum. Meth. B*, 258(2):435–439, 2007.

[29] J. Kennedy et al. . Microprobe analysis of brine shrimp grown on meteorite extracts. *Nucl. Instrum. Meth. B*, 260(1):184–189, 2007.

[30] M. Hajivaliei et al. . Application of PIXE to study ancient Iranian silver coins. *Nucl. Instrum. Meth. B*, 266:1578–1582, 2008.

[31] A. Migliori et al. . Scanning-PIXE analysis of gold lace embroideries in a relic of St. Francis. *Nucl. Instrum. Meth. B*, 266:2339–2342, 2008.

[32] M. Massi et al. . The external beam microprobe facility in Florence: set-up and performance. *Nucl. Instrum. Meth. B*, 190(1-4):276–282, 2002.

[33] R. Cambria et al. . A methodological test of external beam PIXE analysis on inks of ancient manuscripts. *Nucl. Instrum. Meth. B*, 75:488–492, 1993.

[34] V. M. Biryukov et al. . Channeling technique to make nanoscale ion beams. *Nucl. Instrum. Meth. B*, 231(1-4):70–75, 2005.

[35] A. I. Smirnov et al. . First results from a study of a 70 GeV proton beam being focused by a bent crystal. *Nucl. Instrum. Meth. B*, 69(2-3):382–384, 1992.

[36] G. N. Greaves and C. R. A. Catlow. *Applications of synchrotron radiation*. Chapman and Hall, 1990.

[37] D. T. Attwood. *http://www.coe.berkeley.edu/AST/sxreuv/*.

[38] W. Gudat and J. Pflüger. Undulator-wiggler magnets for low energy storage rings. *Zeitschrift für Physik B Condensed Matter*, 61(4):483–491, 1985.

[39] J. A. Clarke. *The Science and Technology of Undulators and Wigglers*. Oxford University Press, 2004.

[40] S. Bellucci et al. . Experimental study for the feasibility of a crystalline undulator. *Phys. Rev. Lett.*, 90:034801, 2003.

[41] V. M. Biryukov , Y. A. Chesnokov, and V. I. Kotov. *Crystal Channeling and Its Application at High-Energy Accelerators*. Springer, 1997.

[42] A. G. Afonin et al. . Crystal undulator experiment at IHEP. *Nucl. Instrum. Meth. B*, 234(1-2):122–127, 2005.

[43] S. Bellucci et al. . Crystal undulator as a novel compact source of radiation. *Particle Accelerator Conference 2003*, 2003.

[44] S. Bellucci et al. . Crystal undulator as a new compact source of radiation. *Phys. Rev. ST Accel. Beams*, 7(2):023501, 2004.

[45] J. Stark. *Phys. Zs.*, 13:973, 1912.

[46] E. Tsyganov. Some aspects of the mechanism of a charge particle penetration through a monocrystal. *Fermilab preprint TM-682*, 1976.

[47] E. Tsyganov. Estimates of cooling and bending processes for charged particle penetration through a monocrystal. *Fermilab preprint TM-684*, 1976.

[48] J. Lindhard. Motion of swift charged particles, as influenced by strings of atoms in crystals. *Phys. Lett.*, 12:126–128, 1964.

[49] H. Kumm et al. . Rosette motion and string scattering of 20 MeV electrons in MgO single crystals. *Radiation Effects and Defects in Solids*, 12:53, 1972.

[50] Y. H. Ohtsuki, Y. Yamamura, and M. Yoshimatsu. Axial-channeling radiation of MeV electrons in high-Z materials. *Phys. Rev. B*, 28(7):3718–3724, Oct 1983.

[51] A. F. Elishev et al. . Steering of charged particle trajectories by a bent crystal. *Phys. Lett. B*, 88:387–391, 1979.

[52] A. M. Taratin and S. A. Vorobiev. Deflection of high-energy charged particles in quasi-channeling states in bent crystals. *Nucl. Instrum. Meth. B*, 26:512–521, 1987.

[53] Yu. M. Ivanov et al. . Volume reflection of a proton beam in a bent crystal. *Phys. Rev. Lett.*, 97(14):144801, 2006.

[54] A. M. Taratin and W. Scandale. Volume reflection of high-energy protons in short bent crystals. *Nucl. Instrum. Meth. B*, 262(2):340–347, 2007.

[55] V. A. Maisheev. On volume reflection of ultrarelativistic particles in single crystals. *physics/0607009*, 2006.

[56] L. Landau. Energy loss of fast particles by ionization. *Journal of Physics*, 8:201–205, 1944.

[57] J. F. Bak et al. . Measurement of average electron densities in Si and Ge using MeV δ-rays produced by channelled high-energy projectiles. *Nucl. Phys. A*, 389:533–556, 1982.

[58] S. Bellucci and V. A. Maisheev. Coherent bremsstrahlung in imperfect periodic atomic structures. *Phys. Rev. B*, 71(17):174105, 2005.

[59] J. Bak et al. . Channeling radiation from 2-55 GeV/c electrons and positrons: planar case. *Nucl. Phys. B*, 254:491–527, 1985.

[60] A. M. Taratin and S. A. Vorobiev. Radiation of high-energy positrons channeled in bent crystals. *Nucl. Instrum. Meth. B*, 31:551–557, 1988.

[61] A. W. Saenz and H. Überall. *Coherent Radiation Sources*. Springer, 1985.

[62] L. D. Landau and E. M. Lifshitz. *The classical theory of fields*. Pergamon, Oxford, 1971.

[63] Yu. A. Chesnokov et al. . Radiation of photons in process of charged particle volume reflection in bent monocrystal. *JINST*, 3:P02005, 2008.

[64] V. N. Baier et al. . Electromagnetic processes at high energies in oriented single crystals. Singapore World Scientific, 1998. Singapore.

[65] V. A. Maisheev. Volume reflection of ultrarelativistic particles in single crystals. *Phys. Rev. ST Accel. Beams*, 10(8):084701, 2007.

[66] S. Hasan. Bent silicon crystals for the LHC collimation studies with an ultrarelativistic proton beam. *Master degree thesis*, Università degli Studi dell'Insubria, 2007.

[67] UA1 Collaboration. Further evidence for charged intermediate vector bosons at the SPS collider. *Phys. Lett. B*, 129(3-4):273–282, 1983.

[68] L. Celano et al. . A high resolution beam telescope built with double sided silicon strip detectors. *Nucl. Instrum. Meth. A*, 381:49–56, 1996.

[69] G. Barbiellini et al. . The AGILE silicon tracker: testbeam results of the prototype silicon detector. *Nucl. Instrum. Meth. A*, 490:146–158, 2002.

[70] M. Prest et al. . The AGILE silicon tracker: an innovative γ-ray instrument for space. *Nucl. Instrum. Meth. A*, 501:280–287, 2003.

[71] W. Scandale et al. . Apparatus to study crystal channeling and volume reflection phenomena at the SPS H8 beamline. *Rev. Sci. Instr.*, 79(2):023303, 2008.

[72] H. Okuno et al. . Experimental study of positron production from a W single crystal by the KEK 8 GeV electron linac beam. *Nucl. Instrum. Meth. B*, 201(1):259–265, 2003.

[73] A. Seryi et al. . Design of the Beam Delivery System for the International Linear Collider. *Particle Accelerator Conference 07*, 2007.

[74] V. Tikhomirov. Multiple volume reflection from different planes inside one bent crystal. *Phys. Lett. B*, 655:217–222, 2007.

[75] W. Scandale and M. Prest. Proposal of the CRYSTAL experiment. Technical Report CERN-SPSC-2008-014. SPSC-P-335, 2008.

[76] B. Schmitt et al. . Development of single photon counting detectors at the Swiss Light Source. *Nucl. Instrum. Meth. A*, 518(1):436–439, 2004.

[77] F. Ferroni et al. . Proton extraction from the SPS with a bent crystal. *Nucl. Instrum. Meth. A*, 351(1):183–187, 1994.

Acknowledgments

There are a lot of people that I would like to acknowledge for their contribution to this thesis work. First of all the organizations which have supported the described research: CERN, INFN (section of Milano Bicocca and Trieste) and the University of Insubria. Many thanks to the H8RD22 collaboration and in particular to its spokesman, Walter Scandale, for the support and the fruitful discussions in these two years.

Many thanks to the splendid group of students at the Physical Department at the University of Insubria: Alessandro, Aldo, Andrea, Daniela, Selene, Valerio; thanks really a lot for the help and friendship. In particular, many thanks to Said for the time spent during the beam tests and all the secrets about bent crystals that I could learn from him.

Many thanks to Erik, for his helpfulness and support during the whole period of this work (and not only!) and for the huge amount of valuable learning received from him in several fields.

Finally, I would like to thank the person who has allowed all of this: Michela. Thanks for the opportunities in these three years, for the time spent on the analysis or making plannings, for all the things which I have learned and, especially, for trusting in me. Thanks!

At the end, thanks to my family, for always being there.